Astronomy & Astrophysics

The chemistry and spatial distribution of small hydrocarbons in UV-irradiated molecular clouds: the Orion Bar PDR[*],[**]

S. Cuadrado[1,2], J. R. Goicoechea[1,2], P. Pilleri[3,4], J. Cernicharo[1,2], A. Fuente[5], and C. Joblin[3,4]

[1] Grupo de Astrofísica Molecular, Instituto de Ciencia de Materiales de Madrid (ICMM, CSIC), Sor Juana Ines de la Cruz 3, 28049 Cantoblanco, Madrid, Spain
e-mail: s.cuadrado@icmm.csic.es
[2] Centro de Astrobiología (CSIC-INTA), Carretera de Ajalvir km 4, 28850 Torrejón de Ardoz, Madrid, Spain
[3] Université de Toulouse, UPS-OMP, IRAP, Toulouse, France
[4] CNRS, IRAP, 9 Av. colonel Roche, BP 44346, 31028 Toulouse Cedex 4, France
[5] Observatorio Astronómico Nacional, Apdo. 112, 28803 Alcalá de Henares, Madrid, Spain

ABSTRACT

Context. Carbon chemistry plays a pivotal role in the interstellar medium (ISM) but even the synthesis of the simplest hydrocarbons and how they relate to polycyclic aromatic hydrocarbons (PAHs) and grains is not well understood.
Aims. We study the spatial distribution and chemistry of small hydrocarbons in the Orion Bar photodissociation region (PDR), a prototypical environment in which to investigate molecular gas irradiated by strong UV fields.
Methods. We used the IRAM 30 m telescope to carry out a millimetre line survey towards the Orion Bar edge, complemented with $\sim 2' \times 2'$ maps of the C_2H and c-C_3H_2 emission. We analyse the excitation of the detected hydrocarbons and constrain the physical conditions of the emitting regions with non-LTE radiative transfer models. We compare the inferred column densities with updated gas-phase photochemical models including ^{13}CCH and $C^{13}CH$ isotopomer fractionation.
Results. Approximately 40% of the lines in the survey arise from hydrocarbons (C_2H, C_4H, c-C_3H_2, c-C_3H, $C^{13}CH$, ^{13}CCH, l-C_3H, and l-H_2C_3 in decreasing order of abundance). We detect new lines from l-C_3H^+ and improve its rotational spectroscopic constants. Anions or deuterated hydrocarbons are not detected, but we provide accurate upper limit abundances: $[C_2D]/[C_2H] < 0.2\%$, $[C_2H^-]/[C_2H] < 0.007\%$, and $[C_4H^-]/[C_4H] < 0.05\%$.
Conclusions. Our models can reasonably match the observed column densities of most hydrocarbons (within factors of <3). Since the observed spatial distribution of the C_2H and c-C_3H_2 emission is similar but does not follow the PAH emission, we conclude that, in high UV-flux PDRs, photodestruction of PAHs is not a necessary requirement to explain the observed abundances of the smallest hydrocarbons. Instead, gas-phase endothermic reactions (or with barriers) between C^+, radicals, and H_2 enhance the formation of simple hydrocarbons. Observations and models suggest that the $[C_2H]/[c$-$C_3H_2]$ ratio (~ 32 at the PDR edge) decreases with the UV field attenuation. The observed low cyclic-to-linear C_3H column density ratio (≤ 3) is consistent with a high electron abundance (x_e) PDR environment. In fact, the poorly constrained x_e gradient influences much of the hydrocarbon chemistry in the more UV-shielded gas. The inferred hot rotational temperatures for C_4H and l-C_3H^+ also suggest that radiative IR pumping affects their excitation. We propose that reactions of C_2H isotopologues with $^{13}C^+$ and H atoms can explain the observed $[C^{13}CH]/[^{13}CCH] = 1.4 \pm 0.1$ fractionation level.

Key words. astrochemistry – surveys – photon-dominated region (PDR) – ISM: molecules – ISM: abundances

1. Introduction

Bright photodissociation regions (PDRs) are the transition layers between the ionised gas directly irradiated by strong UV fields (e.g. from massive OB stars) and the cold neutral gas shielded from radiation (e.g. Tielens & Hollenbach 1985). Photodissociation regions are found in many astrophysical environments and spatial scales, from the nuclei of starburst galaxies (e.g. Fuente et al. 2008) to the illuminated surfaces of proto-planetary disks (e.g. Agúndez et al. 2008a). All of them show a characteristic chemistry that can be understood in terms of an active UV photochemistry. The closest and brightest example of such PDR is the so-called Orion Bar, at the interface between

the Orion Molecular Cloud (OMC) and the H II region illuminated by the Trapezium stars. The Orion Bar is a prototypical high-UV flux, hot PDR, with a far-UV radiation field (FUV, 6.0 eV $< h\nu < 13.6$ eV) of a few 10^4 times the mean interstellar field (Marconi et al. 1998). Because of its proximity (414 ± 7 pc to the Orion Nebula Cluster, Menten et al. 2007), the Orion Bar offers the opportunity to determine the chemical content, spatial stratification of different species, and chemical formation routes in UV illuminated gas.

The transition from ionised to neutral gas in the Orion Bar has been extensively mapped in various atomic and molecular tracers (see e.g. Tielens et al. 1993; Hogerheijde et al. 1995; van der Werf et al. 1996; Walmsley et al. 2000; Ossenkopf et al. 2013). The detailed analysis of these observations suggested an inhomogeneous density distribution. The most commonly accepted scenario is that an extended gas component, with mean gas densities of 10^{4-5} cm^{-3}, causes the chemical stratification seen perpendicular to the dissociation front as the FUV field is

---

attenuated. In this context, the low energy transitions of different molecules, including CO, would arise from this extended interclump medium (Hogerheijde et al. 1995; Jansen et al. 1995; Simon et al. 1997; van der Wiel et al. 2009; Habart et al. 2010; van der Tak et al. 2013). In addition, another component of higher density clumps was invoked to fit the observed high-J CO, CO^+, and other high density and temperature tracers (Burton et al. 1990; Parmar et al. 1991; Stoerzer et al. 1995; Young Owl et al. 2000; Batrla & Wilson 2003). Owing to its small filling factor, this clumpy structure would allow FUV radiation to permeate the region. Although this scenario is still controversial, recent 3D models of the Orion Bar structure are compatible with this morphology (Andree-Labsch et al. 2014).

Depending on the FUV field strength and on the gas density, different processes contribute to the gas heating. Photoelectrons from polycyclic aromatic hydrocarbons (PAHs) and grains heat the interclump gas from ~85 K (Hogerheijde et al. 1995) to ≳500 K at the dissociation front (Allers et al. 2005; van der Werf et al. 2013). In addition, the temperature at the surface ($A_V < 1$) of dense clumps can go above 1000 K because collisional deexcitation of vibrationally excited H_2 dominates the gas heating (Burton et al. 1990). The presence of both hot gas and FUV-pumped, vibrationally excited H_2 (observed in the near-IR at ~2.1 μm) triggers a distinctive PDR chemistry where highly endothermic reactions and reactions with large activation barriers can proceed quickly (Agúndez et al. 2010). Examples of this peculiar chemistry are the reactions of H_2 with C^+, O, and S^+ (all very abundant in PDR edges) that allow the formation of CH^+, OH, and SH^+ and represent the first steps of the PDR chemistry (see recent detections by Habart et al. 2010; Goicoechea et al. 2011; Nagy et al. 2013; Müller et al. 2014). In addition to these simple hydrides, the abundance of carbon bearing radicals (CN, C_2H, c-C_3H_2) was found to increase close to the dissociation front (e.g. Jansen et al. 1995; Fuente et al. 1996).

The formation and chemical behaviour of hydrocarbon molecules in the interstellar medium (ISM) are long standing problems in astrochemistry. Since the early 1970s it has been evident that hydrocarbons, the simplest organic molecules, are ubiquitous in the ISM (e.g. Tucker et al. 1974; Thaddeus et al. 1985a,b; Yamamoto et al. 1987b). These molecular species have peculiar chemical structures (e.g. very rigid compounds such as polyynes or cumulenes) and are quite reactive and polar because of the presence of unpaired electrons on the carbon atoms (e.g. carbenes). Owing to their abundance and ubiquity, these molecules often have a bright rotational spectrum which makes them easily detected in the ISM (e.g. Guelin et al. 1978; Cernicharo et al. 1991a). Cernicharo et al. (1984) were the first to show that carbon chain radicals and cyanopolyynes were present in several cold cores in the Taurus region. The C_2H and c-C_3H_2 molecules, among the most abundant hydrocarbons, are detected in very different environments, ranging from diffuse clouds (e.g. Lucas & Liszt 2000) to cold dark clouds (e.g. Fossé et al. 2001). They have even been detected towards extragalactic sources (Fuente et al. 2005; Meier & Turner 2005, 2012; Aladro et al. 2011). The longest hydrocarbon chain radicals found in the ISM so far are C_6H, C_7H, and C_8H (Cernicharo et al. 1987; Guelin et al. 1987, 1997; Cernicharo & Guelin 1996). Despite many studies on their abundance and formation routes in different environments (e.g. Sakai et al. 2010; Liszt et al. 2012; Pilleri et al. 2013), the synthesis of hydrocarbons in the ISM is still poorly understood. Observations towards diffuse interstellar clouds and low-FUV flux PDRs suggest that the inferred abundances are significantly higher than current pure gas-phase

model predictions (e.g. Fossé et al. 2000; Fuente et al. 2003). The good spatial correlation between the hydrocarbon emission and the PAH emission towards the Horsehead PDR led Pety et al. (2005) to suggest that the photo-erosion of PAHs and small carbonaceous grains may dominate the formation of small hydrocarbon molecules. In more strongly irradiated environments like the Orion Bar (>300 times higher FUV radiation fluxes than the Horsehead) the situation may not necessarily be the same. In particular, the molecular gas attains much higher temperatures and new gas-phase formation routes, endothermic reactions, and reactions with activation energy barriers, become efficient.

In the context of investigating the chemistry in hot molecular gas irradiated by strong FUV radiation fields, we have performed a complete millimetre line survey towards the Orion Bar PDR. This line survey has allowed us to unveil the molecular content, accurately determine the abundances of the detected species, and constrain their formation mechanisms. Approximately 40% of the detected lines arise from small hydrocarbon molecules. In this paper, we report all hydrocarbon lines detected and investigate the spatial distribution of C_2H and c-C_3H_2 throughout the region. The paper is organised as follows. In Sect. 2 we describe the line survey and the mapping observations. In Sect. 3 we report the observational features of the detected hydrocarbons, while in Sect. 4 we present the C_2H and c-C_3H_2 integrated line-intensity maps at 3 mm and 1 mm. The data analysis is explained in Sect. 5 and the PDR chemical models of hydrocarbons are reported in Sect. 6. In Sect. 7 we discuss the results, and finally in Sect. 8 we summarise the main conclusions. The results of the whole survey will be reported in a subsequent paper.

2. Observations and data reduction

2.1. Line survey

In 2009 we started a shallow line survey with the aim to investigate the chemistry of the Orion Bar PDR. The observations were conducted with IRAM 30 m telescope at Pico Veleta (Sierra Nevada, Spain), at the position $\alpha_{2000} = 05^h 35^m 20.8^s$, $\delta_{2000} = -05°25'17.0''$, corresponding to the dissociation front of the Orion Bar, close to what Stoerzer et al. (1995) call the "CO^+ peak".

We began the survey with the EMIR receivers (E0 and E1) and WILMA (wideband line multiple autocorrelator) backend, the only broadband backend at that time. In April 2012, with the implementation of the new FFTS (fast fourier transform spectrometer) backends, we began a higher spectral resolution line survey and since then we have observed with the E0, E2, and E3 receivers at 200 kHz spectral resolution covering a total of 217 GHz along 3, 2, 1, and 0.8 mm bands with both backends. The receivers were configured in dual sideband (2SB) for bands E0, E2, and E3 (covering 16 GHz of instantaneous bandwidth per polarization), and in single sideband (SSB) for E1 (8 GHz per polarization). The observing procedure was position switching (PSW) with the reference position located at an offset ($-600''$, $0''$) to avoid the extended molecular emission from the OMC complex. The telescope pointing and focus were checked every two hours through azimuth-elevation cross scans on the nearby continuum source (the 0420-014 quasar). Atmospheric opacity was corrected by calibrating the data using the ATM code (Cernicharo 1985, IRAM internal report; Pardo et al. 2001). The antenna temperature, T_A^*, was converted to the main beam temperature, T_{MB}, through the $T_{MB} = T_A^*/\eta_{MB}$ relation, where η_{MB} is the antenna efficiency, which is defined as the ratio between main beam efficiency, B_{eff}, and forward efficiency, F_{eff}. All intensities in tables and figures are in main beam
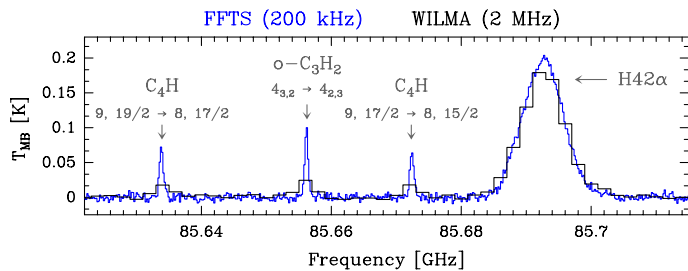
Fig. 1. Zoom to the 3 mm window where both FFTS (200 kHz spectral resolution) and WILMA spectra (2 MHz spectral resolution) are shown. Both data have similar rms(channel) × channel width [K km s^{-1}] noise values, but molecular line profiles are only resolved with the FFTS. The broad hydrogen recombination lines are resolved at both resolutions.

Table 1. Observed frequency ranges and telescope parameters.

Rec.[a]	Obs. Freq.[b] [GHz]	Backend	η_{MB}[c]	HPBW[d] [arcsec]
E0	80.0–117.0	FFTS	0.87–0.82	30.8–21.0
E1	128.0–175.6	WILMA	0.80–0.74	19.1–14.0
E2	202.0–275.0	FFTS	0.70–0.56	12.2–8.9
E3	275.0–304.5	FFTS	0.56–0.50	8.9–8.1
	327.8–359.0	FFTS	0.46–0.40	7.5–6.9

Notes. [a] Emir receiver. [b] Observed frequency range. [c] Antenna efficiencies. [d] The half power beam width can be well fitted by HPBW[arcsec] ≈ 2460/Frequency[GHz].

temperature. A local standard of rest (LSR) of 10.7 km s^{-1} has been assumed in the line survey target position in the Orion Bar dissociation front. Table 1 shows an overview of the frequency ranges observed with each backend, as well as the variation in the telescope efficiencies, η_{MB}, and the half power beam width (HPBW) across the covered frequency range.

The intrinsic molecular line widths towards the Orion Bar PDR are typically ~2 km s^{-1}, so the spectral resolution of the backend has to be high enough to resolve the line profiles. The spectral resolution of WILMA backend does not allow the narrow molecular line profiles of the PDR to be resolved, and therefore it only gives information about the integrated line intensity. Most of the hydrocarbon molecular lines were observed with the FFTS backends which does allow the molecular lines to be resolved, thus providing line profile information. Hydrogen recombination lines from ionised gas in the adjacent H II region are resolved with both backends because they are intrinsically broad (Fig. 1).

The data were reduced using the CLASS software of the GILDAS package[1]. A polynomial baseline of low order (typically second or third order) was subtracted from each ~200 MHz wide spectrum after all scans were added. The rms noise of our observations obtained by integration during ~4 h ranges between 4 mK and 20 mK. Despite the good attenuation of the image band signal (>10 dB), bright lines arising from the image band had to be eliminated in the data processing. The image band lines were identified following the procedure developed by Tercero et al. (2010) according to which each setting was repeated at a slightly shifted frequency (~50 MHz). The change of the frequency for the lines coming from the image

side band when shifting the observing sky frequency allows all possible contaminating lines of the image band to be identified and removed.

2.2. Maps

The line survey was complemented with maps of the line emission distribution of different species. In particular we present maps of the C$_2$H ($N = 1 \rightarrow 0$ and $3\rightarrow2$) and c-C$_3$H$_2$ ($J_{K_a, K_c} = 2_{1,2} \rightarrow 1_{0,1}$ and $6_{1,6} \rightarrow 5_{0,5}$) line emission. The spectral mapping observations were also obtained at the IRAM 30 m telescope in two separate runs. The 3 mm maps were obtained in July 2012, in approximately 3 h integration time for each configuration. We used the EMIR receivers and the FFTS spectrometers at 50 kHz resolution to get accurate velocity information. Because of the limited bandwidth of these high resolution spectrometers, we used two different configurations for C$_2$H and c-C$_3$H$_2$. The 1 mm maps were obtained in December 2012, using the FFTS at 200 kHz resolution. The maps were obtained using the on-the-fly observing mode, with an OFF position at ($-600''$, $0''$) relative to the map centre. This position is free of any emission in these two tracers. Data processing consisted in a linear baseline subtraction in each observed spectra. The resulting spectra were finally gridded through convolution by a Gaussian.

3. Results: small hydrocarbon detections

The millimetre molecular line survey of the Orion Bar covers a bandwidth of ~220 GHz in which more than 200 lines from small hydrocarbon molecules have been identified. The detected lines were attributed to nine different molecules, from the simplest carbon-chain molecule, C$_2$H, to more complex molecules with five atoms such as C$_3$H$_2$. Lines from two isotopologues (^{13}CCH and C^{13}CH) and one cation (l-C$_3$H$^+$) were detected. No lines from anions or vibrationally excited states of hydrocarbons were identified. Line assignment was carried out using Cernicharo's own spectral catalogue (MADEX[2], Cernicharo 2012) and two molecular databases with public access: JPL (Pickett et al. 1998)[3] and CDMS (Müller et al. 2001, 2005)[4].

In this section we individually introduce the detected hydrocarbons and summarise their most important spectroscopic features. The studied species are classified according to their empirical formula: C$_2$H, C$_3$H$^+$, C$_3$H, C$_3$H$_2$, and C$_4$H. Table 2 summarises the dipole moments and electronic ground states of the detected species. The spectroscopic and observational line parameters of the detected hydrocarbons are given in Appendix B.

3.1. C$_2$H

The C$_2$H radical was first detected in the ISM by Tucker et al. (1974) who detected four components of the $N = 1 \rightarrow 0$ rotational transition in several sources associated with massive star-forming regions. Since then, C$_2$H has been detected in a wide variety of sources including the circumstellar envelopes around

---

[1] http://www.iram.fr/IRAMFR/GILDAS/

Table 2. Dipole moments (μ), electronic ground state (E.G.S.), and number of hydrocarbon detected lines in this work.

Molecule	μ	E.G.S.	Detected	Ref.
	[Debye]		Lines	
C_2H	0.77	$^2\Sigma^+$	25	1
^{13}CCH	0.77	$^2\Sigma^+$	7	2
$C^{13}CH$	0.77	$^2\Sigma^+$	8	2
l-C_3H^+	3.00	$^1\Sigma^+$	9	3
l-C_3H	3.55	$^2\Pi^+$	25	1
c-C_3H	2.40	$^2B_2$	24	4
c-C_3H_2	3.43	$^1A_1$	50	5
l-H_2C_3	4.10	$^1A_1$	18	6
C_4H	0.87	$^2\Sigma^+$	40	1

References. (1) Woon (1995); (2) The dipole moment is assumed to be the same as for the C_2H; (3) Pety et al. (2012); (4) Yamamoto et al. (1987b); (5) Kanata et al. (1987); (6) DeFrees & McLean (1986).

carbon-rich evolved stars (De Beck et al. 2012, and references therein), diffuse clouds (Lucas & Liszt 2000), cold dark clouds (Wootten et al. 1980), and even in extragalactic sources (Martín et al. 2006). The isotopologues of the ethynyl radical, ^{13}CCH, $C^{13}CH$, and CCD, have also been detected in the ISM, first observed towards the Orion A ridge and Orion KL star forming core (3′N, 1′E) (Saleck et al. 1992, 1994; Combes et al. 1985; Vrtilek et al. 1985).

3.1.1. Ethynyl: $^{12}C_2H$

The C_2H hydrocarbon is a linear molecule with $^2\Sigma^+$ electronic ground state, therefore its rotational spectrum shows spin rotation interaction and hyperfine structure. The quantum numbers designating the energy levels are N, J, and F. Spin doubling ($J = N + S$) is produced by the coupling between the rotational angular momentum, N, and the unpaired electron spin, S, while the hyperfine structure ($F = J + I$) is due to the coupling of the angular momentum, J, and the spin of the hydrogen nucleus, I. Electric dipole selection rules require $\Delta F = 0$ (with $0 \leftrightarrow 0$) and $\Delta F = \pm 1$, so the $N = 1 \to 0$, $2 \to 1$, $3 \to 2$, and $4 \to 3$ transitions detected in this work split into 6, 11, 11, and 11 allowed hyperfine components, respectively. The C_2H spectroscopic constants were obtained from a simultaneous fit of both laboratory and astronomical data by Gottlieb et al. (1983a) and Müller et al. (2000).

We have identified a total of 25 lines of C_2H. They consist of four sets of rotational transitions corresponding to the hyperfine splitting of the $N = 1 \to 0$ to $4 \to 3$ transitions. The six hyperfine components of the lowest energy rotational transition ($N = 1 \to 0$) are well separated in frequency. There are no significant differences in the line widths ($\Delta v \approx 3$ km s^{-1}) and line peak velocities. As shown in Table 3, the relative intensities of the observed $N = 1 \to 0$ hyperfine components agree with the expected relative intrinsic intensities. This shows that the lines are optically thin and do not show hyperfine emission anomalies.

Nine and five spectral lines of each $N = 3 \to 2$ and $4 \to 3$ hyperfine transition have also been detected at high resolution, but some hyperfine components are partially or fully overlapped. Five lines of the $N = 2 \to 1$ transition, corresponding to seven hyperfine rotational transitions, were detected at 2 MHz spectral resolution. The hyperfine structure is not fully

Table 3. Line intensities of the detected C_2H $N = 1 \to 0$ lines.

Transition	$S_{ij}{}^a$	$T_{MB}{}^b$	Relative I^c [x100]	
$(J, F)_{N=1} \to (J, F)_{N=0}$		[K]	LTE^d	Obs.^{e}
$(3/2, 1) \to (1/2, 1)$	0.17	0.14	4.25	4.20
$(3/2, 2) \to (1/2, 1)$	1.67	1.39	41.72	41.91
$(3/2, 1) \to (1/2, 0)$	0.83	0.69	20.73	20.73
$(1/2, 1) \to (1/2, 1)$	0.83	0.68	20.73	20.56
$(1/2, 0) \to (1/2, 1)$	0.33	0.28	8.32	8.42
$(1/2, 1) \to (1/2, 0)$	0.17	0.14	4.25	4.19

Notes. $^{(a)}$ Theoretical line strengths. $^{(b)}$ Observed line intensities in mean beam temperature. $^{(c)}$ Relative intensities. $^{(d)}$ Expected relative intensities ($S_{ij}/\sum S_{ij}$), assuming that lines are optically thin ($\tau < 1$). $^{(e)}$ Observed relative intensity ($T_{MB_{ij}}/\sum T_{MB_{ij}}$).

resolved and some lines are overlapped. The quantum numbers of the detected C_2H transitions, their spectroscopic parameters, and the results from fitting the line profiles with Gaussians are listed in Table B.1. In Fig. 2 we present the spectra of the $N = 1 \to 0$ to $4 \to 3$ rotational lines.

3.1.2. ^{13}CCH and $C^{13}CH$

We have detected six lines of ^{13}CCH and seven lines of its isotopomer $C^{13}CH$ in the 1 mm band (252.4 GHz and 255.7 GHz, respectively), corresponding to the $N = 3 \to 2$ rotational transition (Fig. 3). Observations of the ^{13}C isotopic species of ethynyl have been quite limited. To our knowledge, this is the first detection of both isotopologues in a PDR. The rotational spectrum and hyperfine structure of both ^{13}CCH and $C^{13}CH$ are described in detail in McCarthy et al. (1995). Table B.2 lists the spectroscopic and observational line parameters. The main hyperfine line of $C^{13}CH$ is more intense than the main hyperfine line of ^{13}CCH by a factor of 1.4 ± 0.1 (3σ), where the quoted uncertainty is three times the standard deviation. This difference suggests that fractionation processes differently affect the two ^{13}C isotopes of C_2H (see Sect. 7.2).

3.2. C_3H^+

We have also detected a series of lines that Pety et al. (2012) originally attributed to l-C_3H^+ in the Horsehead Nebula PDR (see also McGuire et al. 2013). This detection has been recently confirmed in the laboratory (Brünken et al. 2014) and by quantum chemical calculations (Botschwina et al. 2014). The linear C_3H^+ is an essential intermediate in the gas-phase synthesis of hydrocarbons through ion-molecule reactions.

Using the CSO telescope, McGuire et al. (2014) searched for l-C_3H^+ towards a large sample of galactic sources. They only detected the molecule towards the Orion Bar (three rotational lines). l-C_3H^+ presents a simple rotational spectrum, with $J + 1 \to J$ transitions. Here we present nine rotational lines, from $J = 4 \to 3$ to $13 \to 12$, the highest frequency line detected so far. Figure 4 shows the detected lines and Table B.3 summarises the observed parameters.

3.2.1. Improved l-C_3H^+ rotational constants

We have fitted all laboratory lines measured by Brünken et al. (2014) together with those measured towards the Horsehead by Pety et al. (2012) and those reported here in the Orion Bar. Since we detect up to the $J = 13 \to 12$ line, we can better constrain the
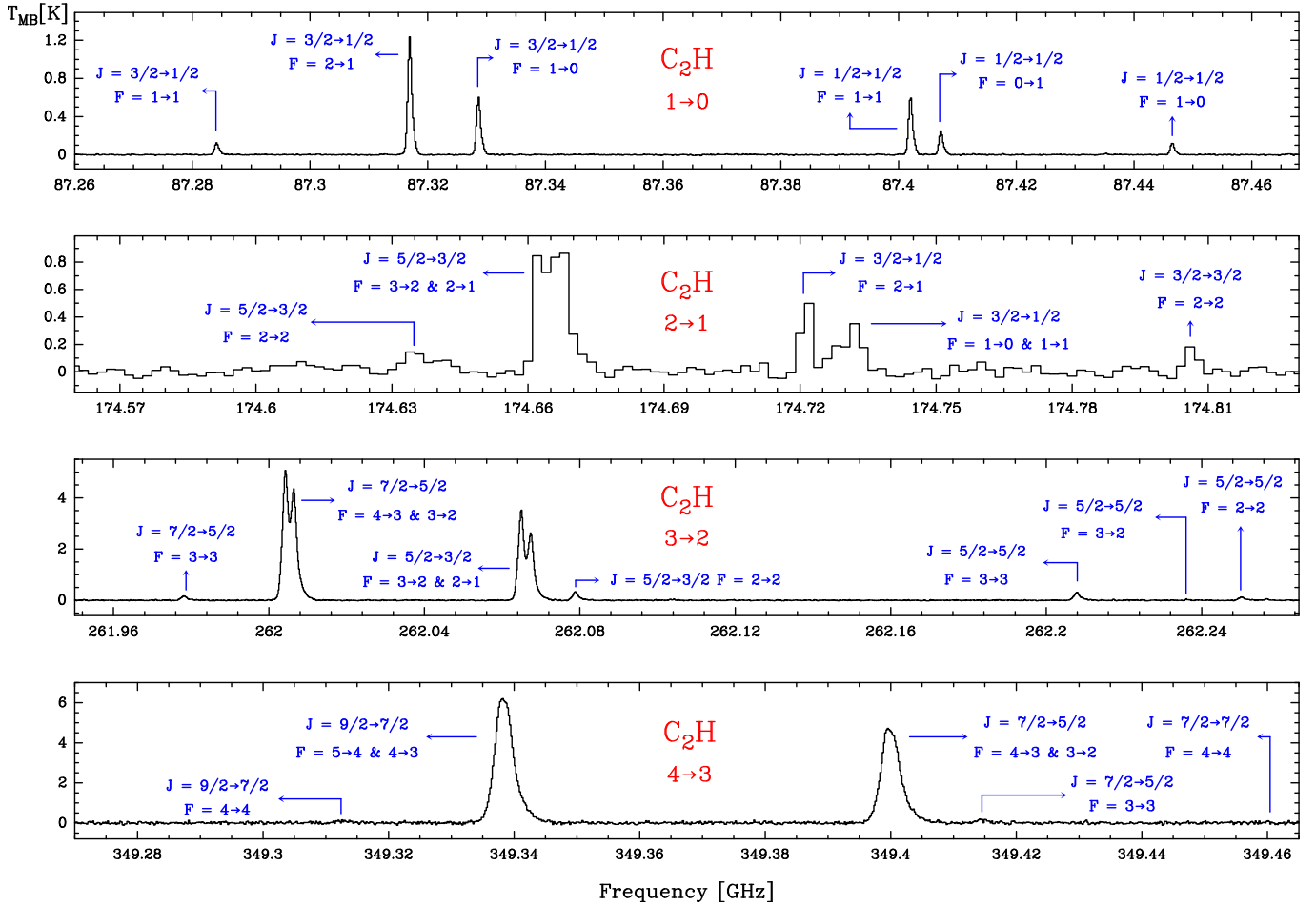
Fig. 2. Detected C_2H hyperfine structure lines of the $N = 1 \rightarrow 0$, $2 \rightarrow 1$, $3 \rightarrow 2$, and $4 \rightarrow 3$ rotational transitions. The $N = 2 \rightarrow 1$ transition was observed at 2 MHz resolution while the $N = 1 \rightarrow 0$, $3 \rightarrow 2$, and $4 \rightarrow 3$ transitions were detected at 200 kHz. Hyperfine structure are only fully resolved in the $N = 1 \rightarrow 0$ transition. The fine and hyperfine components are labelled with the quantum numbers J and F. For clarity, we have not included the labels of the transitions that were too weak to be detected.
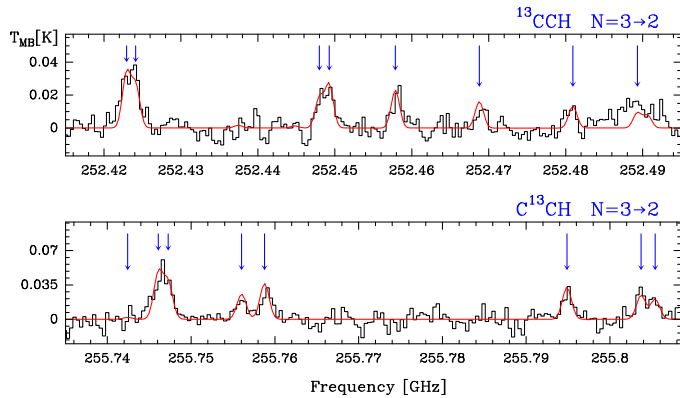
**Fig. 3.** Detection of the $N = 3 \rightarrow 2$ hyperfine structure of ^{13}CCH (*top*) and $C^{13}CH$ (*bottom*) in the Orion Bar PDR (black histogram spectra). A LTE model is overlaid in red (see Sect. 5.2). The position of hyperfine transitions are indicated by the blue arrows. We note the different abscissa and ordinate axis scales in both spectra.

distortion constants. We derive $B = 11244.94793(116)$ MHz and $D = 7.66055(853)$ kHz with a correlation coefficient of 0.77 between both constants. The standard deviation of the fit is 47 kHz. The rotational constants obtained by merging the laboratory measurements and the astronomical data have two times better uncertainties for B and almost one order of magnitude better

accuracy for D. An attempt to fit the distortion constant H produced a slightly better fit (43 kHz), with $H = (2 \pm 1) \times 10^{-7}$ MHz, but with this constant strongly correlated with D and with a significant degradation of the uncertainty of the other constants. Higher J lines will be needed to derive the sextic order distortion constant of l-C_3H^+. Nevertheless, it is clear that the molecule is rather floppy because the D value is high, even higher than that of C_3. If the lowest energy bending mode of l-C_3H^+ is as low as that of C_3, we estimate that this mode can be populated for gas temperatures around ~30–40 K. The lines from the bending mode will consist of a series of doublets (l-doubling), blue-shifted with respect to the lines of the ground vibrational mode. Each member of these doublets will pertain to a series of harmonically related frequencies. We have not found any series of lines with these attributes at the sensitivity level of our survey. Another related molecule having low lying bending modes is C_4H (see discussion in Sect. 7.1).

3.3. C_3H

The C_3H radical is found in the ISM in two isomeric forms: as a linear chain, l-C_3H, and as a three-carbon ring, c-C_3H. Both isomers were first detected by their rotational transitions at millimetre wavelengths in TMC-1 (Thaddeus et al. 1985a; Yamamoto et al. 1987b). The c-C_3H radical is more energetically stable than l-C_3H by ~860 K (Sheehan et al. 2008).
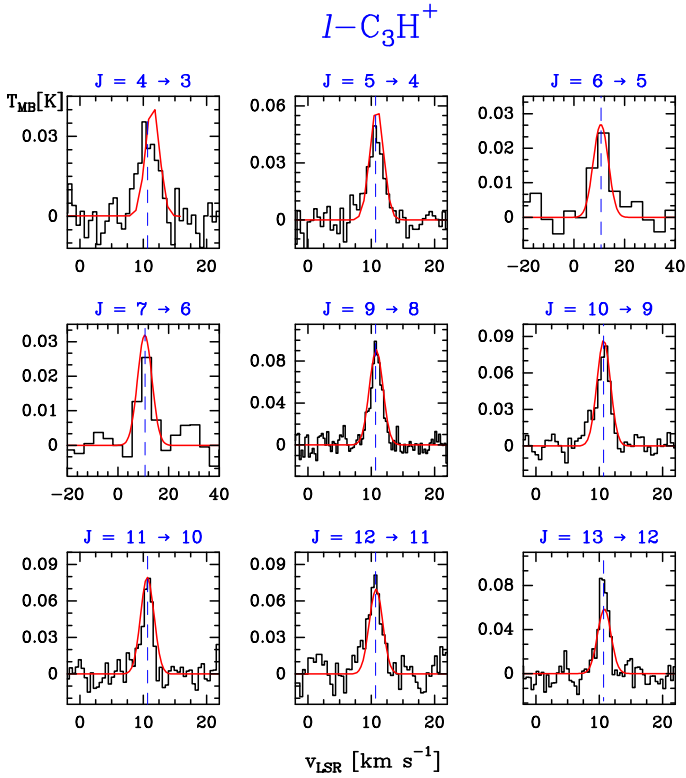
$l-C_3H^+$

Fig. 4. Series of l-C_3H^+ lines detected in the Orion Bar PDR. Spectra of the $J = 4 \to 3$, $5 \to 4$, $9 \to 8$, $10 \to 9$, $11 \to 10$, $12 \to 11$, and $13 \to 12$ rotational transitions of l-C_3H^+ observed at 200 kHz spectral resolution, and $6 \to 5$ and $7 \to 6$ observed at 2 MHz (black histogram spectra). A LTE model is overlaid in red (see Sect. 5.2). The dashed lines indicate the LSR velocity (10.7 km s^{-1}) of the Orion Bar PDR.

3.3.1. Propynylidyne: linear-C₃H

The linear carbon chain, l-C_3H, has a $^2\Pi$ electronic ground state. Its laboratory millimetre wave spectrum was reported by Gottlieb et al. (1985, 1986). The spin-orbit interaction results in two rotational ladders, $^2\Pi_{3/2}$ and $^2\Pi_{1/2}$, with intra-ladder and much weaker cross-ladder transitions. Furthermore, each rotational transition is split by Λ-type doubling due to the nuclei rotation and the unpaired electron motion. In interstellar conditions, only the lower transitions show fully-resolved hyperfine transitions.

We have detected 25 lines of l-C_3H, consisting of (i) 12 lines in the $^2\Pi_{1/2}$ ladder ($E_u/k \leq 102.2$ K); and (ii) 13 lines in the $^2\Pi_{3/2}$ ladder ($E_u/k \leq 75$ K). The l-C_3H lines are rather weak and show very narrow lines profiles ($\Delta v \leq 1.6$ km s^{-1}). The hyperfine structure has only been partially resolved in the lowest detected rotational levels. Figure 5 shows three l-C_3H spectra, which are representative examples of the partially resolved hyperfine structure and the Λ-doublet components. Spectroscopic and observational parameters of l-C_3H are summarised in Table B.4.

3.3.2. Cyclopropynylidyne: cyclic-C₃H

The cyclic form, c-C_3H, is an a-type asymmetric top molecule. The c-C_3H rotational level transitions, given by $N_{K_aK_c}$, are split into fine and hyperfine levels (labelled by the quantum numbers J and F, respectively). The rotational transitions are governed by the $\Delta J = 0$ and ± 1 selection rules. The laboratory spectrum was first measured by Lovas et al. (1992) and Yamamoto & Saito (1994).
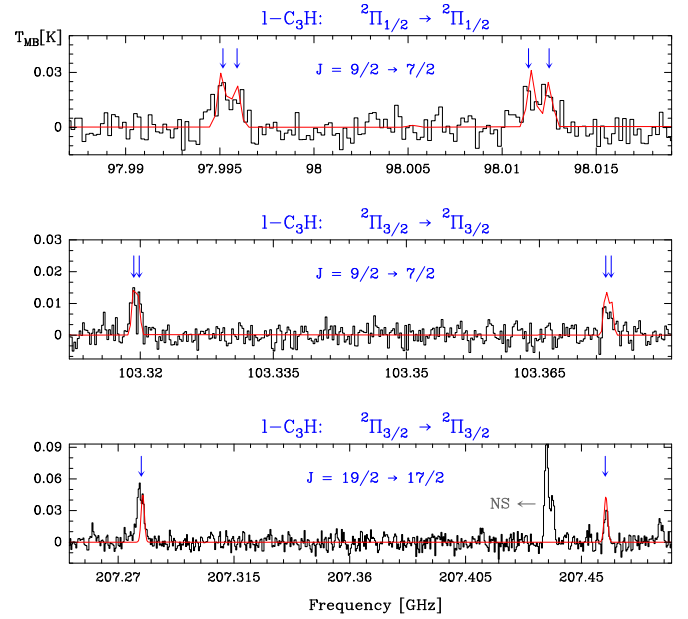
Fig. 5. Examples of l-C_3H detected lines (black histogram spectra). A LTE model is overlaid in red (see Sect. 5.2). l-C_3H lines are indicated by blue arrows. The other spectral features appearing in the selected windows are labelled with their corresponding identification.
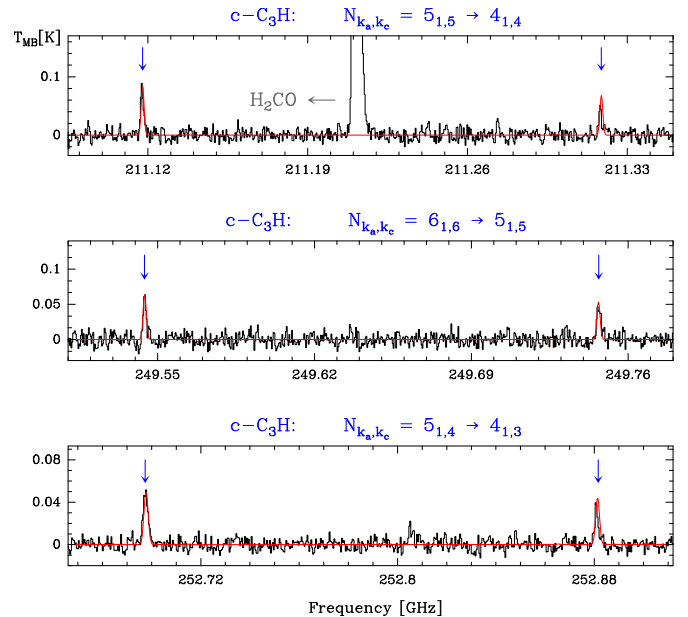
Fig. 6. c-C_3H spectra observed in the 1 mm band (black histogram spectra). A LTE model is overlaid in red (see Sect. 5.2). c-C_3H lines are indicated by blue arrows. The other spectral features appearing in the selected windows are labelled with their corresponding identification.

We have detected 24 lines of c-C_3H. These consist of ten sets of rotational transitions with fine and hyperfine structure lines ($E_u/k \leq 55$ K). No transition is completely resolved in its hyperfine components. Examples of c-C_3H spectra are shown in Fig. 6 and the line parameters are listed in Table B.5.

3.4. C₃H₂

Interstellar molecules with the elemental formula C_3H_2 belong to a type of compounds known as carbenes. They are highly reactive because of the two non-bonded electrons on one of the three carbon atoms. Two structural isomers are observed: cyclic

and linear. The cyclic one, the first organic ring detected in the ISM (Thaddeus et al. 1985b; Vrtilek et al. 1987), is ~6960 K more stable than the linear form (Dykstra et al. 1979; DeFrees & McLean 1986). Cernicharo et al. (1991a) observed one of the C_3H_2 linear isomers in TMC-1 (hereafter l-H_2C_3) characterised by two or more consecutive double carbon bonds with two non-bonded electrons on the terminal carbon (Cernicharo et al. 1991b; Langer et al. 1997). Although the cyclic form is more abundant and ubiquitous, both C_3H_2 isomers are widely observed in the ISM. The cyclic and linear isomers of C_3H_2 have two indiscernible off-axis hydrogen atoms which impose an additional ortho-para symmetry. The rotational spectra of both isomers were originally reported by Vrtilek et al. (1987, 1990).

3.4.1. Cyclopropenylidene: cyclic-C_3H_2

The cyclic isomer of C_3H_2 is a three-carbon ring with (i) two carbon atoms linked by a double bond (semirigid structure); (ii) one extremely reactive bivalent carbon atom which makes it highly polar (with a large dipole moment of 3.4 Debye); and (iii) two equivalent off-axis hydrogen atoms (responsible for the ortho-para symmetries).

The c-C_3H_2 molecule is an oblate asymmetric top with an asymmetric parameter $\kappa = -0.69$, b-type rotational transitions (ΔK_a and $\Delta K_c = \pm 1$ main selection rules), and without fine or hyperfine structure. Ortho and para levels are described by $K_a + K_c =$ odd and even values, respectively. We have detected 23 rotational transitions of ortho c-C_3H_2 with $E_u/k \leq 84.6$ K, 17 rotational transitions of para c-C_3H_2 with $E_u/k \leq 54.7$ K, and 10 lines corresponding to several fully overlapped ortho-para transitions. The line profiles of spectrally resolved ortho and para lines at 1 mm are shown in Fig. 7. The line parameters are listed in Table B.6.

3.4.2. Propadienylidene: linear-H_2C_3

In addition to being a carbene, the linear isomer is a cumulene, with a linear and rigid backbone of three carbon atoms linked by adjacent double bonds [H_2–C=(C=)$_n$C:]. Because of the linear symmetry and the low mass of the two off-axis equivalent hydrogen atoms, the rotational spectrum of propadienylidene is a nearly prolate top with an asymmetric parameter $\kappa = -0.997$ and a-type R-branch selection rules which involve $\Delta J = 1$, $\Delta K_a = 0$, and $\Delta K_c = 1$ transitions. Para levels have even values of K_a, while ortho levels have odd values.

We observed the lowest para ladder ($J_{0,J} \rightarrow J - 1_{0,J-1}$) with rotational transitions separated by ~20.8 GHz, and the lowest ortho ladder ($K_a = 1$), that shows K-type doublets with the two lines displaced by several GHz. Transitions with $K_a > 1$ have not been detected. We have identified 13 lines of ortho species, but only 6 lines for the para species (both with $E_u/k \leq 90.8$ K). The line profiles of spectrally resolved ortho and para lines at 1 mm are shown in Fig. 8. Table B.7 gives the observed line parameters.

3.5. C_4H

The linear butadiynyl, C_4H, is a univalent radical and the simplest example of polyynes, a type of organic species in which molecular structure have single and triple bonds in alternate positions (–C≡C–)$_n$, with $n > 1$. This molecule was first identified in the circumstellar envelope of IRC+10216 (Guelin et al. 1978). Its laboratory microwave spectrum in the ground vibrational state was first obtained by Gottlieb et al. (1983b).

cyclic C_3H_2
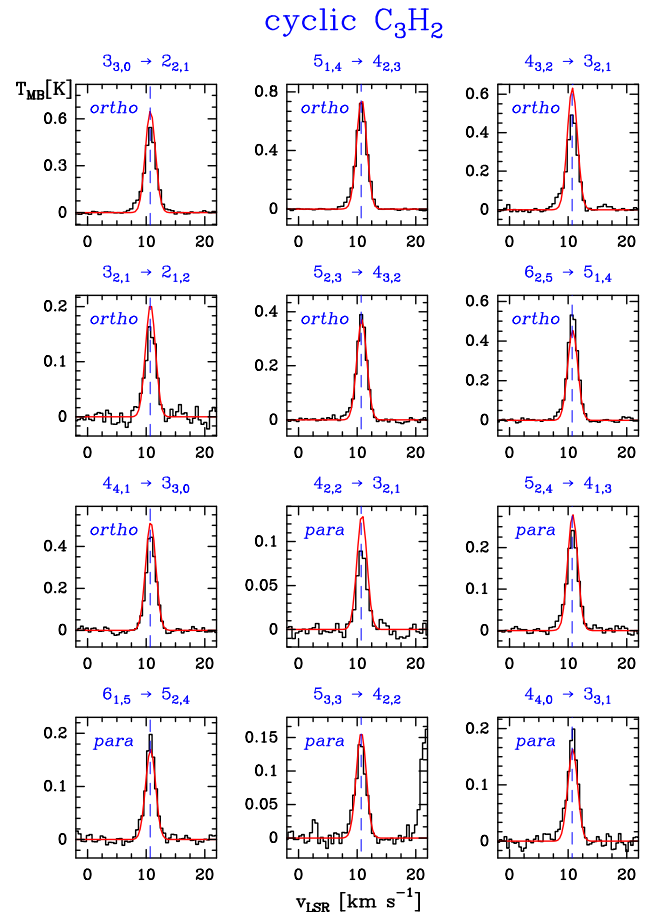
Fig. 7. Observed c-C_3H_2 (black histogram spectra). Best fit LVG model is shown overlaid in red (see Sect. 5.4). The dashed lines indicate the LSR velocity (10.7 km s^{-1}) of the Orion Bar PDR.

linear H_2C_3
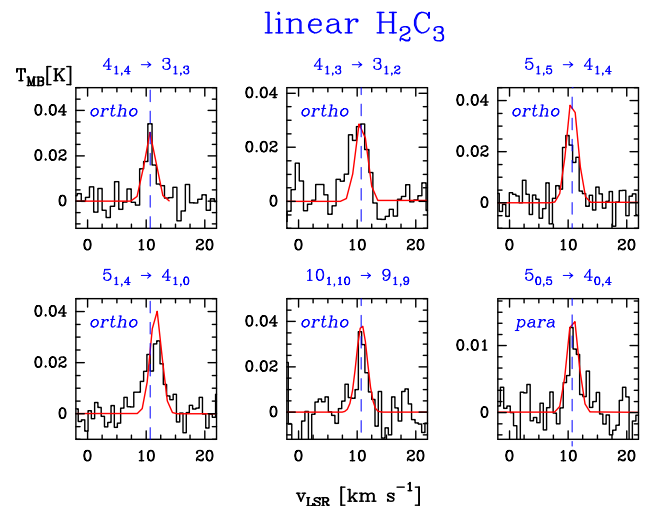
Fig. 8. Observed l-H_2C_3 (black histogram spectra). Best fit LTE model is shown overlaid in red (see Sect. 5.2). The dashed lines indicate the LSR velocity (10.7 km s^{-1}) of the Orion Bar PDR.

The C_4H radical has the same symmetry and electronic ground state ($^2\Sigma^+$) as C_2H, therefore its rotational levels are also split into fine and hyperfine structure. This hyperfine splitting is only fully resolved in the lowest rotational transitions (e.g. Bell et al. 1982, 1983; Guelin et al. 1982). As a consequence, in the studied spectral range, the strongest rotational transitions

are doublets. Forty lines of C_4H consisting of 20 successive doublets starting from $N = 9 \to 8$ have been identified in this work, most of them with high spectral resolution. The C_4H doublets show spectral features that allow us to distinguish them easily: (i) each pair of lines is separated by $\sim$38.5 MHz; and (ii) the lowest frequency transition of each doublet is slightly stronger than the second. This is in perfect agreement with the theoretical line strength. Figure 9 shows some of the strongest lines detected at high spectral resolution in the 3 mm and 1 mm bands. Assignments of the line components, as well as the spectroscopic and observed line parameters of the detected lines are given in Table B.8.

4. Spatial distribution of C_2H, c-C_3H_2, and PAHs

Early mapping observations of the Orion Bar (e.g. Tielens et al. 1993; van der Werf et al. 1996) confirmed the PAH/H_2/CO spatial stratification predicted by PDR models (e.g. Tielens & Hollenbach 1985). Figure 10 shows the IRAC 8 μm band emission along the Orion Bar taken from the Spitzer archive (colour scale). Analysing the ISOCAM mid-IR spectrum of the Bar with the fitting tool PAHTAT (Pilleri et al. 2012) we estimate that at least $\sim$50–80% of the IRAC 8 μm filter band emission is produced by PAHs. As in other high UV-flux PDRs, the PAH emission delineates the atomic zone edge of the Orion Bar (see e.g. Berné et al. 2009; Joblin et al. 2010, for Mon R2 and NGC 7023, respectively). The molecular dissociation front traced by the vibrationally excited H_2 $v = 1 \to 0$ S(1) emission (H_2^*; black contours in Fig. 10; Walmsley et al. 2000) and also the [C II] 158 μm intensity maxima (Bernard-Salas et al. 2012; Ossenkopf et al. 2013) peak slightly deeper in the cloud than the PAHs.

The increased sensitivity and broader frequency coverage of (sub)mm receivers led to the opportunity to map the faint emission of trace chemical species. Figure 10 also shows the integrated line intensity maps of C_2H ($N = 1 \to 0$ and $3 \to 2$ lines at 87.3 GHz and 262.0 GHz, respectively) and c-C_3H_2 ($J_{K_a,K_c} = 2_{1,2} \to 1_{0,1}$ and $6_{1,6} \to 5_{0,5}$ lines at 85.3 GHz and 217.8 GHz, respectively) in white contours. The emission from the Orion Bar can be distinguished more easily from the extended OMC1 cloud component by the emission LSR velocity. While OMC1 is brighter in the 8–10 km s^{-1} velocity range, the Orion Bar emits predominantly in the 10–12 km s^{-1} range. The C_2H and c-C_3H_2 emission contours shown in Fig. 10 are integrated in this interval. Both species show a similar distribution delineating the bar structure of the PDR. However, the morphology of the emission depends on the involved transition energy level, with the more excited lines (those at 1 mm) peaking closer to the cloud edge. The elongated spatial distribution of the hydrocarbon emission is parallel to the H_2^* emission, with the 1 mm C_2H and c-C_3H_2 lines peaking close to the H_2^* intensity peaks. Despite the similar distance, the spatial stratification [PAH]/[C^+-H_2^*-hydrocarbons] is more clearly seen towards the Orion Bar than towards low UV-flux PDRs seen almost edge on (e.g. the Horsehead; Pety et al. 2005). We note that van der Wiel et al. (2009) had previously mapped the C_2H $N = 4 \to 3$ lines with the JCMT telescope and shown that they peak closer to the dissociation front than other (higher energy) lines from SO or H_2CO. Hence, this is a true chemical stratification effect that confirms that C_2H is efficiently produced at the edge of the PDR. The lower excitation lines of both C_2H and c-C_3H_2 (those at 3 mm), however, peak deeper inside the cloud where the gas is less exposed to the FUV-radiation field and clumps/condensations of dense material and large $N(H_2)$ column densities are known to exist (Lis & Schilke 2003).
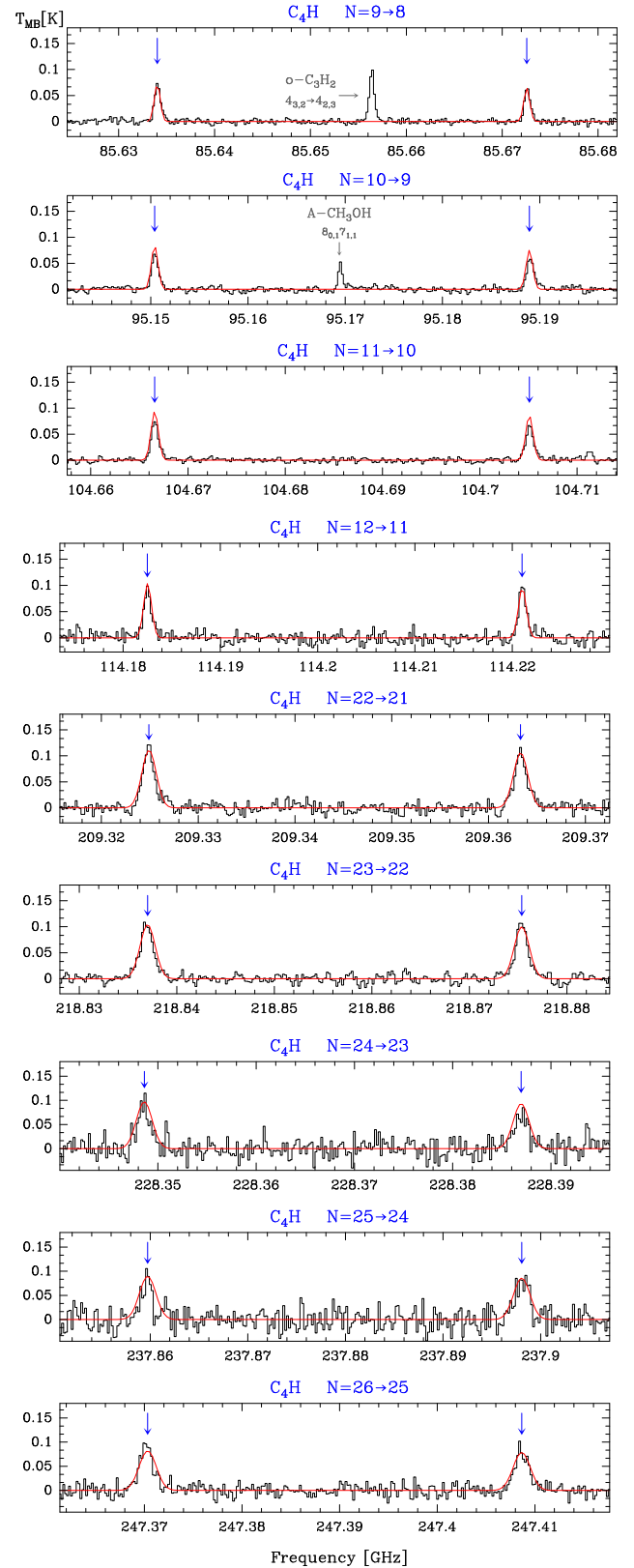
**Fig. 9.** C_4H spectra observed in the Orion Bar (black histogram spectra). A LTE model is overlaid in red (see Sect. 5.2). Line doublets are indicated by the blue arrows. The other spectral features appearing in the selected windows are labelled with their corresponding identification.

5. Analysis

The large number of lines of the different species detected in the 3, 2, 1, and 0.8 mm surveys allows us to carry out a
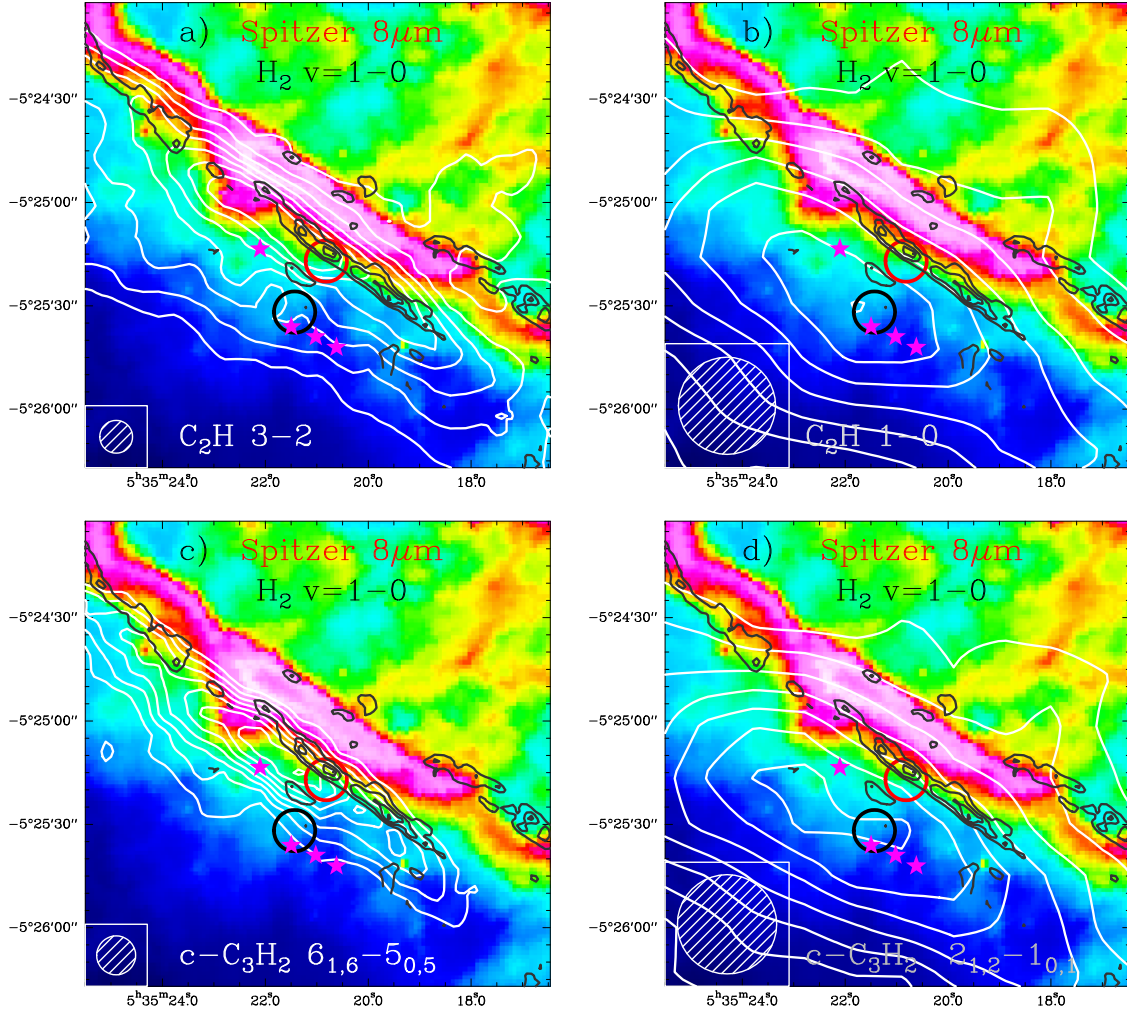
Fig. 10. C_2H and c-C_3H_2 integrated line-intensity maps (white contours) of the Orion Bar. *Upper panels*: C_2H **a)** $N = 3 \rightarrow 2$ at 262.0 GHz; and **b)** $N = 1 \rightarrow 0$ at 87.3 GHz. *Lower panels*: c-C_3H_2 **c)** $6_{1,6} \rightarrow 5_{0,5}$ at 217.8 GHz; and **d)** $2_{1,2} \rightarrow 1_{0,1}$ at 85.3 GHz. The *Spitzer* 8 μm extended emission due to PAHs and very small grains is in colour scale. Black contours are the H_2^* $v = 1 \rightarrow 0$ emission (Walmsley et al. 2000). Stars represent the positions of denser clumps/condensations detected in $H^{13}CN$ $J = 1 \rightarrow 0$ (Lis & Schilke 2003). The IRAM 30 m beams at 1 mm and 3 mm are plotted in the bottom left corner (white striped circle). The target position of the Orion Bar survey, close to the dissociation front, and the molecular peak position beyond the PDR (clump No. 10 of Lis & Schilke 2003; see text for discussion) are indicated with a red and a black circle, respectively. The emission of all lines from C_2H and c-C_3H_2 is integrated in the 10–12 km s^{-1} velocity interval in which the Orion Bar shows prominent emission.

detailed analysis of their excitation to (i) constrain rotational temperatures and column densities accurately; and (ii) investigate the physical conditions for those species with known collisional rates. We first extracted the line profile parameters by Gaussian fits. Second, we calculated rotational temperatures and column densities by constructing rotational population diagrams for each detected molecule. Third, we used the MADEX code (Cernicharo 2012, and references given in Sect. 3) to take into account radiative transfer effects in the observed lines. MADEX computes the intensities of molecular lines in the non-LTE LVG approximation for those molecules whose collisional rates are available, or assuming LTE conditions (to be more precise, a single rotational temperature and a Boltzmann distribution for the rotational levels population) if these rates are not available. See Appendix A for a short comparison with other publicly available code.

5.1. Line parameter fitting procedure

Gaussian profiles were fitted to all detected lines using CLASS. The derived parameters are shown in Appendix B. When two or more transitions overlap, the total profile was fitted. The overlapped transitions are marked with connecting symbols in the tables. Figure 11 shows the observed line widths of C_2H, l-C_3H^+, l-C_3H c-C_3H_2, and C_4H versus the energy of the upper level of the transition. Comparing the detected lines, we conclude that (i) the hydrocarbon lines have a pure Gaussian emission profile; (ii) the average LSR velocity towards the Bar for these lines is 10.7 ± 0.3 km s^{-1}; (iii) the intrinsic line widths are typically ~2 km s^{-1}; (iv) the broadest lines correspond to the lowest energy transitions at 3 mm observed with a larger beam size (~30″–20″ at 3 mm). This is likely an indication of molecular emission in the extended OMC1 cloud that contributes to broadening the observed lines. The c-C_3H and l-C_3H isomers, however, show narrower line profiles suggesting that they arise from specific (less turbulent and more compact) regions in the Bar.

5.2. Rotational population diagrams

For each molecule, we computed a representative rotational temperature (T_{rot}) and a beam-averaged column density (N) by
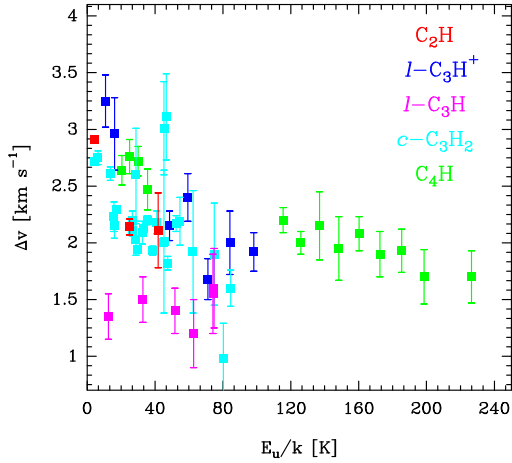
Fig. 11. Hydrocarbon line widths versus transition upper level energy for C_2H, l-C_3H^+, l-C_3H, c-C_3H_2, and C_4H lines.

constructing a rotational diagram, assuming optically thin emission filling the beam and a single rotational temperature for all energy levels (Goldsmith & Langer 1999). The standard relation for the rotational diagram analysis is

$$\ln \frac{N_u}{g_u} = \ln N - \ln Q_{T_{rot}} - \frac{E_u}{kT_{rot}}, \tag{1}$$

with N_u/g_u given by

$$\frac{N_u}{g_u} = \frac{8\pi k}{hc^3} \cdot \frac{\nu_{ul}^2}{A_{ul} g_u} \cdot \eta_{bf}^{-1} \cdot \int T_{MB} dv \quad [\text{cm}^{-2}], \tag{2}$$

where N_u is the column density of the upper level in the optically thin limit [cm^{-2}], N is the total column density [cm^{-2}], g_u is the statistical weight of the upper state of each level, $Q_{T_{rot}}$ is the partition function evaluated at a rotational temperature T_{rot}, E_u/k is the energy of the upper level of the transition [K], ν_{ul} is the frequency of the $u \rightarrow l$ transition [s^{-1}], $\int T_{MB} dv$ is the velocity-integrated line intensity corrected from beam efficiency [K km s^{-1}], and η_{bf} is the beam filling factor. Assuming that the emission source has a 2D Gaussian shape, η_{bf} is equal to $\eta_{bf} = \theta_S^2/(\theta_S^2 + \theta_B^2)$, with θ_B meaning the HPBW of the 30 m telescope in arcsec and θ_S the diameter of the Gaussian source in arcsec. The values for ν_{ul}, A_{ul}, g_u, $\int T_{MB} dv$, and E_u/k for each molecular transition are given in Appendix B and were taken from the MADEX spectral catalogue.

The condition for optically thin emission is correct in our case because we do not expect excessively large hydrocarbon column densities towards the Orion Bar dissociation front. The most abundant hydrocarbon in the Orion Bar is C_2H and, as previously mentioned in Sect. 3.1.1, the relative intensities of the hyperfine components show that lines are optically thin. The rotational diagrams were built considering two limiting cases: (i) that the detected emission is extended, with $\eta_{bf} = 1$; and (ii) that the emission is semi-extended, assuming that $\theta_S = 9''$ (the typical beam at ~1 mm). We considered only lines not blended with other transitions. Ortho and para forms of linear and cyclic C_3H_2 are treated as different species because radiative transitions between both states are forbidden. In order to build the rotational diagram for molecules with hyperfine structure, each hyperfine line component was described without splits, only with a single rotational number N. For this purpose, the integrated intensity, W, level degeneracy, g, and line strength, S,

of each transition was calculated as the sum of all allowed hyperfine components of each $N + 1 \rightarrow N$ transition. The characteristic frequency, ν, was determined using the weighted average with the relative strength of each line as weight, and the Einstein coefficient, A, was calculated using the usual relation:

$$A = \frac{64\pi^4}{3hc^3} \cdot \frac{\nu^3 S}{g} \cdot \mu^2 \quad [\text{s}^{-1}]. \tag{3}$$

The resulting rotational diagrams are shown in Fig. 12. Rotational temperatures and column densities obtained by linear least squares fits for extended and semi-extended emission are listed in Table 4. The uncertainties shown in Table 4 indicate the uncertainty obtained in the least squares fit of the rotational diagram. The uncertainty obtained in the determination of the line parameters with the Gaussian fitting programme are included in the uncertainty bars at each point of the rotational diagram. Table 4 also shows the estimated abundances with respect to hydrogen nuclei using a line-of-sight $N(H_2) \simeq 3 \times 10^{22}$ cm^{-2} column density towards the line survey position. This beam-averaged H_2 column density was derived from our observations of the $C^{18}O$ lines ($J = 1 \rightarrow 0$, $2 \rightarrow 1$ and $3 \rightarrow 2$ transitions) by constructing a rotational diagram, assuming $^{16}O/^{18}O \approx 500$ (Wilson & Rood 1994) and a CO/H_2 abundance of ~10^{-4} (lower than the canonical value due to dissociation). The resulting H_2 column density is in good agreement with previous estimations of $N(H_2)$ close to the dissociation front (see e.g. Hogerheijde et al. 1995). In addition, a $N(H) \simeq 3 \times 10^{21}$ cm^{-2} column density of hydrogen atoms has been inferred from H I observations towards the Orion Bar (van der Werf et al. 2013). Hence, a small fraction of free H atoms exist.

Rotational temperatures and column densities derived from the rotational diagram of each molecule (assuming extended source) were used as input parameters to model the line profiles using the MADEX radiative transfer model under LTE conditions. Figures 4–6, 8, and 9 show the observational spectra (black histograms) and the modelled spectra (red lines) of l-C_3H^+, l-C_3H, c-C_3H, l-H_2C_3, and C_4H, respectively. The obtained fits using LTE models agree with the observations. The computed optical depths at line centre are $\tau < 0.1$ for C_2H, o/p-C_3H_2, and C_3H^+ lines, and $\tau < 0.01$ for the rest of the hydrocarbons. Hence, there are no noticeable line opacity effects in the calculated rotational temperatures and column densities.

For those species for which only one rotational line was detected, we estimated their column densities using as an input parameter the rotational temperatures derived from another molecule with similar structure and rotational constants. In particular, the ^{13}CCH and $C^{13}CH$ column densities were estimated assuming that the rotational temperature is similar to that obtained for C_2H. Figure 3 shows the observational (black histogram) and modelled (red lines) spectra of ^{13}CCH and $C^{13}CH$.

Rotational temperatures range from 17 to 77 K, and column densities from 10^{11} to 10^{14} cm^{-2}. The C_2H radical is by far the most abundant of the detected hydrocarbons, followed by C_4H and c-$(o+p)$-C_3H_2. The linear three-carbon species (l-C_3H and l-H_2C_3) are less abundant than their cyclic isomers. The ortho-to-para ratio obtained from the c-C_3H_2 column density is 2.8 ± 0.6, similar to the expected value at high temperature. The [$C^{13}CH$]/[^{13}CCH] ratio is 1.4 ± 0.1 (3σ). Comparing the rotational temperatures, we conclude that (i) almost all species have $T_{rot} < 30$ K, but l-C_3H^+ and C_4H are rotationally hotter than the other species, reaching $T_{rot} = 46$ K and 77 K, respectively; (ii) although cyclic forms have lower dipole moments, the
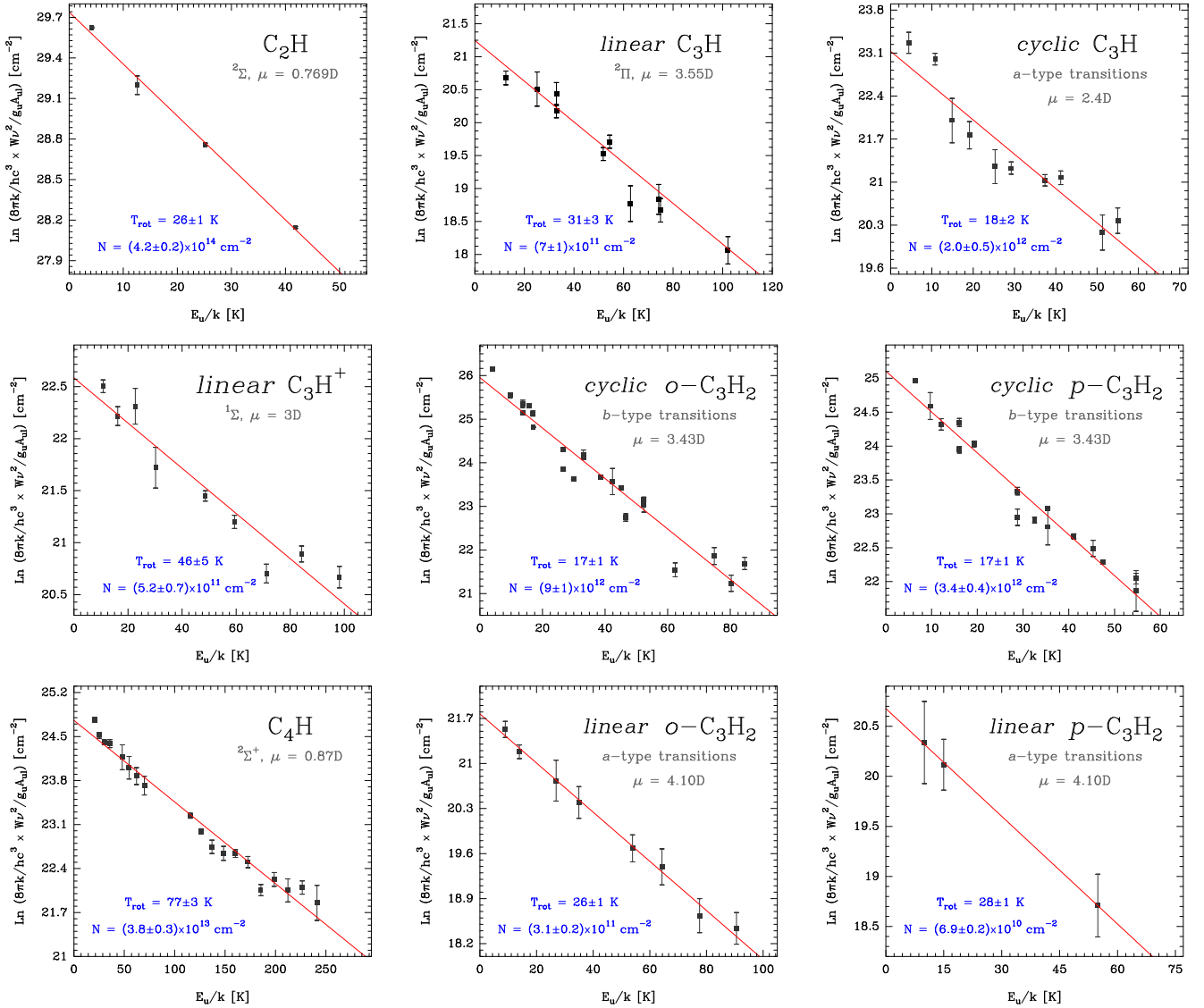
Fig. 12. Rotational diagrams of the detected hydrocarbon molecules in the Orion Bar PDR. Fitted values of the rotational temperature, $T_{\rm rot}$, column density, N, and their respective uncertainties are also indicated for each molecule.

rotational temperatures of the cyclic species (c-C_3H_2 and c-C_3H) are smaller than their respective linear isomers (l-H_2C_3 and l-C_3H); (iii) we obtain similar rotational temperatures for the ortho and para forms of the same molecule; (iv) C_2H and C_4H have similar dipole moments and rotational spectroscopy, but show quite different rotational temperatures (26 K and 77 K, respectively). This low temperature for C_2H means that in the millimetre domain we detect the warm C_2H (containing most of the column density), but not the hotter C_2H recently detected by *Herschel*/HIFI (higher energy transitions from $N = 6 \rightarrow 5$ to $10 \rightarrow 9$; see Nagy et al., in prep.). We estimate that this hotter C_2H only contributes to ~5% of the total C_2H column. The rotational temperature deduced for C_4H will be discussed in Sect. 7.1.

5.3. Spatial variation of the C_2H and c-C_3H_2 abundance

In order to investigate the C_2H and c-C_3H_2 column density and abundance variations along the Orion Bar, we reprojected the 3 mm and 1 mm IRAM 30 m maps to a common grid. We selected two representative positions, one towards the line survey position at the PDR dissociation front (near the C_2H $N = 3 \rightarrow 2$ line emission peak) and the other deeper inside the cloud where the C_2H $N = 1 \rightarrow 0$ line peaks, that we call the molecular peak. This latter position coincides with the dense clump/condensation No. 10 detected by Lis & Schilke (2003) in $H^{13}CN$ $J = 1 \rightarrow 0$ emission. We extracted the C_2H and c-o-C_3H_2 column densities towards these two positions by constructing reduced rotational diagrams with the line intensities extracted from the maps. Figure 13 shows the C_2H ($N = 1 \rightarrow 0$ and $3 \rightarrow 2$) and c-o-C_3H_2 ($J_{K_a,K_c} = 2_{1,2} \rightarrow 1_{0,1}$ and $5_{1,4} \rightarrow 4_{2,3}$) spectra towards the two selected positions. The dark blue spectrum shows the emission in the PDR dissociation front and the light blue spectrum shows the emission deeper inside the cloud. Table 5 shows the C_2H and c-o-C_3H_2 rotational temperatures and column densities towards the two positions. Close to the dissociation front, where the gas is hotter, the inferred rotational temperatures are higher. Despite the similar C_2H and c-o-C_3H_2 column densities towards both positions, the N_H column density towards the cloud edge is necessarily smaller than towards clump/condensation No. 10. This is readily seen in $C^{18}O$ line maps that show the brightest emission towards the molecular peak position deeper inside the

Table 4. Rotational temperatures (T_{rot}), column densities ($N(X)$), and abundances with respect to hydrogen nuclei inferred in the Orion Bar PDR.

	Extended source		Semi-extended source		Abundance	Notes
	T_{rot} [K]	$N(X)$ [cm^{-2}]	T_{rot} [K]	$N(X)$ [cm^{-2}]		
C_2H	26 ± 1	$(4.2 \pm 0.2) \times 10^{+14}$	12 ± 3	$(1.7 \pm 0.7) \times 10^{+15}$	$(0.7\text{--}2.7) \times 10^{-8}$	*a*
^{13}CCH	26	$3.0 \times 10^{+12}$	12	$4.6 \times 10^{+12}$	$(4.8\text{--}7.3) \times 10^{-11}$	*b*
$C^{13}CH$	26	$4.2 \times 10^{+12}$	12	$6.5 \times 10^{+12}$	$(0.7\text{--}1.0) \times 10^{-10}$	*b*
c-C_3H	18 ± 2	$(2.0 \pm 0.5) \times 10^{+12}$	11 ± 1	$(9.9 \pm 3.5) \times 10^{+12}$	$(0.3\text{--}1.6) \times 10^{-10}$	*a*
l-C_3H	31 ± 3	$(7.0 \pm 1.1) \times 10^{+11}$	20 ± 2	$(3.4 \pm 0.9) \times 10^{+12}$	$(1.1\text{--}5.4) \times 10^{-11}$	*a*
l-C_3H^+	46 ± 5	$(5.2 \pm 0.7) \times 10^{+11}$	25 ± 3	$(2.5 \pm 0.6) \times 10^{+12}$	$(0.8\text{--}4.0) \times 10^{-11}$	*a*
c-o-C_3H_2	17 ± 1	$(9.4 \pm 1.3) \times 10^{+12}$	15 ± 1	$(4.1 \pm 1.3) \times 10^{+13}$	$(1.5\text{--}6.5) \times 10^{-10}$	*a*
c-p-C_3H_2	17 ± 1	$(3.4 \pm 0.4) \times 10^{+12}$	11 ± 1	$(1.8 \pm 0.5) \times 10^{+13}$	$(0.5\text{--}2.9) \times 10^{-10}$	*a*
[c-$(o+p)$-C_3H_2]	–	$(1.3 \pm 0.2) \times 10^{+13}$	–	$(5.9 \pm 0.9) \times 10^{+13}$	$(2.1\text{--}9.4) \times 10^{-10}$	*c*
l-o-C_3H_2	26 ± 1	$(3.1 \pm 0.2) \times 10^{+11}$	17 ± 1	$(1.9 \pm 0.4) \times 10^{+12}$	$(0.5\text{--}3.0) \times 10^{-11}$	*a*
l-p-C_3H_2	28 ± 1	$(6.9 \pm 0.2) \times 10^{+10}$	15 ± 1	$(4.0 \pm 0.8) \times 10^{+11}$	$(1.1\text{--}6.4) \times 10^{-12}$	*a*
[l-$(o+p)$-C_3H_2]	–	$(3.8 \pm 0.2) \times 10^{+11}$	–	$(2.3 \pm 0.5) \times 10^{+12}$	$(0.6\text{--}3.7) \times 10^{-11}$	*c*
C_4H	77 ± 3	$(3.8 \pm 0.3) \times 10^{+13}$	49 ± 3	$(2.0 \pm 0.3) \times 10^{+14}$	$(0.6\text{--}3.2) \times 10^{-9}$	*a*

Notes. [a] Rotational temperatures and column densities from rotational diagram analysis. [b] Column densities derived from a LTE model assuming $T_{rot} = 26$ K for extended source and $T_{rot} = 12$ K for semi-extended source. [c] Total column densities calculated as the sum of the ortho and para species. The abundance of each species with respect to H nuclei is given by $\frac{N(X)}{N_H} = \frac{N(X)}{N(H)+2N(H_2)}$, with $N(H_2) \simeq 3 \times 10^{+22}$ cm^{-2} (see Sect. 5.2) and $N(H) \simeq 3 \times 10^{+21}$ cm^{-2} (van der Werf et al. 2013).
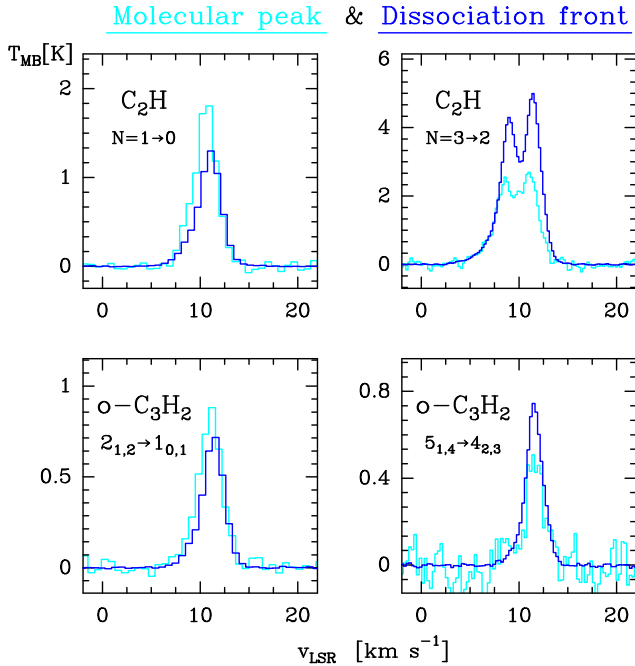
Fig. 13. C_2H (*upper panels*) and c-C_3H_2 (*lower panels*) spectra towards two different positions in the Orion Bar: one in the dissociation front where we have carried out a line survey (dark blue spectrum), and the other towards clump No. 10 of Lis & Schilke (2003) that we call the molecular peak (light blue spectrum). The spectra towards the molecular peak were extracted from the 1 mm and 3 mm reprojected maps.

Bar and a faint emission level towards the dissociation front (e.g. van der Wiel et al. 2009; Cuadrado et al., in prep.). The variation of the C_2H and c-o-C_3H_2 abundances can then be estimated using $N_H \simeq 3.3 \times 10^{22}$ cm^{-2} towards the dissociation front (see Sect. 5.2) and $N_H \simeq 2.5 \times 10^{23}$ cm^{-2} towards clump No. 10 (the median column density inferred by Lis & Schilke 2003

Table 5. Rotational temperatures (T_{rot}), column densities ($N(X)$), and abundances of C_2H and c-o-C_3H_2 with respect to hydrogen nuclei inferred in the dissociation front (DF) and in the molecular peak (MP).

		T_{rot} [K]	$N(X)$ [cm^{-2}]	Abundance*a*
C_2H	DF	26 ± 1	$(4.2 \pm 0.2) \times 10^{+14}$	$\sim 6.7 \times 10^{-9}$
	MP	13 ± 2	$(3.7 \pm 0.6) \times 10^{+14}$	$\sim 7.4 \times 10^{-10}$
c-o-C_3H_2	DF	17 ± 1	$(9.4 \pm 1.3) \times 10^{+12}$	$\sim 1.5 \times 10^{-10}$
	MP	11 ± 2	$(1.2 \pm 0.2) \times 10^{+13}$	$\sim 2.4 \times 10^{-11}$

Notes. [a] With respect to H nuclei, using $N_H \simeq 3.3 \times 10^{+22}$ cm^{-2} (see Sect. 5.2) towards the dissociation front (DF) and $N_H \simeq 2.5 \times 10^{23}$ cm^{-2} (Lis & Schilke 2003) towards the molecular peak (MP).

towards the dense H^{13}CN clumps). This factor of ~ 10 difference is consistent with the expected increase of line-of-sight material with distance from the PDR edge to the density peak (d), and estimated as d^2 from detailed dust radiative transfer models (Arab et al. 2012). Therefore, the C_2H abundance with respect to hydrogen nuclei is higher towards the PDR edge ($\sim 10^{-8}$) than deeper inside the cloud ($\sim 10^{-9}$). c-C_3H_2 shows a similar trend and therefore both hydrocarbons show enhanced abundances towards the UV-illuminated edge of the cloud, but they are also moderately abundant in the more shielded cloud interior. Although higher angular resolution observations will be needed to accurately constrain the abundance gradients in more detail, we note that the [C_2H]/[c-C_3H_2] column density ratio decreases from the illuminated cloud edge to the cloud interior.

5.4. Non-LTE excitation analysis

In order to derive the beam-averaged physical conditions in the observed region we studied the non-LTE excitation of
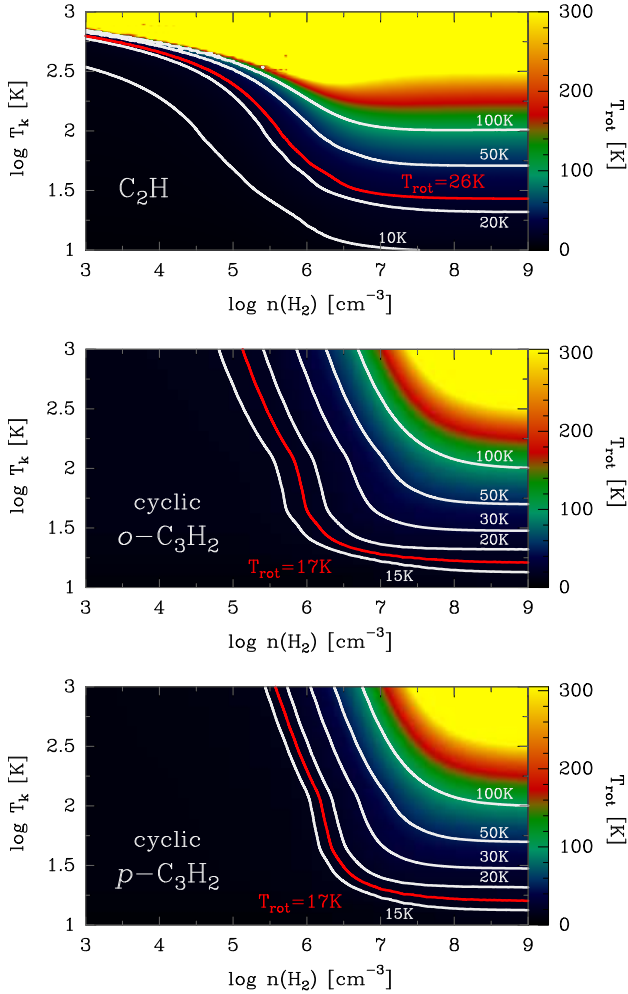
Fig. 14. Grid of C_2H, o-C_3H_2, and p-C_3H_2 LVG models for different gas temperatures and densities. White contour levels represent iso-rotational temperatures. The red curves show the rotational temperature derived from our observations towards the survey position.

the C_2H and c-C_3H_2 molecules for which accurate collisional rates exist. We used C_2H-He collisional rates from Spielfiedel et al. (2012) and C_3H_2-He from Chandra & Kegel (2000) for C_2H and c-C_3H_2, respectively. A large grid of LVG models for a broad range of column densities, H_2 densities $(n(H_2) = 10^{3-9}$ cm$^{-3})$, and kinetic temperatures $(T_k = 10-1000$ K) values were run to obtain synthetic line intensities for C_2H and cyclic o/p-C_3H_2. The best fit models have column densities within a factor of 2 of the inferred value from the rotational diagram analysis (see Sect. 5.2). Hence, we used constant beam-averaged column densities for further analysis $(N(C_2H) = 4.2 \times 10^{+14}$ cm^{-2}, $N(c$-o-$C_3H_2) = 9.4 \times 10^{+12}$ cm^{-2}, and $N(c$-p-$C_3H_2) = 3.4 \times 10^{+12}$ cm$^{-2})$. The C_2H models were fitted in the $N_{up} = 1$ to 5 transition range, and c-C_3H_2 models were fitted within the $J_{up} = 2-8$ range. We used $\Delta v = 2$ km s^{-1} line widths. Figure 14 shows the LVG model results in the form of iso-T_{rot} contours. Each T_{rot} was calculated by building rotational diagrams with the synthetic line intensities obtained from each model. Figure 14 shows that the T_{rot} inferred from our survey data (the red contours) can be obtained for different combinations of gas density $(n(H_2))$ and temperature (T_k).

In order to constrain accurately the range of physical conditions that reproduce the observed intensities towards the dissociation front, we compared the C_2H detected lines to the synthetic line intensities obtained in the grid of LVG models. We only used

the C_2H $N = 3 \rightarrow 2$ and $4 \rightarrow 3$ hyperfine components in the analysis as they were observed with higher angular and spectral resolution. In addition, the extended emission from OMC1 likely contributes to the observed 3 mm lines, both in amplitude and in line-broadening (see Sect. 5.1). Following Neufeld et al. (2014), the best fit model was obtained by finding the minimum root mean square (rms) value of $\log_{10}(I_{obs}/I_{mod})$. This is defined as

$$\text{rms} = \sqrt{\frac{1}{n} \sum_{i=1}^{n} \left(\log_{10} \frac{I_{obs}^i}{I_{mod}^i} \right)^2},\qquad(4)$$

where n is the number of observed lines, I_{obs}^i is the observed line intensity calculated from Gaussian fits to the lines listed in Table B.1, and I_{mod}^i is the model line intensity using MADEX.

Figure 15 (left) represents the rms$_{min}$/rms ratio as a function of T_k and $n(H_2)$ for a grid of excitation models trying to fit the C_2H $N = 3 \rightarrow 2$ and $4 \rightarrow 3$ lines towards the PDR position. The set of physical conditions that best fit the lines lie within $T_k = 150-250$ K, $n(H_2) = (0.7-1.7) \times 10^5$ cm^{-3}. Figure 15 (right) also shows the best fit C_2H model $(T_k \simeq 150$ K, $n(H_2) \simeq 1.5 \times 10^5$ cm$^{-3})$ overlaid over the observed lines. The computed opacities at line centre are $\tau < 0.1$. We note that the ^{12}CO line intensity peaks $(T_{MB}^p$; in main beam temperature) towards the line survey position goes from ~115 K to ~160 K (for the $J = 1 \rightarrow 0$ and $3 \rightarrow 2$ lines, respectively). Since low-J ^{12}CO lines are optically thick $(W[^{12}CO\ 3 \rightarrow 2]/W[^{13}CO\ 3 \rightarrow 2] \simeq 5$, much lower than the $^{12}C/^{13}C$ isotopic ratio of 60), their intensity peak provides a good lower limit to the gas temperature $(T_{MB}^p \lesssim T_{ex} \lesssim T_k)$. Therefore, the temperatures inferred from C_2H and ^{12}CO are in good agreement and consistent with $T_k \simeq 150$ K. Nevertheless, the gas temperature and density in a PDR are expected to vary at spatial scales that cannot be resolved with our single-dish observations. Therefore, these values should be considered as the averaged conditions towards the Orion Bar dissociation front within a ~30″–10″ beam.

In the case of c-(o/p)-C_3H_2, as shown in the plot of iso-T_{rot} (Fig. 14), the excitation of the millimetre lines provides a lower limit to the H_2 density of a few 10^5 cm^{-3}. The statistical analysis to obtain the best fit of the c-(o/p)-C_3H_2 lines was not conclusive because several sets of these two parameters fit the lines. However, for the physical conditions expected in the Orion Bar, the c-C_3H_2 lines do not exactly fit with the same physical conditions as C_2H. Slightly denser gas and a lower temperature are needed to obtain a satisfactory fit of c-(o/p)-C_3H_2 lines $(T_k \simeq 100$ K and $n(H_2) \simeq 4.0 \times 10^5$ cm^{-3}; see Fig. 7). As we see later, this is roughly consistent with our chemical models (Sect. 6) which predict that the c-C_3H_2 abundance peaks slightly deeper inside the cloud than C_2H.

5.5. Undetected hydrocarbons

The broadband coverage of the Orion Bar survey allowed us to obtain upper limits for other chemically interesting carbon-bearing molecules that have not been detected in the PDR: longer carbon chains, anions, and deuterated isotopologues. In particular, we searched for C_2D, C_5H, C_6H, C_2H^-, C_4H^-, C_6H^-, H_2C_4, and $C_2H_3^+$. First, we estimated 3σ line intensities using the relation (e.g. Coutens et al. 2012)

$$\int T_{MB} dv = 3\sigma \sqrt{2\, \delta v\, \Delta v} \qquad [\text{K km s}^{-1}],\qquad(5)$$

where σ is the rms of the observations [K], δv is the velocity-spectral resolution [km s^{-1}], and Δv is the assumed line widths
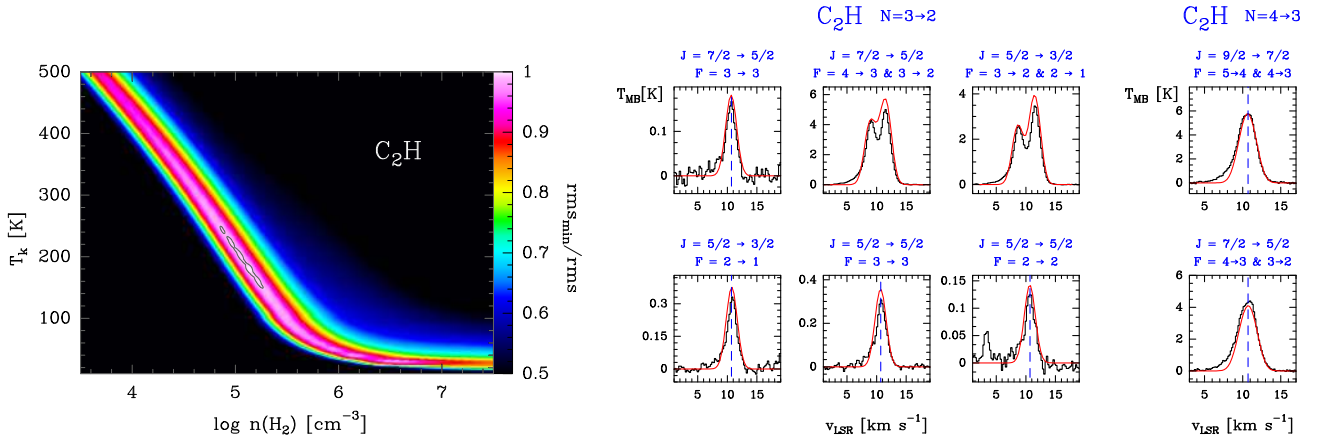
Fig. 15. *Left panel*: rms$_{\rm min}$/rms ratio as a funtion of $T_{\rm k}$ and $n(H_2)$ for a grid of LVG models. The best fit models were obtained with $T_{\rm k}$ = 150–250 K and $n(H_2)$ = (0.7–1.7) × 10^5 cm^{-3}. *Right panel*: observed C$_2$H N = 3 → 2 and 4 → 3 spectra. The best fit LVG model ($T_{\rm k}$ ≃ 150 K, $n(H_2)$ ≃ 1.5 × 10^5 cm^{-3}, and $N(C_2H)$ = 4.2 × 10^{14} cm^{-2}) is shown overlaid in red.

Table 6. Upper limits for undetected hydrocarbons.

| Molecule	$N(X)$ [cm^{-2}]	Abundance[a]
p-C$_2$H$_3^+$	(1.8–2.0) × 10^{+12}	(2.9–3.2) × 10^{-11}
C$_2$D	(5.0–9.0) × 10^{+11}	(0.8–1.4) × 10^{-11}
(o+p)-H$_2$C$_4$	(2.5–2.8) × 10^{+11}	(4.0–4.4) × 10^{-12}
C$_6$H	(2.0–4.0) × 10^{+11}	(3.2–6.4) × 10^{-12}
C$_5$H	(1.5–2.0) × 10^{+11}	(2.4–3.2) × 10^{-12}
C$_6$H$^-$	(0.7–1.5) × 10^{+11}	(1.1–2.4) × 10^{-12}
C$_2$H$^-$	(2.0–3.0) × 10^{+10}	(3.2–4.8) × 10^{-13}
C$_4$H$^-$	(1.5–2.0) × 10^{+10}	(2.4–3.2) × 10^{-13}

Notes. [a] The abundance of each species with respect to H nuclei is given by $\frac{N(X)}{N_H} = \frac{N(X)}{N(H)+2N(H_2)}$, for $N(H_2)$ = 3 × 10^{+22} cm^{-2} (see Sect. 5.2) and $N(H)$ = 3 × 10^{+21} cm^{-2} (van der Werf et al. 2013).

(~2 km s^{-1}). Second, we used MADEX to create LTE models to simulate the emission of different rotational lines at different frequencies of the same species and to constrain their column densities. The column densities and abundances 3σ upper limits for $T_{\rm rot}$ = 20–30 K are listed in Table 6.

Despite some controversy about their presence in PDRs (see e.g. Fortenberry et al. 2013), hydrocarbon anions are not detected at the sensitivity level of our line survey. We provide the following abundance ratio limits: [C$_2$H$^-$]/[C$_2$H] < 0.007% and [C$_4$H$^-$]/[C$_4$H] < 0.05%. They agree with previous unsuccessful anion searches in other interstellar environments (e.g. Agúndez et al. 2008b).

6. PDR models of the Orion Bar

To investigate whether the inferred hydrocarbon column densities and spatial distribution agree with our current understanding of their gas-phase chemical formation, we have used an updated version of the Meudon code for photochemical studies (Le Petit et al. 2006; Le Bourlot et al. 2012). This 1D PDR model solves the FUV radiative transfer in an absorbing and diffusing medium of gas and dust (Goicoechea & Le Bourlot 2007). This allows the explicit computation of the FUV radiation field (continuum+lines) and, therefore, the explicit integration of self-consistent photoionisation and photodissociation rates as
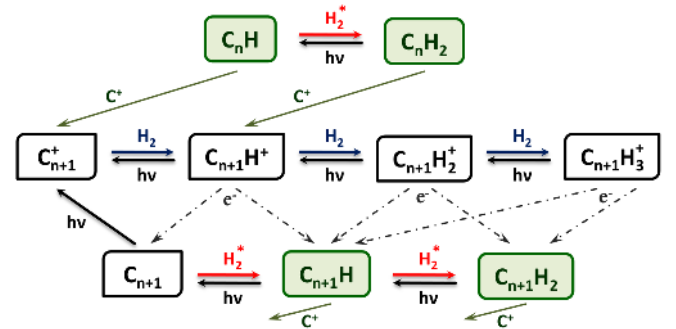
Fig. 16. Scheme with the main gas-phase formation and destruction reactions of small hydrocarbons predicted by our model of the Orion Bar PDR at A_V ≃ 1.5 (close to their abundance peak). Reactions with activation energy barriers are indicated with red arrows. The blue arrows are barrierless hydrogenation reactions.

a function of cloud depth. The model also solves the thermal balance (see Le Petit et al. 2006) and thus the thermal profile through the PDR. Once the attenuation of the FUV radiation field and the temperature profile have been determined, steady-state chemical abundances are computed for a given chemical reaction network.

Our network contains ~130 species and ~2800 gas-phase reactions. It includes the formation of carbon bearing molecules up to four carbon atoms. In our models we adopt a FUV radiation field χ = 2 × 10^4 times the mean interstellar radiation field (ISRF) in Draine units (e.g. Marconi et al. 1998). When available, we used photodissociation rates given by van Dishoeck & Black (1988) and van Dishoeck et al. (2006; multiplied by χ), which are explicitly calculated for the Draine interstellar radiation field (ISRF). State-to-state reactions of vibrationally excited H$_2$ with C$^+$, O, or OH are explicitly treated (see Agúndez et al. 2010). We have further upgraded the carbon-bearing species network and used the most recent branching ratios for ion-molecule, neutral-neutral, dissociative recombination, and charge exchange reactions for carbon chains and hydrocarbon species described in Chabot et al. (2013). Reactions of hydrocarbon radicals with H and H$_2$ are also included in the model (see e.g. Cernicharo 2004; Agúndez et al. 2008a). Figure 16 shows the dominant gas-phase formation and destruction routes of hydrocarbons predicted by our PDR models of the Orion Bar close to their abundance peak (at A_V ≃ 1.5, see below).
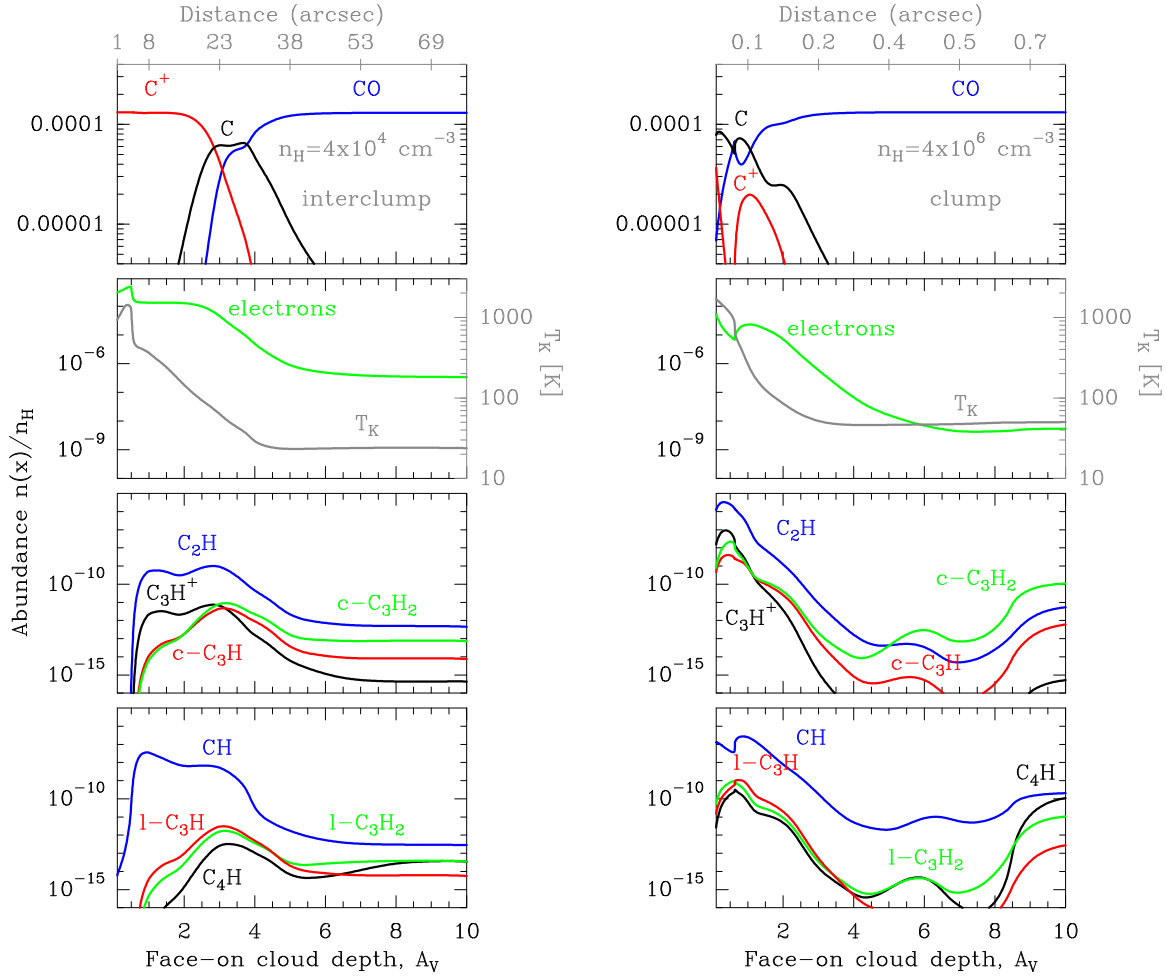
Fig. 17. Constant density, photochemical models as a function of cloud visual extinction (A_V) for $\chi = 2 \times 10^4$. *Left:* $n_{\rm H} = 4 \times 10^4$ cm^{-3} characteristic of a moderate density interclump medium; *right:* $n_{\rm H} = 4 \times 10^6$ cm^{-3} characteristic of higher density clumps. We note the different spatial scales, thermal profile, and molecular abundance and ionisation fraction gradients implied by the two models.

We also included the freeze-out of molecular and atomic species at different cloud depths. In our models ice mantles can desorb thermally and non-thermally (FUV-induced), but we do not contemplate grain surface chemistry. Given the high FUV radiation field and thus grain temperatures in the Orion Bar PDR ($T_d \approx 50–70$ K; Arab et al. 2012), the less volatile species (e.g. H_2O) start to be affected by freeze-out beyond the PDR surface ($A_V > 5$; e.g. Hollenbach et al. 2009). The adopted elemental abundances are those of Goicoechea et al. (2006). We adopted a cosmic-ray ionisation-rate ($\zeta_{\rm CR}$) of 10^{-16} s^{-1}, but we note that the total ionisation rate in the Orion Bar might be higher if one includes the X-ray ionisation effects produced by all X-ray stellar sources in the Trapezium cluster (e.g. Gupta et al. 2010).

In order to guide the interpretation of our observations, we ran two types of PDR models that have been proposed to reproduce the physical conditions in the Orion Bar: constant density and isobaric models. We first ran models with constant hydrogen nuclei density in which the thermal pressure decreases from the illuminated cloud edge to the cloud interior: an interclump medium with $n_{\rm H} = 4 \times 10^4$ cm^{-3} and a denser clump component with $n_{\rm H} = 4 \times 10^6$ cm^{-3} (see Andree-Labsch et al. 2014, for more complicated descriptions). Figure 17 shows the physical and chemical structure of the two models. The spatial scales of the chemical stratification seen in the PDR ($C^+/C/CO/...$) is only compatible with the presence of a moderate density interclump medium. The physical gradients in the denser clump

model occur in much smaller scales (that cannot be resolved with the IRAM 30 m) but produce enhanced columns of several species. Hence, an ensemble of low filling factor embedded clumps or dense gas structures may be responsible for some chemical signatures that we see averaged in our observations.

Alternatively, isobaric models (with $P \simeq 10^8$ K cm^{-3}), in which the gas density naturally increases from a few $\sim 10^4$ cm^{-3} in the cloud edge to a few $\sim 10^6$ cm^{-3} in the interior, have been recently invoked to explain the CH$^+$, OH$^+$ and high-J CO lines detected by *Herschel* (Nagy et al. 2013; van der Tak et al. 2013; Joblin et al., in prep.). A high thermal pressure model of this kind is shown in Fig. 18. In the following we restrict our discussion and model predictions for the observed hydrocarbon molecules.

6.1. Gas-phase formation of small hydrocarbons

Figure 18 shows model results for the $P \simeq 10^8$ K cm^{-3} isobaric model that we take as our reference model. For such a highly UV-illuminated PDR, the first step of the gas-phase carbon chemistry is the $H_2 + C^+ \rightarrow CH^+ + H$ reaction, which becomes faster than the $H_2 + C^+ \rightarrow CH_2^+$ + photon radiative association. The first reaction is endothermic by $E/k \approx 4300$ K. Hot gas (a few hundred K) and/or the presence of (FUV pumped) vibrationally excited H_2 are needed to overcome the reaction endothermicity (e.g. Black & van Dishoeck 1987; Agúndez et al. 2010). Such conditions apply to the edge of the Orion Bar, as
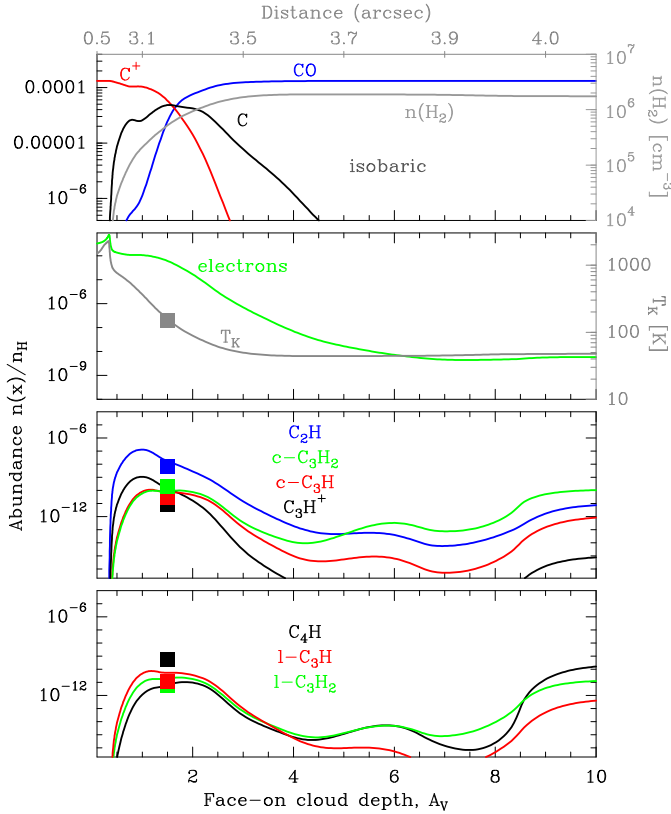
Fig. 18. Reference isobaric photochemical model for the Orion Bar with $P = 10^8$ K cm^{-3} and $\chi = 2 \times 10^4$. We note the increase of $n(H_2)$ as the gas temperatures decreases. The grey square shows the beam-averaged gas temperature estimated from our millimetre observations ($T_k \simeq 150$ K), which corresponds to $A_V \simeq 1.5$ in the model. The coloured squares show the beam-averaged abundances derived from the line survey.

demonstrated by the detection of rotationally excited CH$^+$ lines (see e.g. Habart et al. 2010; Nagy et al. 2013). The presence of significant amounts of CH$^+$ produces enhanced abundances of CH$_2^+$ and CH$_3^+$ ions by subsequent reactions with H$_2$ (barrierless reactions). These simple hydrocarbon ions recombine and form CH and CH$_2$. In fact, CH$^+$ and CH show extended line emission in the entire Orion region (Goicoechea et al., in prep.) whereas CH$^+$ has not been detected in low FUV-flux field PDRs like the Horsehead (Teyssier et al., in prep.). The coexistence of CH radicals and C$^+$ in the surface of the PDR allows the formation of C$_2^+$ through the ion-neutral reaction CH + C$^+ \rightarrow$ C$_2^+$ + H. This starts the chemistry of species containing two carbon atoms.

The C$_2^+$ ion reacts with H$_2$ to form C$_2$H$^+$, C$_2$H$_2^+$, and C$_2$H$_3^+$ by a series of successive barrierless hydrogenation reactions. Recombination of these ions with electrons form the abundant C$_2$ and C$_2$H neutrals. Figure 18 shows that most small hydrocarbons show a first abundance peak near the illuminated edge of the cloud where the predicted gas temperature sharply goes from ∼1000 K in the cloud surface, close to the ionisation front, to ∼150 K near the dissociation front at $A_V \approx 1.5$. Such elevated temperatures contribute to enhancing the abundance of C$_2$H through the C$_2$ + H$_2 \rightarrow$ C$_2$H + H reaction, which has an activation energy barrier of $E/k \approx 1500$ K (Pitts et al. 1982). For the physical conditions prevailing in the edge of Orion Bar, this neutral-neutral reaction dominates the gas-phase formation of abundant C$_2$H. For this reason, the gas-phase production of C$_2$H may be more efficient in dense and hot PDRs than in cool PDRs (we note the higher peak C$_2$H abundance in

the clump model compared to the interclump model in Fig. 17). Like CH$^+$ or CH, the highest C$_2$H abundances are predicted at the illuminated edge of the cloud. Reaction of C$_2$H with H$_2$ then forms acetylene, C$_2$H$_2$. This reaction is also favoured at high temperatures (Baulch 2005). Since C$^+$ is the most abundant carbon-bearing species in the PDR edge, further reactions of C$_2$H with C$^+$ produce C$_3^+$, that then reacts with H$_2$ to produce C$_3$H$^+$ (depending on the acetylene abundance, C$_2$H$_2$ + C$^+$ can also contribute to C$_3$H$^+$ formation). These are crucial intermediate precursors that form increasingly complex hydrocarbons. The chemistry of species containing three carbon atoms then proceeds. Reactions of C$_3$H$^+$ with H$_2$ produce the linear and cyclic forms of C$_3$H$_2^+$ and C$_3$H$_3^+$ isomers (e.g. Maluendes et al. 1993; McEwan et al. 1999). Dissociative recombination of these ions then produces the c-C$_3$H$_2$, l-H$_2$C$_3$, and l- and c-C$_3$H isomers (e.g. Fossé et al. 2001). The detection of l-C$_3$H$^+$ in the Horsehead (Pety et al. 2012) and Orion Bar, supports the above gas-phase routes for the synthesis of hydrocarbons containing several C atoms in UV-illuminated gas (i.e. with available C$^+$). We note that in the hydrocarbon abundance peak, their destruction is dominated by photodissociation (e.g. for C$_2$H and c-C$_3$H$_2$ producing C$_2$, C$_3$, and c-C$_3$H, respectively, see Fig. 16).

Although not all chemical rates and branching ratios involving hydrocarbons are known with precision, the Orion Bar is a good laboratory for testing this scheme (Fig. 16) because (i) large column densities of C$^+$ exist; (ii) the electron density is high enough to make recombination reactions efficient; and (iii) the gas temperature is high enough to activate the barriers of reactions involving neutral carbon-bearing molecules with H and H$_2$.

For the physical conditions prevailing in the Orion Bar, the gas temperature and ionisation fraction (the electron abundance or x_e) significantly drops at cloud depths larger than $A_V \approx 4$. At these depths, most of the carbon becomes locked in CO and not in C$^+$ or C. This modifies the hydrocarbon chemistry. Even deeper inside the cloud, molecules and atoms start to freeze-out so the exact abundances of small hydrocarbons in cloud interiors are more uncertain. In particular, they critically depend on x_e, which determines the abundance of hydrocarbon ion precursors (see also Fossé et al. 2001). The ionisation fraction in UV-shielded gas is set by the cosmic-ray ionisation-rate and by the poorly known gas-phase abundance of low ionisation metals like Fe that carry most of the positive charge (see Goicoechea et al. 2009, for the Horsehead). The chemical time-scales become much longer than in the illuminated cloud edge and time-dependent effects are expected to be important (Hollenbach et al. 2009; Pilleri et al. 2013). Our reference isobaric model predicts that the hydrocarbon abundances peak again at N_H(face-on) $\gtrsim 9 \times 10^{21}$ cm^{-2}. This is consistent with the detection of hydrocarbons in dark clouds (Fossé et al. 2001) and with the spatial distribution of the low energy C$_2$H and c-C$_3$H$_2$ lines in our maps (peaking beyond the PDR, Fig. 10).

At least qualitatively, the abundances of small hydrocarbons beyond the cloud edge increase if x_e decreases. The ionisation fraction in a cloud interior can be low if the metallicity (Fe, etc.) is low or if the gas density is high ($x_e \propto \sqrt{\zeta_{CR}/n_H}$; see the different x_e gradients and resulting hydrocarbon abundances at large cloud depths in the models shown in Fig. 17). Finally, x_e can also be low if significant abundances ($\gtrsim 10^{-7}$) of negatively charged species exist (PAH, grains, or other large molecules to which electrons could easily attach). This of course is far from being proven and is still controversial. In such a case, the abundances of hydrocarbons like c-C$_3$H$_2$ are expected to increase by large factors (e.g. Lepp & Dalgarno 1988; Goicoechea et al. 2009).

Table 7. Observed and best isobaric PDR model column densities.

|	Observed	Model[a]
	$\log_{10}(N)$	$\log_{10}(N)$
	[cm^{-2}]	[cm^{-2}]
C$_2$H	14.6	14.1[b] –14.8[c]
l-C$_3$H$^+$	11.7	12.0[b] –12.7[c]
c-C$_3$H$_2$	13.1	12.2[b] –12.9[c]
l-H$_2$C$_3$	11.6	11.3[b] –12.0[c]
c-C$_3$H	12.3	11.3[b] –12.0[c]
l-C$_3$H	11.8	11.1[b] –11.9[c]
C$_4$H	13.6	12.3[b] –13.1[c]

Notes. [a] Isobaric model with $P = 10^8$ K cm^{-3} and $\chi = 2 \times 10^4$. Column densities integrated up to $N(H_2)$(face-on) $\simeq 10^{22}$ cm^{-2}. [b] Face-on configuration. [c] Column densities for an inclination angle of $\alpha \simeq 11°$ with respect to an edge-on geometry.

6.2. Comparison with observations

Because the Orion Bar does not have a perfect edge-on orientation, comparison of unidimensional PDR models and observations requires (i) a knowledge of the inclination angle α with respect to a pure edge-on configuration and (ii) knowledge of the equivalent face-on cloud depth (as in 1D models) of the observed line of sight, N_H(face-on) = N_H(observed) $\times \sin \alpha$. Different estimations have constrained the inclination angle to a maximum value of 15° (see discussion by Melnick et al. 2012, and references therein). This means a geometric column density enhancement of $\gtrsim 4$ with respect to a pure face-on PDR model predictions.

Table 7 lists the column densities inferred from our observations towards the PDR survey position and the column densities predicted by the reference isobaric model ($P = 10^8$ K cm^{-3}) integrated from $N(H_2)$(face-on) $\simeq 0$ to 10^{22} cm^{-2} and for two different inclinations (face-on and $\alpha \simeq 11°$). We note that for the reference model with $\alpha \simeq 11°$, the face-on extinction $A_V \simeq 10$ is equivalent to an angular scale $\sim 4''/\sin 11° \simeq 20''$ at the distance of the Orion Bar PDR (see Fig. 18), roughly the average beam of our millimetre observations.

In this range of values, the match between observations and our reference models is reasonably good. In particular, the column densities of all small hydrocarbons can be reproduced within factors of <3. The predicted variation of selected hydrocarbon abundance ratios with cloud depth (decreasing FUV field) is shown in Fig. 19. Taking the column density of l-C$_3$H as a reference (the model matches the observed value and this molecule is expected to show enhanced abundances in high x_e environments; see Fossé et al. 2001) the PDR model also reproduces the observed [C$_2$H]/[l-C$_3$H], [c-C$_3$H$_2$]/[l-C$_3$H], and [l-H$_2$C$_3$]/[l-C$_3$H] column density ratios within a factor of 2. Nevertheless, the column density of other species, C$_4$H in particular, is underestimated by a factor of 3 in the reference model, showing that the agreement is clearly not perfect. Still, given the complexity of the region and the geometrical simplicity of our models, this is much better than the order-of-magnitude differences reported between observations and models of low FUV-flux PDRs like the Horsehead (Pety et al. 2005, 2012). In this PDR, photo-destruction of PAHs or very small grains (VSGs) has been invoked to dominate the production of hydrocarbons like C$_2$H or c-C$_3$H$_2$. In the Orion Bar, the FUV flux is much higher and our model results suggest that photochemical models can explain the observed C$_2$H, C$_3$H, and C$_3$H$_2$ column
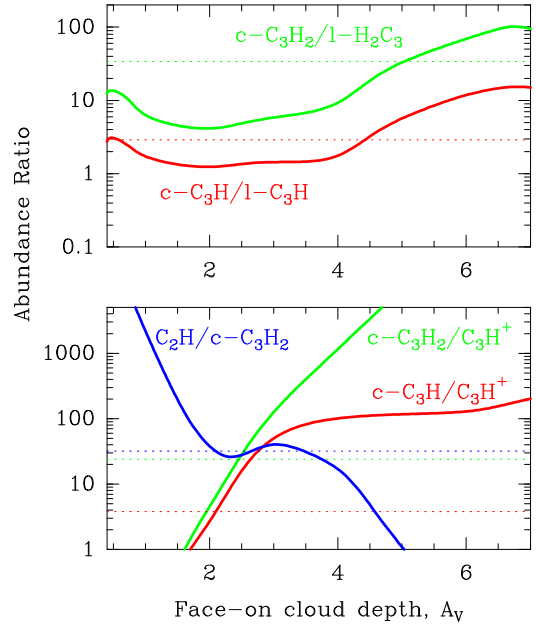
Fig. 19. Reference isobaric photochemical model for the Orion Bar with $P = 10^8$ K cm^{-3} and $\chi = 2 \times 10^4$ showing selected hydrocarbon abundance ratios as a function of A_V. The dashed horizontal lines show the ratios derived from the line survey.

densities without invoking a major contribution of PAH photodestruction. This conclusion would agree with the different spatial distributions of the PAHs and the C$_2$H and c-C$_3$H$_2$ emission seen along the Orion Bar. An important difference compared to the diffuse clouds or low UV-flux PDRs like the Horsehead is the much higher temperature attained by the gas and the elevated abundances of vibrationally excited H$_2$ activating many neutral-neutral reactions that likely play a minor role in the Horsehead or in diffuse clouds (see also Sect. 7.4).

For the more complex hydrocarbons (i.e. those with more than three carbon atoms), however, steady-state gas-phase models do not provide an entirely satisfactory fit. Time-dependent photochemical models, such as those applied to C-rich protoplanetary nebulae (e.g. Cernicharo 2004) show that the steady-state abundances of several organic species are different from those obtained during the gas time evolution. Hence, they may fit some specific hydrocarbons better despite the short time-scales in PDRs.

7. Discussion

7.1. Rotationally hot C$_4$H and l-C$_3$H$^+$

The rotational population analysis presented in Sect. 5.2 shows that C$_4$H, and to a lesser extent l-C$_3$H$^+$, have unusually high rotational temperatures compared to other small hydrocarbon molecules detected in the millimetre domain. This is more clearly seen in C$_4$H, which has a similar dipole moment and rotational spectroscopy to C$_2$H but shows much higher rotational temperatures ($T_{rot} \approx 77$ K versus 26 K). The C$_4$H radical has a complicated vibronic spectroscopy due to the proximity of the degenerated $^2\Pi$ excited electronic state (with a much higher 4.3 Debye dipole moment) only ~ 300 K above the X$^2\Sigma^+$ ground state. The Renner-Teller effect, spin-orbit interactions, and other couplings complicate the low energy rovibronic structure of C$_4$H (see e.g. Senent & Hochlaf 2010; Mazzotti et al. 2011). We suspect that radiative pumping contributes to the excitation of the

lowest lying bending modes of C_4H. Indeed, the derived rotational temperature for C_4H, $T_{rot} \approx 77$ K, is very similar to the dust temperature inferred towards the edge of the Orion Bar PDR (Arab et al. 2012). Therefore, it is plausible that the absorption of IR continuum photons from warm grains heated by the strong FUV-radiation field contributes to the C_4H excitation. In this context, the inferred T_{rot} would be more representative of the dust grain temperature in the PDR edge than of the gas temperature. The low energy modes of C_4H have been detected in the circumstellar envelope around the carbon-rich star IRC+10216 (Guelin et al. 1987). However, we have not detected rovibrational lines from the lowest energy C_4H bending mode, $\nu 7$ (Yamamoto et al. 1987a) probably due to the limited sensitivity of our line survey. The upper limit C_4H $[\nu 7]/[\nu = 0] < 10\%$ column density ratio we derive, however, is relatively high.

In Sect. 3.2.1 we concluded that l-C_3H^+ is a floppy molecule that very likely has low lying bending modes. Although we have not detected lines with their expected spectroscopic pattern, these levels can also be populated at relatively low gas temperatures through IR pumping. The l-C_3H^+ ion is a high dipole-moment molecule and, for the physical conditions in the Orion Bar PDR, its rotational levels are expected to be subthermally excited ($T_{ex} \ll T_k$). However, $T_{rot}(l$-$C_3H^+) \approx 46$ K is significantly higher[5] than the rotational temperatures inferred for all the other small hydrocarbons molecules (except C_4H). Again, this is an indication that IR pumping likely affects the l-C_3H^+ excitation.

## 7.2. Fractionation of $C^{13}CH$ and ^{13}CCH isotopomers

The inferred $[C^{13}CH]/[^{13}CCH] = 1.4 \pm 0.1$ (3σ) column density ratio towards the Orion Bar implies differential ^{13}C fractionation of CCH isotopologues. Sakai et al. (2010) also observed both isotopomers towards the dark cloud TMC-1 and the star-forming core exhibiting warm carbon-chain chemistry L1527. They derived $[C^{13}CH]/[^{13}CCH] = 1.6 \pm 0.4$ and 1.6 ± 0.1, respectively.

Furuya et al. (2011) suggested that the observed fractionation in cold and dense gas could be explained by the isotopomer exchange reaction

$$^{13}CCH + H \rightleftarrows C^{13}CH + H + \Delta E, \qquad (6)$$
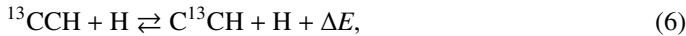
where $\Delta E \simeq 8$ K is the difference between the zero point energy (ZPE) of $C^{13}CH$ and ^{13}CCH (see also Tarroni & Carter 2003). Compared to a dark cloud, the Orion Bar shows different physical conditions driven by the presence of a strong UV radiation field: a large C^+ abundance, a higher fraction of H atoms with respect to H_2, and much more elevated gas temperatures. In the warm PDR gas, and in the absence of an activation barrier (suggested by Furuya et al. 2011), reaction (6) will not enhance the $C^{13}CH$ abundance significantly above $C^{13}CH$ (by only ~5% at ~150 K). Therefore, in addition to reaction (6), we suggest that reactions

$$^{13}C^+ + CCH \rightleftarrows C^{13}CH + C^+ + \Delta E' \qquad (7)$$

---
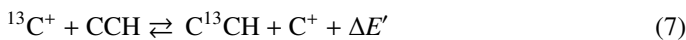
[5] The $T_{rot}(l$-$C_3H^+) = 178(3)$ K value inferred by McGuire et al. (2014) from their observation of the $J = 9 \rightarrow 8$, $10 \rightarrow 9$, and $11 \rightarrow 10$ lines is significantly higher than the value we obtain from our multi-line observations with the IRAM 30 m telescope. The presence of significant l-C_3H^+ emission dilution in the larger CSO telescope beam ($HPBW_{CSO}[arcsec] \approx 7000/Frequency[GHz]$, Mangum 1993) would lead to apparently larger values of T_{rot} if beam dilution is not corrected. In particular, we compute that a l-C_3H^+ emission source size of $\theta_s \lesssim 17''$ (leading to a beam dilution of $\eta_{bf}(CSO) \lesssim 0.23$ at ~225 GHz) reconciles both data sets.
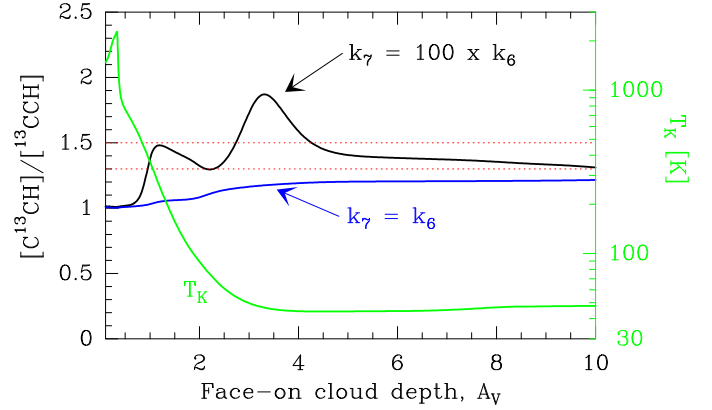
Fig. 20. Reference isobaric photochemical model for the Orion Bar with $P = 10^8$ K cm^{-3} and $\chi = 2 \times 10^4$. ^{13}C fractionation reactions have been included to explain the observed $[C^{13}CH]/[^{13}CCH]$ ratio (shown in the region enclosed by the red dashed lines). The black curve show a model in which the rate of the $^{13}C^+ + CCH$ reaction is 100 times higher than that of the $^{13}CCH + H$ reaction (see text).

and

$$^{13}C^+ + CCH \rightleftarrows {}^{13}CCH + C^+ + \Delta E'', \qquad (8)$$
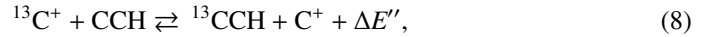
can contribute to the differential fractionation of $C^{13}CH$ and ^{13}CCH. Both isotopomers have relatively high ZPE differences with respect to CCH ($\Delta E' \simeq 63$ K and $\Delta E'' \simeq 55$ K, respectively) and both reactions (7) and (8) are more endothermic in the backward direction than reaction (6). We note that in a high UV-flux PDR, the gas temperature is high enough to prevent significant $^{13}C^+$ depletion through the reaction

$$^{13}C^+ + CO \rightleftarrows C^+ + {}^{13}CO + 34.8 \, \text{K} \qquad (9)$$
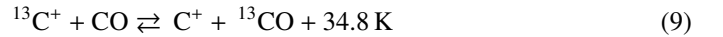
(see Ossenkopf et al. 2013, for low $[C\,\textsc{ii}]/[^{13}C\,\textsc{ii}]$ line intensity ratios towards the Orion Bar). Owing to the higher H atom abundance in PDRs, reaction (7) needs to be faster (e.g. forming $C^{13}CH$) than the backward isotopomer exchange reaction (6) (e.g. destroying $C^{13}CH$). Figure 20 shows our reference isobaric model in which ^{13}C fractionation reactions involving $^{13}C^+$, ^{13}CO, and $H^{13}CO^+$ have been included (see Langer et al. 1984; Le Bourlot et al. 1993). The blue curve shows the predicted depth-dependent $[C^{13}CH]/[^{13}CCH]$ abundance ratio in a model with the same rate for reactions (6)–(8). In this model, the exchange reactions with H atoms dominate and $C^{13}CH$ only fractionates at large cloud depths (by ~20% at ~50 K) where the gas temperature significantly decreases. The black curve shows a model with $k_7 = k_8 = 100 \times k_6$. In this model, fractionation reactions with $^{13}C^+$ can dominate in the warm UV-illuminated gas and the $[C^{13}CH]/[^{13}CCH]$ ratio already increases at the cloud surface (becoming compatible with our observations). We note, however, that reaction (6) must always be present, otherwise the $[C^{13}CH]/[^{13}CCH]$ ratio will be much higher than the observed value as the gas temperature decreases. Quantum calculations and/or laboratory experiments are needed to constrain the reaction rates and potential energy activation barriers of these processes in detail.

7.3. Cyclic versus linear isomers

The linear and cyclic isomers of a given hydrocarbon species can have different behaviours with respect to neutral-neutral and ion-neutral reactions, and thus with respect to different physical conditions. Fossé et al. (2001) reported high $[c$-$C_3H_2]/[l$-$H_2C_3]$ (~28) and $[c$-$C_3H]/[l$-$C_3H]$ (~13) abundance ratios towards the

cyanopolyyne peak in the cold dark cloud TMC-1. These ratios are higher than those observed in diffuse and translucent clouds: $[c\text{-}C_3H_2]/[l\text{-}H_2C_3] \simeq$ (3–5) (Cernicharo et al. 1999) and $[c\text{-}C_3H]/[l\text{-}C_3H] \simeq 2$ (Turner et al. 2000). Teyssier et al. (2005) showed that the cyclic-to-linear C_3H_2 column density ratio in the Horsehead nebula increases from the UV-illuminated layers to the shielded cloud interior. Fossé et al. (2001) also explored the chemistry in TMC-1 and concluded that the cyclic-to-linear abundance ratio of C_3H_2 increases with decreasing electron abundances. Our reference model for the Orion Bar also predicts that both the $[c\text{-}C_3H_2]/[l\text{-}H_2C_3]$ and the $[c\text{-}C_3H]/[l\text{-}C_3H]$ ratios increase with A_V as the FUV-radiation field is attenuated and x_e decreases (see Fig. 19). This suggests that the formation of the linear isomers (less stable energetically) is favoured in the warm UV-illuminated gas with high ionisation fractions. The low $[c\text{-}C_3H]/[l\text{-}C_3H] \simeq 3$ abundance ratio we infer towards the Orion Bar is the same as that found in the PDR around the protoplanetary nebula CRL 618 (Pardo & Cernicharo 2007) and slightly higher than that inferred towards the Horsehead PDR (~1.8) (Teyssier et al. 2004). Such low abundance ratios (≤3) therefore seem a signature of the presence of FUV radiation and high ionisation fractions. On the other hand, the $[c\text{-}C_3H_2]/[l\text{-}H_2C_3] \simeq 34$ ratio we infer towards the Orion Bar is much higher than that observed in the Horsehead PDR (≃3.5) and in diffuse clouds. At this point, the reason for such a difference is not clear, but may suggest that in the Orion Bar, the $c\text{-}C_3H_2$ abundance is enhanced by formation routes not considered in our pure-gas phase models.

7.4. C_2H versus $c\text{-}C_3H_2$ in other environments

In order to investigate the role of UV radiation and gas density in the formation of the small hydrocarbons, we compare the column density of several hydrocarbons in different environments. The considered sources are the Monoceros R2 (Mon R2) ultra-compact H II region ($\chi > 10^5$ in Draine units and $\chi/n_H \simeq 10^{-1}$ cm^3 dissociation parameter, e.g. Pilleri et al. 2013), the Orion Bar PDR ($\chi \approx 10^4$ and $\chi/n_H \simeq 0.5$ cm^3, e.g. Marconi et al. 1998), the nucleus of the starburst galaxy M 82 ($\chi \approx 6 \times 10^3$ and $\chi/n_H \simeq 0.06$ cm^3, e.g. Fuente et al. 2008), the reflection nebula NGC 7023 ($\chi \approx 10^3$ and $\chi/n_H \simeq 0.06$ cm^3, e.g. Joblin et al. 2010), diffuse clouds ($\chi \approx 1$ and $\chi/n_H \simeq 10^{-2}$ cm^3, e.g. Liszt et al. 2012), and the Horsehead PDR ($\chi \approx 60$ and $\chi/n_H \simeq 6 \times 10^{-3}$ cm^3, e.g. Pety et al. 2012). We also considered three sources shielded from external UV-illumination: the cold and dense cloud TMC-1, the low-mass protostar (hot corino) IRAS 16293-2422, and the dense core L1498 (the three with a $\chi/n_H \ll 10^{-4}$ cm^3).

The variation of incident UV radiation flux affects the relative abundance of certain hydrocarbons. As expected for widespread interstellar molecules, intense C_2H and $c\text{-}C_3H_2$ emission is detected in all the above sources. However, the observed $[C_2H]/[c\text{-}C_3H_2]$ column density ratio varies from highly irradiated sources like the Orion Bar (~32) to UV-shielded sources (<10) (see Fig. 21). In fact, the observed $[C_2H]/[c\text{-}C_3H_2]$ ratios seem to scale with χ/n_H, the critical parameter determining most of the PDR properties. In the Orion Bar model this can be readily seen in the predicted decrease of the $[C_2H]/[c\text{-}C_3H_2]$ abundance ratio with increasing A_V (Fig. 19). This trend can be explained by the effect of UV radiation on the chemical processes governing the hydrocarbon formation. In particular, the chemistry in cold shielded gas is driven by the ionisation of H_2 by cosmic rays, and the hydrocarbons are mainly produced by
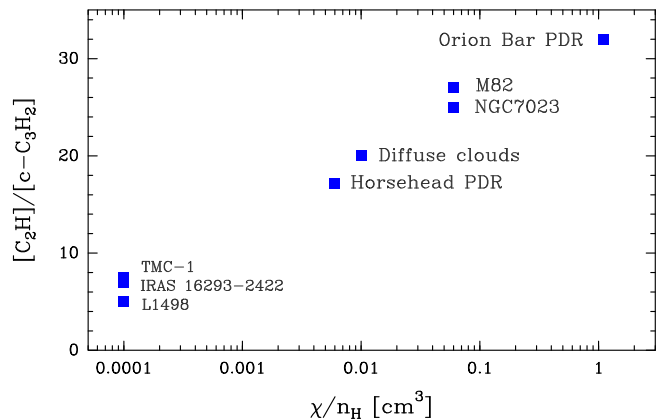
Fig. 21. Observed $[C_2H]/[c\text{-}C_3H_2]$ column density ratios as a function of χ/n_H dissociation parameter (see text) in the Orion Bar PDR, the nucleus of M82 (Aladro et al. 2011), NGC 7023 (NW PDR; Fuente et al. 1993, 2003), diffuse clouds (averaged abundances towards B0355, B0415, B2200, and B2251; Liszt et al. 2012), Horsehead PDR (Pety et al. 2012), TMC-1 (towards the cyanopolyyne peak; Ohishi et al. 1992), IRAS 16293-2422 (van Dishoeck et al. 1995), and L1498 (Tafalla et al. 2006; Padovani et al. 2009).

ion-molecule barrierless reactions. Time-dependent effects and grain surface processes are also likely important deep inside clouds (Pilleri et al. 2013). In strongly UV irradiated environments, the presence of C^+ and H_2^* triggers the rapid formation of hydrocarbons ions like CH^+, CH_2^+, and CH_3^+ (see Sect. 6.2). In the associated warm gas, neutral-neutral reactions (e.g. reactions of C_n or neutral hydrocarbons with H and H_2) that do not play a role in the cold gas become efficient (see e.g. Cernicharo 2004). They allow high abundances of hydrocarbon molecules to be maintained despite the large UV field. For the typical densities in PDRs (~10^5 cm^{-3}) our gas-phase models predict higher column densities of C_2H in strongly irradiated PDRs ($\chi > 1000$) than in low UV-flux PDRs. On the other hand, they predict decreasing column densities of $c\text{-}C_3H_2$ for $\chi > 1000$. Therefore, the $[C_2H]/[c\text{-}C_3H_2]$ ratio is expected to increase with the strength of the UV radiation field and observations seem to confirm this. For high UV-fluxes, photodissociation is the main destruction mechanism of C_2H and $c\text{-}C_3H_2$ up to a few A_V. The $c\text{-}C_3H_2$ photodissociation rate is a factor of ~4 higher than that of C_2H (e.g. van Dishoeck et al. 2006). For the Orion Bar physical conditions this contributes to the fact that C_2H is predicted to peak slightly closer to the dissociation front, and also to the general increase in $c\text{-}C_3H_2$ column density compared to C_2H when the UV field decreases.

The dense PDR around Mon R2 H II region (not shown in Fig. 21) displays the highest $[C_2H]/[c\text{-}C_3H_2] \sim 125$ ratio (Pilleri et al. 2013). This is a more extreme environment where the gas is heated to very high temperatures, favouring the production of simple hydrocarbons like CH^+ (Pilleri et al. 2014) or C_2H (Pilleri et al. 2013) through the hot-gas PDR chemistry described in Sect. 6.1.

Hydrocarbons are also detected in diffuse clouds (e.g. Liszt et al. 2012, 2014), where radiation fields ($\chi \approx 1$) and densities ($n_H \approx 100$ cm^{-3}) are lower than in PDRs. However, owing to the similar χ/n_H dissociation parameter, diffuse clouds and low-FUV flux PDRs are expected to share common characteristics. The $[C_2H]/[c\text{-}C_3H_2]$ ratio inferred in diffuse clouds (~20) is more similar to the one inferred in the Horsehead PDR (~17), a low UV-flux and low χ/n_H PDR, and indeed is lower than the value observed in the Orion Bar (~32).

In contrast to the low and high illumination PDRs, dark clouds and hot corinos show the lowest $[C_2H]/[c\text{-}C_3H_2]$ ratios (<10). The exact ratios in these UV-shielded environments are probably very time-dependent, i.e. the molecular abundances depends on the evolutive stage of the clouds.

In a broader extragalactic context, the nucleus of M82, which is the most studied example of an extragalactic starburst, shares similar photochemical characteristics with high UV-flux galactic PDRs. The chemistry of its nucleus seems to be the result of an old starburst mainly affected by the influence of intense UV fields from massive stars, where star formation has almost exhausted the molecular gas reservoir (Fuente et al. 2008). In the study of the chemical complexity of the NE lobe of the M 82 galaxy carried out by Aladro et al. (2011), they found that C_2H is the brightest spectral feature in the 1.3 mm and 2 mm bands. The $[C_2H]/[c\text{-}C_3H_2]$ ratio observed towards M 82 ($\sim$27) lies in between that of the Orion Bar ($\sim$32) and of NGC 7023 ($\sim$18–32; see Fuente et al. 1993, 2003).

In summary, observations and models suggest that the $[C_2H]/[c\text{-}C_3H_2]$ ratio is a good tracer of increasing χ/n_H values. Ratios above $\sim$10 suggest the presence of UV radiation ($\chi > 1$), with $[C_2H]/[c\text{-}C_3H_2]$ ratios above $\sim$30 probing the presence of strong radiation fields ($\chi > 10^3$). In combination with the observation of low $[c\text{-}C_3H]/[l\text{-}C_3H]$ isomeric ratios ($\leq$3), characteristic of high x_e environments, these ratios are good diagnostics of the presence of an active photochemistry. On the other hand, $[C_2H]/[c\text{-}C_3H_2] \lesssim 10$ and $[c\text{-}C_3H]/[l\text{-}C_3H] \gtrsim 10$ ratios are indicative of low x_e gas shielded from external UV radiation.

7.5. PAH/HAC photodestruction and grain surface chemistry

Another difference between low and high UV-illumination environments is the spatial distribution of the hydrocarbons emission. The C_2H and $c\text{-}C_3H_2$ emission spatially correlates very well in the Horsehead PDR (Pety et al. 2005), diffuse clouds (Lucas & Liszt 2000; Gerin et al. 2011), and in the Orion Bar PDR (Fig. 10). Furthermore, a tight correlation between the PAHs and the small hydrocarbon emission was found in the Horsehead PDR from high angular resolution interferometric observations (Pety et al. 2005). Following previous suggestions (Fossé et al. 2000; Fuente et al. 2003; Teyssier et al. 2004), Pety et al. (2005) proposed that the photo-fragmentation of PAHs likely increases the abundance of small hydrocarbons in the Horsehead. In the Orion Bar, the 8 μm PAH emission and the C_2H and $c\text{-}C_3H_2$ emission clearly show a different spatial distribution (Fig. 10). Lacking higher angular resolution observations and a complete model of the PAH/VSG photoerosion (Pilleri et al. 2012), we can only conclude that in strongly irradiated PDRs like the Orion Bar, photodestruction of PAHs is not a necessary condition to explain the observed abundances of the simplest hydrocarbons.

Nevertheless, additional top-down formation routes for hydrocarbon molecules not included in our gas-phase models may take place in PDRs. In particular, recent ultra-high vacuum experiments with carbonaceous grains show that hydrogen atoms attached to the grain surface can efficiently react and produce a large variety of organic molecules, from PAHs to acetylene (Merino et al. 2014). We note that C_2H_2 photodissociation produces C_2H and the reaction of C_2H_2 with C^+ forms the observed hydrocarbon ion $l\text{-}C_3H^+$, an important gas-phase precursor of C_3H_2 and C_3H. In addition, laboratory experiments performed by Alata et al. (2014) show that the photodestruction of hydrogenated amorphous carbon (HAC) grains, observed in the diffuse medium (Duley & Williams 1983), also leads to the production of small hydrocarbons (such as CH_4) that can trigger the gas-phase formation of other hydrocarbons.

Since PAHs, carbonaceous grains, and H atoms are abundant in PDRs, both the photodestruction of PAHs/HACs and the chemistry that takes place at the surfaces of carbonaceous grains will need to be taken into account in future PDR models.

8. Summary and conclusions

We have investigated the spatial distribution and chemistry of small hydrocarbons in the strongly UV-irradiated Orion Bar PDR. We performed a complete millimetre line survey towards the Orion Bar dissociation front (the "CO$^+$ peak") covering a bandwidth of $\sim$220 GHz using the IRAM 30 m telescope. These observations have been complemented with $\sim2' \times 2'$ maps of the C_2H and $c\text{-}C_3H_2$ emission. Approximately 40% of the detected lines have been assigned to hydrocarbons (C_2H, C_4H, $c\text{-}C_3H_2$, $c\text{-}C_3H$, C^{13}CH, ^{13}CCH, $l\text{-}C_3H$, and $l\text{-}H_2C_3$ in decreasing order of abundance). We also present the detection of nine rotational lines of the newly discovered hydrocarbon ion $l\text{-}C_3H^+$, allowing us to improve its spectroscopic constants. No anions, lines from vibrationally excited states, or deuterated hydrocarbons were detected. A detailed analysis of the excitation conditions and chemistry was carried out. In particular, we obtained the following results:

– Although the Orion Bar is a harsh environment, the millimetre line survey shows a relatively rich molecular line spectra, with more than 200 lines arising from hydrocarbons.

– The inferred rotational temperatures range from 17 to 77 K (most species have $T_{rot} < 30$ K) and column densities ranging from 10^{11} to 10^{14} cm^{-2}. C_2H is the most abundant of the detected hydrocarbons ($\sim10^{-8}$ with respect to H nuclei).

– We obtain similar rotational temperatures for ortho and para forms of cyclic and linear C_3H_2. The inferred $c\text{-}C_3H_2$ ortho-to-para ratio is 2.8$\pm$0.6, consistent with the high temperature limit.

– The $[C^{13}CH]/[^{13}CCH]$ ratio is 1.4 $\pm$ 0.1 and shows that fractionation processes differently affect the two ^{13}C isotopes of C_2H. We suggest that reactions of C_2H with $^{13}C^+$, as well as reactions of C_2H isotopologues with H atoms, can explain the observed levels of C^{13}CH fractionation in the Orion Bar.

– We constrain the beam-averaged physical conditions from non-LTE models of C_2H and $c\text{-}C_3H_2$. The best fits for C_2H are obtained for $T_k \gtrsim 150$ K and $n(H_2) \gtrsim 10^5$ cm^{-3}. Slightly denser gas and lower temperatures are required to fit the $c\text{-}C_3H_2$ lines.

– We provide accurate upper limit abundances for chemically related carbon bearing molecules that are not detected in the PDR: $[C_2D]/[C_2H] < 0.2\%$, $[C_2H^-]/[C_2H] < 0.007\%$, and $[C_4H^-]/[C_4H] < 0.05\%$.

– Hydrocarbon molecules show moderate abundances towards the FUV-illuminated edge of the cloud, but they are also abundant in the more shielded cloud interior. The observed decrease of the $[C_2H]/[c\text{-}C_3H_2]$ column density ratio from the dissociation front to the molecular peak and observations towards different environments suggest that the $[C_2H]/[c\text{-}C_3H_2]$ abundance ratio increases with increasing χ/n_H values. In addition, the observation of low $[c\text{-}C_3H]/[l\text{-}C_3H]$ ratios ($\leq$3) in the Orion Bar PDR probes a high electron abundance environment.

– We compare the inferred column densities with updated photochemical models. Our models can reasonably match the observed column densities of most hydrocarbons (within

factors of <3). The largest discrepancy is for C_4H: our model underestimates the C_4H column density by a factor of ~3. Since the observed spatial distribution of the C_2H and c-C_3H_2 emission is similar but does not follow the PAH emission, we conclude that the photodestruction of PAHs is not a necessary requirement in high UV-flux PDRs to explain the observed abundances of the smallest hydrocarbons. Instead, endothermic reactions (or with barriers) between C^+, radicals, and H_2 can dominate their formation. Still, photoerosion of PAHs/HACs/VSGs and surface chemistry on carbonaceous grains may be needed to explain the abundances of more complex hydrocarbons.

– The electron abundance influences the hydrocarbon chemistry beyond the cloud layers directly exposed to the UV radiation field. Unfortunately, the ionisation fraction depends on the poorly known abundances of low ionisation metals, on the density profile, and on the controversial presence of negatively charged PAH, grains, or polyatomic anions in cloud interiors. Improving our knowledge of these aspects, and on the products and details of PAH/HAC/VSG photoerosion and grain surface chemistry processes, will help us to improve our knowledge of the interstellar carbon chemistry.

References

Agúndez, M., Cernicharo, J., & Goicoechea, J. R. 2008a, A&A, 483, 831
Agúndez, M., Cernicharo, J., Guélin, M., et al. 2008b, A&A, 478, L19
Agúndez, M., Goicoechea, J. R., Cernicharo, J., Faure, A., & Roueff, E. 2010, ApJ, 713, 662
Aladro, R., Martín, S., Martín-Pintado, J., et al. 2011, A&A, 535, A84
Alata, I., Cruz-Diaz, G. A., Muñoz Caro, G. M., & Dartois, E. 2014, A&A, 569, A119
Allers, K. N., Jaffe, D. T., Lacy, J. H., Draine, B. T., & Richter, M. J. 2005, ApJ, 630, 368
Andree-Labsch, S., Ossenkopf, V., & Röllig, M. 2014, A&A, submitted [arXiv:1405.5553]
Arab, H., Abergel, A., Habart, E., et al. 2012, A&A, 541, A19
Batrla, W., & Wilson, T. L. 2003, A&A, 408, 231
Baulch, D. L. 2005, J. Phys. Chem. Ref. Data, 34, 757
Bell, M. B., Sears, T. J., & Matthews, H. E. 1982, ApJ, 255, L75
Bell, M. B., Matthews, H. E., & Sears, T. J. 1983, A&A, 127, 241
Bernard-Salas, J., Habart, E., Arab, H., et al. 2012, A&A, 538, A37
Berné, O., Fuente, A., Goicoechea, J. R., et al. 2009, ApJ, 706, L160
Black, J. H., & van Dishoeck, E. F. 1987, ApJ, 322, 412
Botschwina, P., Stein, C., Sebald, P., Schröder, B., & Oswald, R. 2014, ApJ, 787, 72
Brünken, S., Kluge, L., Stoffels, A., Asvany, O., & Schlemmer, S. 2014, ApJ, 783, L4
Burton, M. G., Hollenbach, D. J., & Tielens, A. G. G. M. 1990, ApJ, 365, 620
Castor, J. I. 1970, MNRAS, 149, 111
Cernicharo, J. 2004, ApJ, 608, L41
Cernicharo, J. 2012, EAS Pub. Ser., 58, 251
Cernicharo, J., & Guelin, M. 1996, A&A, 309, L27
Cernicharo, J., Guelin, M., & Askne, J. 1984, A&A, 138, 371
Cernicharo, J., Guelin, M., Menten, K. M., & Walmsley, C. M. 1987, A&A, 181, L1
Cernicharo, J., Gottlieb, C. A., Guelin, M., et al. 1991a, ApJ, 368, L39
Cernicharo, J., Gottlieb, C. A., Guelin, M., et al. 1991b, ApJ, 368, L43
Cernicharo, J., Cox, P., Fossé, D., & Güsten, R. 1999, A&A, 351, 341
Cernicharo, J., Guélin, M., & Kahane, C. 2000, A&AS, 142, 181
Chabot, M., Béroff, K., Gratier, P., Jallat, A., & Wakelam, V. 2013, ApJ, 771, 90
Chandra, S., & Kegel, W. H. 2000, A&AS, 142, 113
Combes, F., Boulanger, F., Encrenaz, P. J., et al. 1985, A&A, 147, L25
Coutens, A., Vastel, C., Caux, E., et al. 2012, A&A, 539, A132
De Beck, E., Lombaert, R., Agúndez, M., et al. 2012, A&A, 539, A108
DeFrees, D. J., & McLean, A. D. 1986, ApJ, 308, L31
Duley, W. W., & Williams, D. A. 1983, MNRAS, 205, 67
Dykstra, C. E., Parsons, C. A., & Oates, C. L. 1979, J. Am. Chem. Soc., 101, 1962
Fortenberry, R. C., Huang, X., Crawford, T. D., & Lee, T. J. 2013, ApJ, 772, 39
Fossé, D., Cesarsky, D., Gerin, M., Lequeux, J., & Tiné, S. 2000, in ISO Beyond the Peaks: The 2nd ISO Workshop on Analytical Spectroscopy, eds. A. Salama, M. F. Kessler, K. Leech, & B. Schulz, ESA SP, 456, 91
Fossé, D., Cernicharo, J., Gerin, M., & Cox, P. 2001, ApJ, 552, 168
Fuente, A., Martin-Pintado, J., Cernicharo, J., & Bachiller, R. 1993, A&A, 276, 473
Fuente, A., Rodriguez-Franco, A., & Martin-Pintado, J. 1996, A&A, 312, 599
Fuente, A., Rodríguez-Franco, A., García-Burillo, S., Martín-Pintado, J., & Black, J. H. 2003, A&A, 406, 899
Fuente, A., García-Burillo, S., Gerin, M., et al. 2005, ApJ, 619, L155
Fuente, A., García-Burillo, S., Usero, A., et al. 2008, A&A, 492, 675
Furuya, K., Aikawa, Y., Sakai, N., & Yamamoto, S. 2011, ApJ, 731, 38
Gerin, M., Kaźmierczak, M., Jastrzebska, M., et al. 2011, A&A, 525, A116
Goicoechea, J. R., & Le Bourlot, J. 2007, A&A, 467, 1
Goicoechea, J. R., Rodríguez-Fernández, N. J., & Cernicharo, J. 2004, ApJ, 600, 214
Goicoechea, J. R., Pety, J., Gerin, M., et al. 2006, A&A, 456, 565
Goicoechea, J. R., Pety, J., Gerin, M., Hily-Blant, P., & Le Bourlot, J. 2009, A&A, 498, 771
Goicoechea, J. R., Joblin, C., Contursi, A., et al. 2011, A&A, 530, L16
Goldsmith, P. F., & Langer, W. D. 1999, ApJ, 517, 209
Gottlieb, C. A., Gottlieb, E. W., & Thaddeus, P. 1983a, ApJ, 264, 740
Gottlieb, C. A., Gottlieb, E. W., Thaddeus, P., & Kawamura, H. 1983b, ApJ, 275, 916
Gottlieb, C. A., Vrtilek, J. M., Gottlieb, E. W., Thaddeus, P., & Hjalmarson, A. 1985, ApJ, 294, L55
Gottlieb, C. A., Gottlieb, E. W., Thaddeus, P., & Vrtilek, J. M. 1986, ApJ, 303, 446
Guelin, M., Green, S., & Thaddeus, P. 1978, ApJ, 224, L27
Guelin, M., Friberg, P., & Mezaoui, A. 1982, A&A, 109, 23
Guelin, M., Cernicharo, J., Kahane, C., Gomez-Gonzalez, J., & Walmsley, C. M. 1987, A&A, 175, L5
Guelin, M., Cernicharo, J., Travers, M. J., et al. 1997, A&A, 317, L1
Gupta, H., Rimmer, P., Pearson, J. C., et al. 2010, A&A, 521, L47
Habart, E., Dartois, E., Abergel, A., et al. 2010, A&A, 518, L116
Hogerheijde, M. R., Jansen, D. J., & van Dishoeck, E. F. 1995, A&A, 294, 792
Hollenbach, D., Kaufman, M. J., Bergin, E. A., & Melnick, G. J. 2009, ApJ, 690, 1497
Jansen, D. J., Spaans, M., Hogerheijde, M. R., & van Dishoeck, E. F. 1995, A&A, 303, 541
Joblin, C., Pilleri, P., Montillaud, J., et al. 2010, A&A, 521, L25
Kanata, H., Yamamoto, S., & Saito, S. 1987, Chem. Phys. Lett., 140, 221
Langer, W. D., Graedel, T. E., Frerking, M. A., & Armentrout, P. B. 1984, ApJ, 277, 581
Langer, W. D., Velusamy, T., Kuiper, T. B. H., et al. 1997, ApJ, 480, L63
Le Bourlot, J., Pineau Des Forets, G., Roueff, E., & Flower, D. R. 1993, A&A, 267, 233
Le Bourlot, J., Le Petit, F., Pinto, C., Roueff, E., & Roy, F. 2012, A&A, 541, A76
Le Petit, F., Nehmé, C., Le Bourlot, J., & Roueff, E. 2006, ApJS, 164, 506
Lepp, S., & Dalgarno, A. 1988, ApJ, 324, 553
Lis, D. C., & Schilke, P. 2003, ApJ, 597, L145
Liszt, H., Sonnentrucker, P., Cordiner, M., & Gerin, M. 2012, ApJ, 753, L28
Liszt, H. S., Pety, J., Gerin, M., & Lucas, R. 2014, A&A, 564, A64
Lovas, F. J., Suenram, R. D., Ogata, T., & Yamamoto, S. 1992, ApJ, 399, 325
Lucas, R., & Liszt, H. S. 2000, A&A, 358, 1069
Maluendes, S. A., McLean, A. D., Yamashita, K., & Herbst, E. 1993, J. Chem. Phys., 99, 2812
Mangum, J. G. 1993, PASP, 105, 117
Marcelino, N., Cernicharo, J., Agúndez, M., et al. 2007, ApJ, 665, L127
Marconi, A., Testi, L., Natta, A., & Walmsley, C. M. 1998, A&A, 330, 696
Martín, S., Mauersberger, R., Martín-Pintado, J., Henkel, C., & García-Burillo, S. 2006, ApJS, 164, 450
Mazzotti, F. J., Raghunandan, R., Esmail, A. M., Tulej, M., & Maier, J. P. 2011, J. Chem. Phys., 134, 164303
McCarthy, M., Gottlieb, C., & Thaddeus, P. 1995, J. Mol. Spectr., 173, 303
McEwan, M. J., Scott, G. B. I., Adams, N. G., et al. 1999, ApJ, 513, 287
McGuire, B. A., Carroll, P. B., Loomis, R. A., et al. 2013, ApJ, 774, 56
McGuire, B. A., Carroll, P. B., Sanders, J. L., et al. 2014, MNRAS, 442, 2901
Meier, D. S., & Turner, J. L. 2005, ApJ, 618, 259
Meier, D. S., & Turner, J. L. 2012, ApJ, 755, 104
Melnick, G. J., Tolls, V., Goldsmith, P. F., et al. 2012, ApJ, 752, 26

Menten, K. M., Reid, M. J., Forbrich, J., & Brunthaler, A. 2007, A&A, 474, 515
Merino, P., Švec, M., Martinez, J. I., et al. 2014, Nat. Comm., 5
Müller, H. S. P., Klaus, T., & Winnewisser, G. 2000, A&A, 357, L65
Müller, H. S. P., Thorwirth, S., Roth, D. A., & Winnewisser, G. 2001, A&A, 370, L49
Müller, H. S. P., Schlöder, F., Stutzki, J., & Winnewisser, G. 2005, J. Mol. Struct., 742, 215
Müller, H. S. P., Goicoechea, J. R., Cernicharo, J., et al. 2014, A&A, 569, L5
Nagy, Z., Van der Tak, F. F. S., Ossenkopf, V., et al. 2013, A&A, 550, A96
Neufeld, D. A., Gusdorf, A., Güsten, R., et al. 2014, ApJ, 781, 102
Ohishi, M., Irvine, W. M., & Kaifu, N. 1992, in Astrochemistry of Cosmic Phenomena, ed. P. D. Singh, IAU Symp., 150, 171
Ossenkopf, V., Röllig, M., Neufeld, D. A., et al. 2013, A&A, 550, A57
Padovani, M., Walmsley, C. M., Tafalla, M., Galli, D., & Müller, H. S. P. 2009, A&A, 505, 1199
Pardo, J. R., & Cernicharo, J. 2007, ApJ, 654, 978
Pardo, J. R., Encrenaz, P. J., & Breton, D. 2001, in Preserving the Astronomical Sky, eds. R. J. Cohen, & W. T. Sullivan, IAU Symp., 196, 255
Pardo, J. R., Cernicharo, J., Goicoechea, J. R., Guélin, M., & Asensio Ramos, A. 2007, ApJ, 661, 250
Parmar, P. S., Lacy, J. H., & Achtermann, J. M. 1991, ApJ, 372, L25
Pety, J., Teyssier, D., Fossé, D., et al. 2005, A&A, 435, 885
Pety, J., Gratier, P., Guzmán, V., et al. 2012, A&A, 548, A68
Pickett, H. M., Poynter, R. L., Cohen, E. A., et al. 1998, J. Quant. Spectr. Rad. Transf., 60, 883
Pilleri, P., Montillaud, J., Berné, O., & Joblin, C. 2012, A&A, 542, A69
Pilleri, P., Treviño-Morales, S., Fuente, A., et al. 2013, A&A, 554, A87
Pilleri, P., Fuente, A., Gerin, M., et al. 2014, A&A, 561, A69
Pitts, W. M., Pasternack, L., & McDonald, J. R. 1982, Chem. Phys., 68, 417
Sakai, N., Saruwatari, O., Sakai, T., Takano, S., & Yamamoto, S. 2010, A&A, 512, A31
Saleck, A. H., Eigler, K., Simon, R., Vowinkel, B., & Winnewisser, G. 1992, in Astronomische Gesellschaft Abstract Series 7, ed. G. Klare, 83
Saleck, A. H., Simon, R., Winnewisser, G., & Wouterloot, J. G. A. 1994, Canad. J. Phys., 72, 747
Senent, M. L., & Hochlaf, M. 2010, ApJ, 708, 1452
Sheehan, S. M., Parsons, B. F., Zhou, J., et al. 2008, J. Chem. Phys., 128, 034301
Simon, R., Stutzki, J., Sternberg, A., & Winnewisser, G. 1997, A&A, 327, L9
Sobolev, V. V. 1960, Moving envelopes of stars (Cambridge: Harvard University Press)
Spielfiedel, A., Feautrier, N., Najar, F., et al. 2012, MNRAS, 421, 1891
Stoerzer, H., Stutzki, J., & Sternberg, A. 1995, A&A, 296, L9

Tafalla, M., Santiago-García, J., Myers, P. C., et al. 2006, A&A, 455, 577
Tarroni, R., & Carter, S. 2003, J. Chem. Phys., 119, 12878
Tercero, B., Cernicharo, J., Pardo, J. R., & Goicoechea, J. R. 2010, A&A, 517, A96
Teyssier, D., Fossé, D., Gerin, M., et al. 2004, A&A, 417, 135
Teyssier, D., Hily-Blant, P., Gerin, M., et al. 2005, in ESA SP 577, ed. A. Wilson, 423
Thaddeus, P., Gottlieb, C. A., Hjalmarson, A., et al. 1985a, ApJ, 294, L49
Thaddeus, P., Vrtilek, J. M., & Gottlieb, C. A. 1985b, ApJ, 299, L63
Tielens, A. G. G. M., & Hollenbach, D. 1985, ApJ, 291, 722
Tielens, A. G. G. M., Meixner, M. M., van der Werf, P. P., et al. 1993, Science, 262, 86
Tucker, K. D., Kutner, M. L., & Thaddeus, P. 1974, ApJ, 193, L115
Turner, B. E., Herbst, E., & Terzieva, R. 2000, ApJS, 126, 427
van der Tak, F. F. S., Black, J. H., Schöier, F. L., Jansen, D. J., & van Dishoeck, E. F. 2007, A&A, 468, 627
van der Tak, F. F. S., Nagy, Z., Ossenkopf, V., et al. 2013, A&A, 560, A95
van der Werf, P. P., Stutzki, J., Sternberg, A., & Krabbe, A. 1996, A&A, 313, 633
van der Werf, P. P., Goss, W. M., & O'Dell, C. R. 2013, ApJ, 762, 101
van der Wiel, M. H. D., van der Tak, F. F. S., Ossenkopf, V., et al. 2009, A&A, 498, 161
van Dishoeck, E. F., & Black, J. H. 1988, ApJ, 334, 771
van Dishoeck, E. F., Blake, G. A., Jansen, D. J., & Groesbeck, T. D. 1995, ApJ, 447, 760
van Dishoeck, E. F., Jonkheid, B., & van Hemert, M. C. 2006, Faraday Discussions, 133, 231
Vrtilek, J. M., Gottlieb, C. A., Langer, W. D., Thaddeus, P., & Wilson, R. W. 1985, ApJ, 296, L35
Vrtilek, J. M., Gottlieb, C. A., & Thaddeus, P. 1987, ApJ, 314, 716
Vrtilek, J. M., Gottlieb, A., Gottlieb, E. W., Killian, T. C., & Thaddeus, P. 1990, ApJ, 364, L53
Walmsley, C. M., Natta, A., Oliva, E., & Testi, L. 2000, A&A, 364, 301
Wilson, T. L., & Rood, R. 1994, ARA&A, 32, 191
Woon, D. E. 1995, Chem. Phys. Lett., 244, 45
Wootten, A., Bozyan, E. P., Garrett, D. B., Loren, R. B., & Snell, R. L. 1980, ApJ, 239, 844
Yamamoto, S., & Saito, S. 1994, J. Chem. Phys., 101, 5484
Yamamoto, S., Saito, S., Guelin, M., et al. 1987a, ApJ, 323, L149
Yamamoto, S., Saito, S., Ohishi, M., et al. 1987b, ApJ, 322, L55
Young Owl, R. C., Meixner, M. M., Wolfire, M., Tielens, A. G. G. M., & Tauber, J. 2000, ApJ, 540, 886

Appendix A: MADEX: a local, non-LTE LVG code

The physical conditions in ISM clouds are such that molecular excitation is usually far from LTE. MADEX solves the non-LTE level excitation and line radiative transfer in a 1D isothermal homogeneous medium assuming a large velocity gradient (LVG) and spherical geometry. In this approximation the statistical-equilibrium equations are solved assuming *local* excitation conditions and a geometrically averaged escape probability formalism for the emitted photons (see details in Sobolev 1960; Castor 1970). This description allows one to take into account radiative trapping and collisional excitation and deexcitation more easily and computationally faster than more sophisticated *non-local* codes in which the radiative coupling between different cloud positions is explicitly treated (Montecarlo simulations, ALI methods, etc.). As a small benchmark, and in order to place the conclusions of our work on a firm ground, here we compare MADEX results with those obtained with RADEX[6], a publicly available escape probability code (see van der Tak et al. 2007 for the basic formulae).

We ran several models for CO (a low-dipole moment molecule with $\mu = 0.12$ D) and for HCO$^+$ ($\mu = 3.90$ D). These are typical examples of molecules with low and high critical densities, respectively (e.g. n_{cr}(CO $2 \rightarrow 1$) of a few 10^4 cm^{-3} and n_{cr}(HCO$^+$ $2 \rightarrow 1$) of a few 10^6 cm^{-3}). We note that for optically thin emission lines and for densities $n(H_2) \gg n_{cr}$, collisions dominate over radiative excitations and level populations get closer to LTE ($T_{ex} \rightarrow T_k$) as the density increases. For optically thick lines, line trapping effectively reduces n_{cr} and lines can be thermalized at lower densities. In the low density limit ($n(H_2) \ll n_{cr}$), level populations are subthermally excited and, as the density decreases, tend to thermalize to the background radiation temperature ($T_k > T_{ex} \rightarrow 2.7$ K in the millimetre domain).

Figure A.1 (upper panels) shows low density model results ($n(H_2) = 3 \times 10^3$ cm^{-3}) for N(CO) from 10^{15} to 10^{18} cm^{-2} at two different gas temperatures ($T_k = 10$ and 150 K, blue and red points, respectively). The left and right figures show the computed excitation temperatures and line centre opacities, respectively, for the CO $2 \rightarrow 1$, $3 \rightarrow 2$, and $4 \rightarrow 3$ transitions. Figure A.1 (*lower panels*) shows higher density models ($n(H_2) = 3 \times 10^5$ cm^{-3}) close to thermalization ($T_{ex} \simeq T_k$). We note that the selected range of column densities represents a transition from optically thin to optically thick emission. A line width of 1 km s^{-1} is adopted in all models.

Figure A.2 shows the same kind of models for HCO$^+$ (column densities from 10^{12} to 10^{15} cm^{-2}). Owing to the much higher critical densities of HCO$^+$ rotational transitions, their excitation is sub-thermal ($T_{ex} < T_k$) in most of the explored parameter space. In addition, their associated emission lines become optically thick for column densities smaller than those of CO.

The filled and empty square marks in Figs. A.1 and A.2 represent computations performed with MADEX and RADEX
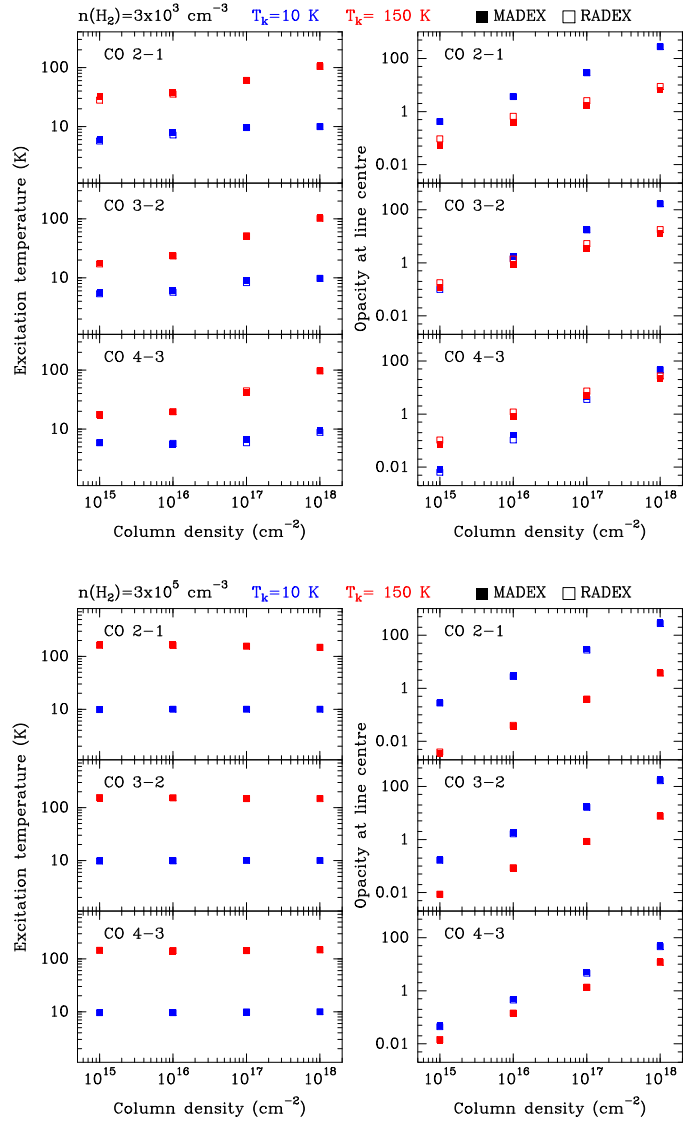
Fig. A.1. CO isothermal models carried out with MADEX (filled squares) and RADEX (empty squares) non-LTE radiative transfer codes. Two gas densities are considered: $n(H_2) = 3 \times 10^3$ cm^{-3} (*upper panels*) and $n(H_2) = 3 \times 10^5$ cm^{-3} (*lower panels*). Excitation temperatures and line centre opacities (*left* and *right* panels, respectively) are shown for several rotational transitions in the millimetre domain as a function of CO column density. Two gas temperatures are considered, 10 K (blue points) and 150 K (red points).

codes, respectively. We checked that for the considered models, the predicted excitation temperatures and line opacities agree within ~20% and ~40%, respectively. This translates into maximum brightness temperature differences of ~50% in the most extreme cases.

---

[6] http://www.sron.rug.nl/~vdtak/radex/radex.php

Fig. A.2. Same as Fig. A.1 but for HCO$^+$.

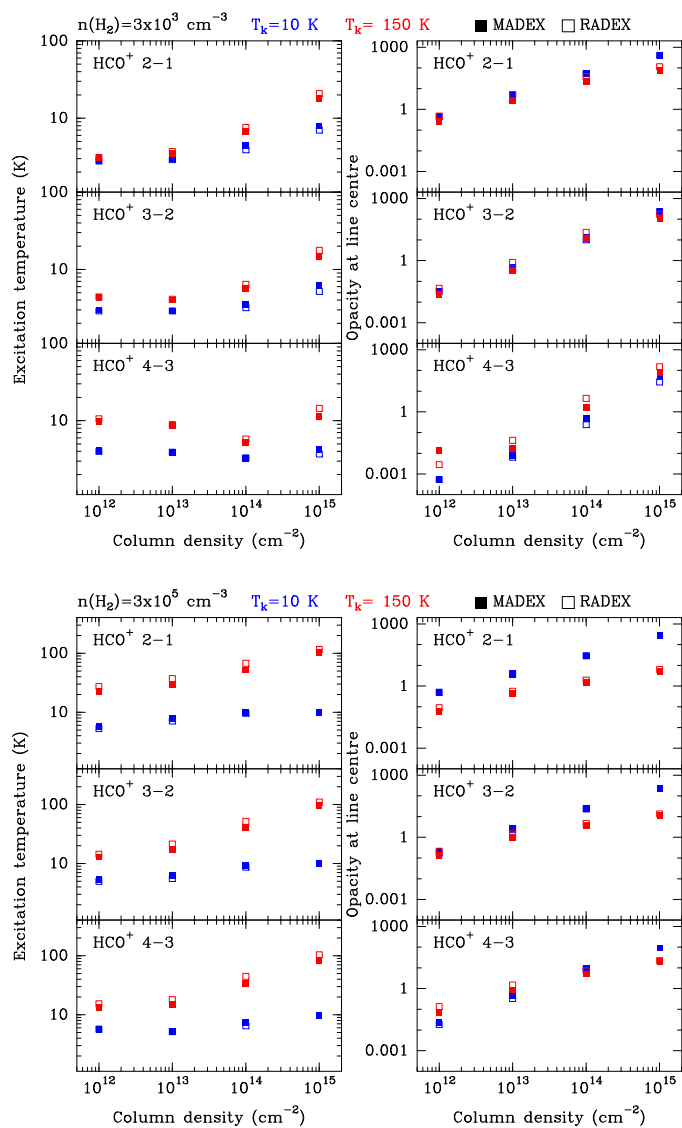# Appendix B: Identified hydrocarbon lines

Table B.1. Line parameters of C_2H.

Transition $(N, J, F)_u \to (N, J, F)_l$	Frequency [MHz]	E_u [K]	A_{ul} [s^{-1}]	S_{ij}	g_u	$\int T_{MB}\,dv$ [K km s^{-1}]	v_{LSR} [km s^{-1}]	Δv [km s^{-1}]	T_{MB} [K]
$(1, 3/2, 1) \to (0, 1/2, 1)$	$87\,284.105^F$	4.2	2.59×10^{-7}	0.2	3	0.40(1)	10.52(2)	3.03(6)	0.12
$(1, 3/2, 2) \to (0, 1/2, 1)$	$87\,316.898^F$	4.2	1.53×10^{-6}	1.7	5	3.82(1)	10.47(1)	2.91(1)	1.23
$(1, 3/2, 1) \to (0, 1/2, 0)$	$87\,328.585^F$	4.2	1.27×10^{-6}	0.8	3	1.86(1)	10.47(1)	2.89(2)	0.61
$(1, 1/2, 1) \to (0, 1/2, 1)$	$87\,401.989^F$	4.2	1.27×10^{-6}	0.8	3	1.89(1)	10.48(1)	2.88(1)	0.61
$(1, 1/2, 0) \to (0, 1/2, 1)$	$87\,407.165^F$	4.2	1.53×10^{-6}	0.3	1	0.74(1)	10.49(1)	2.84(4)	0.25
$(1, 1/2, 1) \to (0, 1/2, 0)$	$87\,446.470^F$	4.2	2.61×10^{-7}	0.2	3	0.39(1)	10.49(2)	2.90(5)	0.13
$(2, 5/2, 2) \to (1, 3/2, 2)$	$174\,634.861^W$	12.6	1.00×10^{-6}	0.1	5	1.32(19)	–	–	–
$(2, 5/2, 3) \to (1, 3/2, 2)$	$174\,663.199^W$	12.6	1.47×10^{-5}	2.8	7	⟩ 13.90(21)	–	–	–
$(2, 5/2, 2) \to (1, 3/2, 1)$	$174\,667.629^W$	12.6	1.36×10^{-5}	1.9	5		–	–	–
$(2, 3/2, 2) \to (1, 1/2, 1)$	$174\,721.744^W$	12.6	1.16×10^{-5}	1.6	5	2.84(17)	–	–	–
$(2, 3/2, 1) \to (1, 1/2, 0)$	$174\,728.071^W$	12.6	8.16×10^{-6}	0.7	3	⟩ 4.06(53)	–	–	–
$(2, 3/2, 1) \to (1, 1/2, 1)$	$174\,733.210^W$	12.6	5.08×10^{-6}	0.4	3		–	–	–
$(2, 3/2, 2) \to (1, 3/2, 2)$	$174\,806.843^W$	12.6	2.67×10^{-6}	0.4	5	1.52(26)	–	–	–
$(3, 7/2, 3) \to (2, 5/2, 3)$	$261\,978.120^F$	25.1	1.95×10^{-6}	0.1	7	0.33(1)	10.67(4)	2.04(9)	0.15
$(3, 7/2, 4) \to (2, 5/2, 3)$	$262\,004.260^F$	25.2	5.31×10^{-5}	3.9	9	9.19(5)	10.72(1)	1.86(1)	4.65
$(3, 7/2, 3) \to (2, 5/2, 2)$	$262\,006.482^F$	25.1	5.10×10^{-5}	2.9	7	10.10(6)	10.72(1)	2.39(1)	3.97
$(3, 5/2, 3) \to (2, 3/2, 2)$	$262\,064.986^F$	25.2	4.88×10^{-5}	2.8	7	6.74(7)	10.78(1)	1.90(2)	3.33
$(3, 5/2, 2) \to (2, 3/2, 1)$	$262\,067.469^F$	25.2	4.46×10^{-5}	1.8	5	6.18(7)	10.83(1)	2.39(3)	2.43
$(3, 5/2, 2) \to (2, 3/2, 2)$	$262\,078.934^F$	25.2	5.99×10^{-6}	0.2	5	0.68(2)	10.75(3)	2.09(8)	0.30
$(3, 5/2, 3) \to (2, 5/2, 3)$	$262\,208.614^F$	25.2	3.95×10^{-6}	0.2	7	0.67(1)	10.77(2)	2.29(6)	0.27
$(3, 5/2, 3) \to (2, 5/2, 2)$	$262\,236.957^F$	25.2	4.03×10^{-7}	0.02	7	0.06(1)	10.71(9)	1.35(22)	0.04
$(3, 5/2, 2) \to (2, 5/2, 2)$	$262\,250.928^F$	25.2	2.27×10^{-6}	0.09	5	0.27(1)	10.67(5)	2.17(15)	0.12
$(4, 9/2, 4) \to (3, 7/2, 4)$	$349\,312.833^F$	41.9	2.98×10^{-6}	0.09	9	0.22(1)	10.72(22)	2.32(44)	$0.15^\star$
$(4, 9/2, 5) \to (3, 7/2, 4)$	$349\,337.707^F$	41.9	1.30×10^{-4}	4.9	11	⟩ 18.09(5)	10.64(1)	2.93(1)	4.65
$(4, 9/2, 4) \to (3, 7/2, 3)$	$349\,338.989^F$	41.9	1.27×10^{-4}	3.9	9				
$(4, 7/2, 4) \to (3, 5/2, 3)$	$349\,399.274^F$	41.9	1.25×10^{-4}	3.8	9	⟩ 14.02(7)	10.69(1)	3.01(1)	3.33
$(4, 7/2, 3) \to (3, 5/2, 2)$	$349\,400.669^F$	41.9	1.19×10^{-4}	2.9	7				
$(4, 7/2, 3) \to (3, 5/2, 3)$	$349\,414.640^F$	41.9	7.02×10^{-6}	0.2	7	0.29(2)	10.80(11)	1.89(28)	$0.30^\star$
$(4, 7/2, 4) \to (3, 7/2, 4)$	$349\,603.611^F$	41.9	5.18×10^{-6}	0.2	9	0.34(1)	10.61(12)	2.14(26)	0.27

Notes. General notes to Appendix B tables: (i) Frequency, energy of the upper level of each transition (E_u), Einstein coefficient for spontaneous emission (A_{ul}), intrinsic line strength (S_{ij}), and the level degeneracy (g_u) from MADEX. The velocity-integrated intensity ($\int T_{MB}\,dv$), radial velocity (v_{LSR}), and FWHM line width (Δv) obtained by Gaussian fit. (ii) Parentheses indicate the uncertainty obtained by the Gaussian fitting programme. The fit uncertainty in units of the last significant digit is given in Tables B.1, B.6, and B.8. (iii) The weighted average of hyperfine and fine components is used for the analysis of C_2H, l-C_3H, c-C_3H, and C_4H molecules. (iv) Fully overlapping transitions are marked with connecting symbols. (v) We note that the line intensities in Tables B.2, B.4, B.5, and B.7 are given in units of mK. (vi) Labels: $^{(F)}$ Detected with FFTS backend. $^{(W)}$ The lines detected with WILMA backend just give information about the integrated line intensity (see Sect. 2). $^{(\star)}$ Marginal detection.

Table B.2. Line parameters of ^{13}CCH and C^{13}CH.

Transition $(N, J, F_1, F)_u \rightarrow (N, J, F_1, F)_l$	Frequency [MHz]	E_u [K]	A_{ul} [s^{-1}]	S_{ij}	g_u	$\int T_{MB} dv$ [mK km s^{-1}]	v_{LSR} [km s^{-1}]	Δv [km s^{-1}]	T_{MB} [mK]
^{13}CCH									
$(1, 3/2, 2, 5/2) \rightarrow (0, 1/2, 1, 3/2)$	84 119.329^F	4.0	1.37×10^{-6}	2.0	6	20.5(7.0)	11.0(0.3)	1.4(0.4)	14*
$(3, 7/2, 4, 9/2) \rightarrow (2, 5/2, 3, 7/2)$	252 422.933^F	24.2	4.75×10^{-5}	4.3	10	⎫ 114.2(6.6)	10.7(0.1)	3.6(0.3)	34
$(3, 7/2, 4, 7/2) \rightarrow (2, 5/2, 3, 5/2)$	252 424.122^F	24.2	4.63×10^{-5}	3.3	8	⎭			
$(3, 7/2, 3, 5/2) \rightarrow (2, 5/2, 2, 3/2)$	252 447.991^F	24.2	4.42×10^{-5}	2.4	6	⎫ 61.4(8.2)	10.5(0.2)	2.5(0.3)	27
$(3, 7/2, 3, 7/2) \rightarrow (2, 5/2, 2, 5/2)$	252 449.265^F	24.2	4.74×10^{-5}	3.4	8	⎭			
$(3, 5/2, 3, 7/2) \rightarrow (2, 3/2, 2, 5/2)$	252 457.865^F	24.2	4.16×10^{-5}	3.0	8	46.9(6.6)	10.4(0.2)	1.6(0.5)	19
$(3, 5/2, 3, 5/2) \rightarrow (2, 3/2, 2, 3/2)$	252 468.774^F	24.2	3.86×10^{-5}	2.1	6	18.4(8.2)	10.3(0.3)	1.4(0.7)	16
$(3, 5/2, 2, 5/2) \rightarrow (2, 3/2, 1, 3/2)$	252 480.925^F	24.2	3.17×10^{-5}	1.7	6	28.3(6.6)	11.0(0.2)	1.4(0.4)	15
$(3, 5/2, 2, 3/2) \rightarrow (2, 3/2, 1, 1/2)$	252 489.308^F	24.2	3.32×10^{-5}	1.2	4	16.0(3.3)	10.6(0.1)	1.4(0.4)	12
C^{13}CH									
$(1, 3/2, 2, 5/2) \rightarrow (0, 1/2, 1, 3/2)$	85 229.326^F	4.1	1.42×10^{-6}	2.0	6	36.3(7.0)	11.0(0.2)	2.2(0.4)	16*
$(3, 7/2, 3, 5/2) \rightarrow (2, 5/2, 2, 5/2)$	255 742.430^F	24.5	3.36×10^{-6}	0.2	6	12.0(6.7)	10.4(0.1)	0.6(0.3)	21
$(3, 7/2, 4, 9/2) \rightarrow (2, 5/2, 3, 7/2)$	255 746.086^F	24.5	4.94×10^{-5}	4.3	10	⎫ 151.7(15)	10.7(0.1)	3.0(0.4)	47
$(3, 7/2, 4, 7/2) \rightarrow (2, 5/2, 3, 5/2)$	255 747.258^F	24.5	4.83×10^{-5}	3.4	8	⎭			
$(3, 7/2, 3, 5/2) \rightarrow (2, 5/2, 2, 3/2)$	255 756.027^F	24.5	4.52×10^{-5}	2.4	6	51.3(16.6)	10.7(0.4)	2.4(0.9)	19
$(3, 7/2, 3, 7/2) \rightarrow (2, 5/2, 2, 5/2)$	255 758.767^F	24.5	4.81×10^{-5}	3.3	8	57.1(18.3)	10.5(0.2)	1.9(0.7)	31
$(3, 5/2, 3, 7/2) \rightarrow (2, 3/2, 2, 5/2)$	255 794.864^F	24.5	4.34×10^{-5}	3.0	8	46.1(11.6)	10.6(0.2)	1.6(0.5)	28
$(3, 5/2, 3, 5/2) \rightarrow (2, 3/2, 2, 3/2)$	255 803.715^F	24.5	4.34×10^{-5}	2.3	6	38.9(15.0)	10.7(0.2)	1.1(0.4)	35
$(3, 5/2, 2, 5/2) \rightarrow (2, 3/2, 1, 3/2)$	255 805.399^F	24.5	3.62×10^{-5}	1.9	6	34.5(20.0)	10.8(0.4)	1.9(0.8)	17

Table B.3. Line parameters of l-C$_3$H$^+$.

Transition $J \rightarrow J-1$	Frequency [MHz]	E_u [K]	A_{ul} [s^{-1}]	S_{ij}	g_u	$\int T_{MB} dv$ [K km s^{-1}]	Δv [km s^{-1}]	T_{MB} [K]	Notes
$4 \rightarrow 3$	89 957.849(0.054)^F	10.8	3.389×10^{-5}	4	9	0.12(0.01)	3.25(0.23)	0.033	[a]
$5 \rightarrow 4$	112 445.713(0.047)^F	16.2	6.770×10^{-5}	5	11	0.13(0.01)	2.96(0.32)	0.043	[a]
$6 \rightarrow 5$	134 932.733(0.010)^W	22.7	1.188×10^{-4}	6	13	0.21(0.04)	–	–	[b]
$7 \rightarrow 6$	157 418.719(0.016)^W	30.2	1.907×10^{-4}	7	15	0.16(0.03)	–	–	[b]
$9 \rightarrow 8$	202 386.776(0.065)^F	48.6	4.113×10^{-4}	9	19	0.20(0.01)	2.15(0.13)	0.088	[a]
$10 \rightarrow 9$	224 868.307(0.114)^F	59.4	5.672×10^{-4}	10	21	0.19(0.01)	2.40(0.21)	0.076	[a]
$11 \rightarrow 10$	247 348.016(0.080)^F	71.2	7.582×10^{-4}	11	23	0.14(0.01)	1.68(0.18)	0.080	[a]
$12 \rightarrow 11$	269 825.838(0.120)^F	84.2	9.878×10^{-4}	12	25	0.17(0.02)	2.00(0.28)	0.079	[a]
$13 \rightarrow 12$	292 301.412(0.065)^F	98.2	1.260×10^{-3}	13	27	0.19(0.02)	1.92(0.17)	0.095	[a]

Notes. [a] Observed frequencies of the detected lines and their uncertainties obtained by fitting Gaussian at 200 kHz spectral resolution and measured in the local standard of rest frame ($v_{LSR} = 10.7$ km s^{-1} in the Orion Bar PDR). [b] Frequencies and uncertainties reported in Pety et al. (2012).

Table B.4. Line parameters of l-C$_3$H.

Transition $(J^\mathrm{p}, F)_\mathrm{u} \rightarrow (J^\mathrm{p}, F)_\mathrm{l}$	Frequency [MHz]	E_u [K]	A_ul [s^{-1}]	S_{ij}	g_u	$\int T_\mathrm{MB}\,dv$ [mK km s^{-1}]	v_LSR [km s^{-1}]	Δv [km s^{-1}]	T_MB [mK]
$^2\Pi_{1/2} \rightarrow {}^2\Pi_{1/2}$									
$(9/2^+, 5 \rightarrow 7/2^-, 4)$	$97\,995.166^F$	12.5	6.12×10^{-5}	4.9	11	35.1(3.5)	10.3(0.2)	1.4(0.2)	24
$(9/2^+, 4 \rightarrow 7/2^-, 3)$	$97\,995.913^F$	12.5	5.95×10^{-5}	3.9	9	30.1(3.0)	10.2(0.4)	1.4(0.2)	20
$(9/2^-, 5 \rightarrow 7/2^+, 4)$	$98\,011.611^F$	12.5	6.13×10^{-5}	4.9	11	28.0(2.8)	10.8(0.2)	1.3(0.2)	20
$(9/2^-, 4 \rightarrow 7/2^+, 3)$	$98\,012.524^F$	12.5	5.96×10^{-5}	3.9	9	32.6(3.3)	10.8(0.3)	1.3(0.2)	24
$(13/2^-, 6 \rightarrow 11/2^+, 5)$	$149\,106.972^W$	46.1	2.11×10^{-4}	5.6	13	$\rangle$ 178.5(71.4)	–	–	–
$(13/2^-, 7 \rightarrow 11/2^+, 6)$	$149\,106.972^W$	46.1	2.14×10^{-4}	6.6	15				
$(13/2^+, 7 \rightarrow 11/2^-, 6)$	$149\,212.667^W$	46.2	2.14×10^{-4}	6.6	15	$\rangle$ 58.7(55.5)	–	–	–
$(13/2^+, 6 \rightarrow 11/2^-, 5)$	$149\,212.667^W$	46.2	2.12×10^{-4}	5.7	13				
$(15/2^+, 7 \rightarrow 13/2^-, 6)$	$171\,958.650^W$	54.4	3.33×10^{-4}	6.7	15	$\rangle$ 87.0(8.7)	–	–	–
$(15/2^+, 8 \rightarrow 13/2^-, 7)$	$171\,958.650^W$	54.4	3.36×10^{-4}	7.7	17				
$(15/2^-, 7 \rightarrow 13/2^+, 6)$	$172\,094.778^W$	54.4	3.34×10^{-4}	6.7	15	$\rangle$ 48.5(4.8)	–	–	–
$(15/2^-, 8 \rightarrow 13/2^+, 7)$	$172\,094.778^W$	54.4	3.37×10^{-4}	7.7	17				
$(19/2^+, 9 \rightarrow 17/2^-, 8)$	$217\,571.404^F$	74.2	6.96×10^{-4}	8.8	19	$\rangle$ 57.6(13.4)	10.9(0.2)	1.4(0.3)	39
$(19/2^+, 10 \rightarrow 17/2^-, 9)$	$217\,571.667^F$	74.2	7.00×10^{-4}	9.7	21				
$(19/2^-, 9 \rightarrow 17/2^+, 8)$	$217\,773.402^F$	74.2	6.98×10^{-4}	8.8	19	$\rangle$ 34.1(7.4)	10.6(0.2)	1.7(0.4)	17
$(19/2^-, 10 \rightarrow 17/2^+, 9)$	$217\,773.513^F$	74.2	7.02×10^{-4}	9.7	21				
$(27/2^-, 14 \rightarrow 25/2^+, 13)$	$295\,172.315^F$	102.1	1.81×10^{-3}	13.9	29	$\rangle$ 30.0(7.7)	11.1(0.1)	0.6(0.2)	48
$(27/2^-, 13 \rightarrow 25/2^+, 12)$	$295\,172.315^F$	102.1	1.81×10^{-3}	12.9	27				
$(27/2^+, 14 \rightarrow 25/2^-, 13)$	$295\,514.212^F$	102.2	1.82×10^{-3}	13.9	29	$\rangle$ 54.9(9.7)	10.2(0.1)	1.2(0.3)	41
$(27/2^+, 13 \rightarrow 25/2^-, 12)$	$295\,514.212^F$	102.2	1.82×10^{-3}	12.9	27				
$^2\Pi_{3/2} \rightarrow {}^2\Pi_{3/2}$									
$(9/2^-, 5 \rightarrow 7/2^+, 4)$	$103\,319.276^F$	32.9	6.47×10^{-5}	4.4	11	26.6(2.7)	10.9(0.2)	1.6(0.2)	16
$(9/2^-, 4 \rightarrow 7/2^+, 3)$	$103\,319.786^F$	32.9	6.30×10^{-5}	3.5	9	20.2(2.0)	10.2(0.2)	1.4(0.2)	14
$(9/2^+, 5 \rightarrow 7/2^-, 4)$	$103\,372.483^F$	32.9	6.49×10^{-5}	4.4	11	$\rangle$ 25.1(2.5)	10.0(0.4)	2.9(0.4)	8
$(9/2^+, 4 \rightarrow 7/2^-, 3)$	$103\,373.094^F$	32.9	6.31×10^{-5}	3.5	9				
$(13/2^+, 7 \rightarrow 11/2^-, 6)$	$141\,635.793^W$	25.1	1.92×10^{-4}	6.9	15	$\rangle$ 101.1(25.5)	–	–	–
$(13/2^+, 6 \rightarrow 11/2^-, 5)$	$141\,636.431^W$	25.1	1.90×10^{-4}	5.9	13				
$(13/2^-, 7 \rightarrow 11/2^+, 6)$	$141\,708.728^W$	25.1	1.92×10^{-4}	6.9	15	$\rangle$ 120.7(31.9)	–	–	–
$(13/2^-, 6 \rightarrow 11/2^+, 5)$	$141\,709.494^W$	25.1	1.90×10^{-4}	5.9	13				
$(15/2^-, 8 \rightarrow 13/2^+, 7)$	$163\,491.035^W$	32.9	2.90×10^{-4}	7.9	17	$\rangle$ 129.9(27.8)	–	–	–
$(15/2^-, 7 \rightarrow 13/2^+, 6)$	$163\,491.557^W$	32.9	2.96×10^{-4}	6.9	15				
$(15/2^+, 8 \rightarrow 13/2^-, 7)$	$163\,597.232^W$	32.9	3.00×10^{-4}	7.9	17	$\rangle$ 144.6(19.9)	–	–	–
$(15/2^+, 7 \rightarrow 13/2^-, 6)$	$163\,597.900^W$	32.9	2.96×10^{-4}	6.9	15				
$(19/2^-, 10 \rightarrow 17/2^+, 9)$	$207\,279.369^F$	51.8	6.18×10^{-4}	9.9	21	$\rangle$ 79.3(7.9)	10.5(0.1)	1.4(0.2)	53
$(19/2^-, 9 \rightarrow 17/2^+, 8)$	$207\,279.779^F$	51.8	6.14×10^{-4}	8.9	19				
$(19/2^+, 10 \rightarrow 17/2^-, 9)$	$207\,459.226^F$	51.8	6.19×10^{-4}	9.9	21	$\rangle$ 98.0(9.8)	10.5(0.2)	2.5(0.4)	37
$(19/2^+, 9 \rightarrow 17/2^-, 8)$	$207\,459.800^F$	51.8	6.16×10^{-4}	8.9	19				
$(21/2^+, 11 \rightarrow 19/2^-, 10)$	$229\,213.636^F$	62.8	8.40×10^{-4}	10.9	23	$\rangle$ 52.3(13.8)	10.4(0.2)	1.2(0.4)	40
$(21/2^+, 10 \rightarrow 19/2^-, 9)$	$229\,214.005^F$	62.8	8.36×10^{-4}	9.9	21				
$(21/2^-, 11 \rightarrow 19/2^+, 10)$	$229\,432.781^F$	62.8	8.42×10^{-4}	10.9	23	$\rangle$ 49.8(13.8)	10.5(0.3)	1.2(0.2)	39
$(21/2^-, 10 \rightarrow 19/2^+, 9)$	$229\,433.316^F$	62.8	8.38×10^{-4}	9.9	21				
$(23/2^-, 12 \rightarrow 21/2^+, 11)$	$251\,174.624^F$	74.8	1.11×10^{-3}	11.9	25	$\rangle$ 53.5(9.8)	10.6(0.1)	1.6(0.3)	32
$(23/2^-, 11 \rightarrow 21/2^+, 10)$	$251\,174.624^F$	74.8	1.11×10^{-3}	10.9	23				
$(23/2^+, 12 \rightarrow 21/2^-, 11)$	$251\,433.892^F$	74.9	1.11×10^{-3}	11.9	25	$\rangle$ 57.1(9.8)	10.8(0.2)	2.2(0.4)	25
$(23/2^+, 11 \rightarrow 21/2^-, 10)$	$251\,434.415^F$	74.9	1.11×10^{-3}	10.9	23				

Table B.5. Line parameters of c-C$_3$H.

Transition $(N_{K_aK_c}, J, F)_u \rightarrow (N_{K_aK_c}, J, F)_l$	Frequency [MHz]	E_u [K]	A_{ul} [s^{-1}]	S_{ij}	g_u	$\int T_{MB}\,dv$ [mK km s^{-1}]	v_{LSR} [km s^{-1}]	Δv [km s^{-1}]	T_{MB} [mK]
$(3_{1,2}, 5/2, 3) \rightarrow (3_{1,3}, 5/2, 3)$	85 272.149^F	14.9	3.40×10^{-6}	0.6	7	⟩ 21.6(5.9)	10.8(0.2)	1.2(0.4)	17
$(3_{1,2}, 5/2, 2) \rightarrow (3_{1,3}, 5/2, 2)$	85 272.522^F	14.9	3.64×10^{-6}	0.4	5				
$(3_{1,2}, 7/2, 4) \rightarrow (3_{1,3}, 7/2, 4)$	85 702.495^F	14.9	3.89×10^{-6}	0.8	9	7.5(4.7)	10.5(0.4)	0.9(0.6)	8
$(2_{1,2}, 5/2, 3) \rightarrow (1_{1,1}, 3/2, 2)$	91 494.349^F	4.4	1.59×10^{-5}	2.2	7	88.0(9.5)	10.5(0.2)	3.4(0.5)	29
$(2_{1,2}, 5/2, 2) \rightarrow (1_{1,1}, 3/2, 1)$	91 497.608^F	4.4	1.38×10^{-5}	1.3	5	52.4(9.5)	10.5(0.3)	2.9(0.6)	17
$(2_{1,2}, 3/2, 2) \rightarrow (1_{1,1}, 1/2, 1)$	91 699.471^F	4.4	1.37×10^{-5}	1.3	5	52.3(5.9)	10.8(0.3)	2.3(0.7)	21
$(2_{1,2}, 3/2, 2) \rightarrow (1_{1,1}, 3/2, 2)$	91 780.518^F	4.4	2.23×10^{-6}	0.2	5	24.2(5.9)	10.5(0.2)	1.7(0.4)	14
$(3_{1,3}, 7/2, 4) \rightarrow (2_{1,2}, 5/2, 3)$	132 993.978^W	10.8	6.06×10^{-5}	3.5	9	⟩ 227.3(17.6)	–	–	–
$(3_{1,3}, 7/2, 3) \rightarrow (2_{1,2}, 5/2, 2)$	132 994.679^W	10.8	5.75×10^{-5}	2.6	7				
$(3_{1,3}, 5/2, 2) \rightarrow (2_{1,2}, 3/2, 1)$	133 186.451^W	10.8	5.11×10^{-5}	1.6	5	⟩ 252.6(27.7)	–	–	–
$(3_{1,3}, 5/2, 3) \rightarrow (2_{1,2}, 3/2, 2)$	133 187.717^W	10.8	5.70×10^{-5}	2.5	7				
$(4_{1,4}, 9/2, 5) \rightarrow (3_{1,3}, 7/2, 4)$	172 463.355^W	19.1	1.43×10^{-4}	4.6	11	⟩ 32.3(3.2)	–	–	–
$(4_{1,4}, 9/2, 4) \rightarrow (3_{1,3}, 7/2, 3)$	172 463.718^W	19.1	1.39×10^{-4}	3.6	9				
$(4_{1,4}, 7/2, 3) \rightarrow (3_{1,3}, 5/2, 2)$	172 660.964^W	19.1	1.32×10^{-4}	2.7	7	⟩ 218.3(52.5)	–	–	–
$(4_{1,4}, 7/2, 4) \rightarrow (3_{1,3}, 5/2, 3)$	172 661.526^W	19.1	1.38×10^{-4}	3.6	9				
$(5_{1,5}, 11/2, 6) \rightarrow (4_{1,4}, 9/2, 5)$	211 117.576^F	29.2	2.74×10^{-4}	5.6	13	⟩ 182.2(14.6)	10.7(0.1)	2.1(0.2)	82
$(5_{1,5}, 11/2, 5) \rightarrow (4_{1,4}, 9/2, 4)$	211 117.834^F	29.2	2.68×10^{-4}	4.7	11				
$(5_{1,5}, 9/2, 4) \rightarrow (4_{1,4}, 7/2, 3)$	211 318.450^F	29.2	2.61×10^{-4}	3.7	9	⟩ 96.4(13.2)	10.6(0.1)	1.7(0.3)	54
$(5_{1,5}, 9/2, 5) \rightarrow (4_{1,4}, 7/2, 4)$	211 318.796^F	29.2	2.68×10^{-4}	4.7	11				
$(4_{1,3}, 9/2, 5) \rightarrow (3_{1,2}, 7/2, 4)$	216 488.286^F	25.3	2.51×10^{-4}	4.1	11	71.7(8.9)	10.7(0.1)	2.3(0.3)	30
$(4_{1,3}, 9/2, 4) \rightarrow (3_{1,2}, 7/2, 3)$	216 492.634^F	25.3	2.21×10^{-4}	2.9	9	32.4(5.9)	10.9(0.1)	1.3(0.3)	22
$(4_{1,3}, 7/2, 4) \rightarrow (3_{1,2}, 5/2, 3)$	216 638.258^F	25.3	2.26×10^{-4}	3.0	9	42.8(14.8)	10.6(0.1)	1.2(0.2)	29
$(4_{1,3}, 7/2, 3) \rightarrow (3_{1,2}, 5/2, 2)$	216 641.130^F	25.3	2.31×10^{-4}	2.4	7	20.1(16.3)	11.0(0.2)	0.9(0.1)	21
$(6_{1,6}, 13/2, 7) \rightarrow (5_{1,5}, 11/2, 6)$	249 544.145^F	41.2	4.65×10^{-4}	6.7	15	⟩ 125.4(13.0)	10.7(0.1)	1.8(0.2)	66
$(6_{1,6}, 13/2, 6) \rightarrow (5_{1,5}, 11/2, 5)$	249 544.343^F	41.2	4.59×10^{-4}	5.7	13				
$(6_{1,6}, 11/2, 5) \rightarrow (5_{1,5}, 9/2, 4)$	249 746.630^F	41.2	4.50×10^{-4}	4.7	11	⟩ 155.5(17.9)	10.5(0.2)	3.1(0.5)	47
$(6_{1,6}, 11/2, 6) \rightarrow (5_{1,5}, 9/2, 5)$	249 746.873^F	41.2	4.59×10^{-4}	5.7	13				
$(5_{1,4}, 11/2, 6) \rightarrow (4_{1,3}, 9/2, 5)$	252 697.373^F	37.4	4.09×10^{-4}	4.9	13	⟩ 123.6(8.2)	10.5(0.1)	2.5(0.2)	49
$(5_{1,4}, 11/2, 5) \rightarrow (4_{1,3}, 9/2, 4)$	252 698.198^F	37.4	4.01×10^{-4}	4.1	11				
$(5_{1,4}, 9/2, 4) \rightarrow (4_{1,3}, 7/2, 3)$	252 881.049^F	37.4	3.89×10^{-4}	3.2	9	⟩ 72.5(9.9)	10.6(0.1)	1.6(0.3)	44
$(5_{1,4}, 9/2, 5) \rightarrow (4_{1,3}, 7/2, 4)$	252 881.590^F	37.4	4.02×10^{-4}	4.1	11				
$(7_{1,7}, 15/2, 8) \rightarrow (6_{1,6}, 13/2, 7)$	287 920.669^F	55.0	7.28×10^{-4}	7.7	17	⟩ 148.0(16.8)	10.5(0.1)	1.7(0.2)	80
$(7_{1,7}, 15/2, 7) \rightarrow (6_{1,6}, 13/2, 6)$	287 920.669^F	55.0	7.21×10^{-4}	6.8	15				
$(7_{1,7}, 13/2, 6) \rightarrow (6_{1,6}, 11/2, 5)$	288 124.063^F	55.0	7.12×10^{-4}	5.8	13	⟩ 94.5(16.8)	10.6(0.2)	2.0(0.4)	43
$(7_{1,7}, 13/2, 7) \rightarrow (6_{1,6}, 11/2, 6)$	288 124.063^F	55.0	7.22×10^{-4}	6.8	15				
$(6_{1,5}, 13/2, 7) \rightarrow (5_{1,4}, 11/2, 6)$	289 270.928^W	51.3	6.41×10^{-4}	5.9	15	⟩ 78.7(20.6)	–	–	–
$(6_{1,5}, 13/2, 6) \rightarrow (5_{1,4}, 11/2, 5)$	289 271.481^W	51.3	6.32×10^{-4}	5.1	13				
$(6_{1,5}, 11/2, 5) \rightarrow (5_{1,4}, 9/2, 4)$	289 461.153^W	51.3	6.21×10^{-4}	4.2	11	⟩ 39.4(13.1)	–	–	–
$(6_{1,5}, 11/2, 6) \rightarrow (5_{1,4}, 9/2, 5)$	289 461.805^W	51.3	6.33×10^{-4}	5.1	13				

Table B.6. Line parameters of c-C_3H_2.

Transition $(J_{K_aK_c})_u \to (J_{K_aK_c})_l$	Sym	Frequency [MHz]	E_u [K]	A_{ul} [s^{-1}]	S_{ij}	g_u	$\int T_{MB}\,dv$ [K km s^{-1}]	v_{LSR} [km s^{-1}]	Δv [km s^{-1}]	T_{MB} [K]
$4_{2,2} \to 4_{1,3}$	para	$80\,723.179^F$	28.8	1.46×10^{-5}	1.8	9	0.10(1)	10.56(14)	2.60(41)	0.03
$2_{0,2} \to 1_{1,1}$	para	$82\,093.548^F$	6.4	2.07×10^{-5}	1.4	5	0.55(1)	10.64(2)	2.75(6)	0.19
$6_{6,1} \to 6_{5,2}$	ortho	$82\,583.441^F$	66.3	1.31×10^{-5}	2.2	13	0.01(1)	10.82(32)	0.86(44)	0.01*
$3_{1,2} \to 3_{0,3}$	ortho	$82\,966.196^F$	13.7	1.09×10^{-5}	1.0	7	0.48(1)	10.71(2)	2.61(6)	0.17
$3_{2,2} \to 3_{1,3}$	para	$84\,727.687^F$	16.1	1.15×10^{-5}	1.0	7	0.14(1)	10.79(5)	2.15(11)	0.06
$2_{1,2} \to 1_{0,1}$	ortho	$85\,338.900^F$	4.1	2.55×10^{-5}	1.5	5	2.03(2)	10.72(1)	2.72(2)	0.70
$4_{3,2} \to 4_{2,3}$	ortho	$85\,656.415^F$	26.7	1.67×10^{-5}	1.8	9	0.24(1)	10.75(3)	2.20(8)	0.10
$5_{4,2} \to 5_{3,3}$	para	$87\,435.317^F$	45.3	2.04×10^{-5}	2.5	11	0.04(1)	10.72(16)	2.01(73)	0.02
$6_{5,2} \to 6_{4,3}$	ortho	$90\,344.081^F$	62.4	2.38×10^{-5}	3.1	13	0.04(1)	10.72(21)	1.92(54)	0.02
$7_{4,3} \to 7_{3,4}$	ortho	$112\,490.768^F$	80.3	4.50×10^{-5}	3.5	15	0.05(1)	10.69(14)	0.98(41)	0.02
$3_{0,3} \to 2_{1,2}$	ortho	$117\,151.183^W$	9.7	7.67×10^{-5}	2.4	7	2.51(15)	–	–	–
$3_{1,3} \to 2_{0,2}$	para	$117\,546.231^W$	12.1	7.77×10^{-5}	2.5	7	0.74(6)	–	–	–
$3_{1,2} \to 2_{2,1}$	ortho	$145\,089.611^W$	13.7	7.44×10^{-5}	1.3	7	1.30(11)	–	–	–
$2_{2,0} \to 1_{1,1}$	para	$150\,436.558^W$	9.7	5.89×10^{-5}	0.6	5	0.32(6)	–	–	–
$4_{0,4} \to 3_{1,3}$	para	$150\,820.665^W$	19.3	1.80×10^{-4}	3.5	9	1.00(4)	–	–	–
$4_{1,4} \to 3_{0,3}$	ortho	$150\,851.898^W$	17.0	1.80×10^{-4}	3.5	9	3.00(19)	–	–	–
$6_{2,4} \to 6_{1,5}$	para	$150\,954.689^W$	54.7	6.87×10^{-5}	1.9	13	0.06(2)	–	–	–
$6_{3,4} \to 6_{2,5}$	ortho	$151\,039.149^W$	52.4	6.88×10^{-5}	1.9	13	0.20(3)	–	–	–
$5_{1,4} \to 5_{0,5}$	ortho	$151\,343.875^W$	33.1	4.35×10^{-5}	1.0	11	0.34(4)	–	–	–
$5_{2,4} \to 5_{1,5}$	para	$151\,361.102^W$	35.4	4.35×10^{-5}	1.0	11	0.09(2)	–	–	–
$3_{2,2} \to 2_{1,1}$	para	$155\,518.308^W$	16.1	1.23×10^{-4}	1.7	7	0.68(4)	–	–	–
$4_{2,2} \to 3_{2,1}$	para	$204\,788.929^F$	28.8	1.37×10^{-4}	1.0	9	0.20(1)	10.83(5)	2.03(14)	0.09
$3_{3,0} \to 2_{2,1}$	ortho	$216\,278.738^F$	17.1	2.81×10^{-4}	1.4	7	1.29(1)	10.74(9)	2.29(2)	0.53
$6_{0,6} \to 5_{1,5}$	para	$217\,822.057^F$	38.6	5.93×10^{-4}	5.5	13	⎫ 3.14(1)	10.75(1)	2.18(1)	1.35
$6_{1,6} \to 5_{0,5}$	ortho	$217\,822.180^F$	36.3	5.93×10^{-4}	5.5	13	⎭			
$5_{1,4} \to 4_{2,3}$	ortho	$217\,940.045^F$	33.1	4.43×10^{-4}	3.4	11	1.60(1)	10.78(1)	2.13(1)	0.70
$5_{2,4} \to 4_{1,3}$	para	$218\,160.462^F$	35.4	4.44×10^{-4}	3.4	11	0.56(1)	10.79(2)	2.20(4)	0.24
$8_{2,6} \to 8_{1,7}$	para	$218\,448.823^F$	86.9	1.64×10^{-4}	2.0	17	⎫ 0.10(1)	10.75(10)	2.27(25)	0.04
$8_{3,6} \to 8_{2,7}$	ortho	$218\,449.400^F$	84.6	1.64×10^{-4}	2.0	17	⎭			
$7_{1,6} \to 7_{0,7}$	ortho	$218\,732.683^F$	58.8	9.82×10^{-5}	1.0	15	⎫ 0.16(1)	10.75(5)	2.07(11)	0.07
$7_{2,6} \to 7_{1,7}$	para	$218\,732.767^F$	61.2	9.82×10^{-5}	1.0	15	⎭			
$4_{3,2} \to 3_{2,1}$	ortho	$227\,169.143^F$	26.7	3.43×10^{-4}	1.9	9	1.10(2)	10.74(2)	2.11(5)	0.49
$3_{2,1} \to 2_{1,2}$	ortho	$244\,222.155^F$	15.8	6.49×10^{-5}	0.2	7	0.38(2)	10.76(5)	2.23(13)	0.16
$5_{2,3} \to 4_{3,2}$	ortho	$249\,054.415^F$	38.7	4.57×10^{-4}	2.4	11	0.79(1)	10.80(1)	1.93(4)	0.39
$7_{0,7} \to 6_{1,6}$	ortho	$251\,314.362^F$	48.3	9.35×10^{-4}	6.5	15	⎫ 2.22(1)	10.78(1)	1.98(1)	1.05
$7_{1,7} \to 6_{0,6}$	para	$251\,314.369^F$	50.7	9.35×10^{-4}	6.5	15	⎭			
$6_{1,5} \to 5_{2,4}$	para	$251\,508.713^F$	47.5	7.42×10^{-4}	4.4	13	0.37(1)	10.76(2)	1.82(6)	0.19
$6_{2,5} \to 5_{1,4}$	ortho	$251\,527.325^F$	45.1	7.42×10^{-4}	4.4	13	1.16(1)	10.80(1)	2.00(2)	0.55
$10_{3,7} \to 10_{2,8}$	para	$251\,773.193^F$	137.6	2.98×10^{-4}	2.9	21	⎫ 0.02(1)	10.75(13)	0.93(23)	0.02*
$10_{4,7} \to 10_{3,8}$	ortho	$251\,773.421^F$	135.3	2.98×10^{-4}	2.9	21	⎭			
$8_{1,7} \to 8_{0,8}$	para	$252\,409.829^F$	76.5	1.34×10^{-4}	1.0	17	⎫ 0.10(1)	10.76(1)	2.01(26)	0.05
$8_{2,7} \to 8_{1,8}$	ortho	$252\,409.834^F$	74.1	1.34×10^{-4}	1.0	17	⎭			

Table B.6. continued.

Transition $(J_{K_aK_c})_u \to (J_{K_aK_c})_l$	Sym	Frequency [MHz]	E_u [K]	A_{ul} [s^{-1}]	S_{ij}	g_u	$\int T_{MB}dv$ [K km s^{-1}]	v_{LSR} [km s^{-1}]	Δv [km s^{-1}]	T_{MB} [K]
$5_{3,3} \to 4_{2,2}$	para	$254\,987.657^F$	41.1	5.17×10^{-4}	2.5	11	0.31(1)	10.72(4)	2.18(10)	0.13
$5_{3,2} \to 4_{4,1}$	ortho	$260\,479.764^W$	42.4	1.77×10^{-4}	0.8	11	0.25(8)	–	–	–
$4_{4,1} \to 3_{3,0}$	ortho	$265\,759.483^F$	29.9	7.99×10^{-4}	2.8	9	0.94(1)	10.79(1)	1.94(3)	0.46
$4_{4,0} \to 3_{3,1}$	para	$282\,381.108^F$	32.5	8.11×10^{-4}	2.37	9	0.42(2)	10.80(4)	2.09 (10)	0.19
$8_{0,8} \to 7_{1,7}$	para	$284\,805.229^F$	64.3	1.39×10^{-3}	7.45	17	$\rangle$ 2.05(2)	10.64(1)	2.21(3)	0.87
$8_{1,8} \to 7_{0,7}$	ortho	$284\,805.230^F$	62.0	1.39×10^{-3}	7.45	17				
$6_{2,4} \to 5_{3,3}$	para	$284\,913.028^F$	54.7	8.38×10^{-4}	3.44	13	0.26(2)	10.65(8)	2.19(21)	0.11
$7_{1,6} \to 6_{2,5}$	ortho	$284\,998.025^F$	58.8	1.15×10^{-3}	5.42	15	$\rangle$ 1.50(2)	10.38(2)	2.82(5)	0.50
$7_{2,6} \to 6_{1,5}$	para	$284\,999.377^F$	61.2	1.15×10^{-3}	5.42	15				
$6_{3,4} \to 5_{2,3}$	ortho	$285\,795.689^F$	52.4	8.49×10^{-4}	3.45	13	0.79(2)	10.65(3)	2.17(7)	0.34
$5_{4,2} \to 4_{3,1}$	para	$300\,191.723^F$	45.3	7.61×10^{-4}	2.26	11	0.28(3)	11.13(17)	3.01(41)	0.09
$5_{5,0} \to 4_{4,1}$	ortho	$349\,264.002^F$	46.6	1.81×10^{-3}	3.41	11	0.63(5)	10.60(12)	3.11(38)	0.19
$7_{3,4} \to 6_{4,3}$	ortho	$351\,523.296^F$	74.9	1.36×10^{-3}	3.43	15	0.26(5)	10.86(19)	1.91(45)	0.13
$10_{1,10} \to 9_{0,9}$	ortho	$351\,781.573^F$	94.1	2.68×10^{-3}	9.45	21	$\rangle$ 0.79(6)	10.61(7)	1.87(15)	0.40
$10_{0,10} \to 9_{1,9}$	para	$351\,781.573^F$	96.5	2.68×10^{-3}	9.45	21				
$9_{1,8} \to 8_{2,7}$	ortho	$351\,965.963^F$	91.0	2.33×10^{-3}	7.41	19	$\rangle$ 0.49(5)	10.54(7)	1.50(15)	0.31
$9_{2,8} \to 8_{1,7}$	para	$351\,965.969^F$	93.3	2.33×10^{-3}	7.41	19				
$8_{3,6} \to 7_{2,5}$	ortho	$352\,193.664^F$	84.6	1.91×10^{-3}	5.42	17	0.35(5)	10.74(13)	1.60(16)	0.21

Table B.7. Line parameters of l-H$_2$C$_3$.

Transition $(J_{K_aK_c})_u \to (J_{K_aK_c})_l$	Sym	Frequency [MHz]	E_u [K]	A_{ul} [s^{-1}]	S_{ij}	g_u	$\int T_{MB}dv$ [mK km s^{-1}]	v_{LSR} [km s^{-1}]	Δv [km s^{-1}]	T_{MB} [mK]
$4_{1,4} \to 3_{1,3}$	ortho	$82\,395.089^F$	8.9	4.56×10^{-5}	3.8	9	65.5(9.3)	10.7(0.1)	2.1(0.4)	29
$4_{0,4} \to 3_{0,3}$	para	$83\,165.345^F$	10.0	5.00×10^{-5}	4.0	9	22.8(9.3)	10.5(0.6)	2.8(1.1)	8*
$4_{1,3} \to 3_{1,2}$	ortho	$83\,933.699^F$	9.1	4.82×10^{-5}	3.8	9	75.2(8.2)	10.7(0.2)	2.0(0.4)	29
$5_{1,5} \to 4_{1,4}$	ortho	$102\,992.379^F$	13.8	9.33×10^{-5}	4.8	11	67.5(8.4)	10.5(0.2)	2.7(0.4)	26
$5_{0,5} \to 4_{0,4}$	para	$103\,952.926^F$	15.0	9.99×10^{-5}	5.0	11	28.5(7.2)	10.8(0.3)	2.5(0.8)	11
$5_{1,4} \to 4_{1,3}$	ortho	$104\,915.583^F$	14.1	9.86×10^{-5}	4.8	11	91.3(8.4)	10.5(0.2)	3.7(0.4)	23
$7_{1,7} \to 6_{1,6}$	ortho	$144\,183.804^W$	26.7	2.68×10^{-4}	6.9	15	96.9(30.7)	–	–	–
$7_{1,6} \to 6_{1,5}$	ortho	$146\,876.061^W$	27.2	2.83×10^{-4}	6.9	15	105.6(33.4)	–	–	–
$8_{1,8} \to 7_{1,7}$	ortho	$164\,777.547^W$	34.6	4.06×10^{-4}	7.9	17	78.9(25.2)	–	–	–
$8_{1,7} \to 7_{1,6}$	ortho	$167\,854.234^W$	35.3	4.29×10^{-4}	7.9	17	110.2(21.3)	–	–	–
$10_{1,10} \to 9_{1,9}$	ortho	$205\,960.125^F$	53.4	8.06×10^{-4}	9.9	21	65.0(13.0)	10.7(0.2)	1.7(0.5)	36
$10_{0,10} \to 9_{0,9}$	para	$207\,843.289^F$	54.9	8.37×10^{-4}	10.0	21	27.8(8.7)	10.7(0.2)	1.5(0.4)	17*
$10_{1,9} \to 9_{1,8}$	ortho	$209\,805.427^F$	54.4	8.52×10^{-4}	9.9	21	80.4(17.5)	10.7(0.2)	2.2(0.5)	35
$11_{1,11} \to 10_{1,10}$	ortho	$226\,548.575^F$	64.3	1.08×10^{-3}	10.9	23	65.4(18.3)	10.6(0.2)	1.6(0.4)	50
$12_{0,12} \to 11_{0,11}$	para	$249\,367.939^F$	77.8	1.46×10^{-3}	12.0	25	95.8(14.7)	10.9(0.2)	2.5(0.5)	36*
$12_{1,11} \to 11_{1,10}$	ortho	$251\,748.328^F$	77.6	1.49×10^{-3}	11.9	25	37.2(9.9)	10.7(0.1)	1.0(0.3)	36
$13_{0,13} \to 12_{0,12}$	para	$270\,121.513^W$	90.8	1.86×10^{-3}	13.0	27	14.5(2.9)*	–	–	–
$13_{1,12} \to 12_{1,11}$	ortho	$272\,716.158^F$	90.6	1.90×10^{-3}	12.9	27	35.9(8.8)	10.9(0.1)	1.0(0.2)	34*

Table B.8. Line parameters of C_4H.

Transition	Frequency	E_u	A_{ul}	S_{ij}	g_u	$\int T_{MB} dv$	v_{LSR}	Δv	T_{MB}
$(N, J)_u \rightarrow (N, J)_l$	[MHz]	[K]	[s^{-1}]			[K km s^{-1}]	[km s^{-1}]	[km s^{-1}]	[K]
$(9, 19/2) \rightarrow (8, 17/2)$	$85\,634.023^F$	20.5	2.63×10^{-6}	9.5	20	0.21(1)	10.55(5)	2.66(13)	0.074
$(9, 17/2) \rightarrow (8, 15/2)$	$85\,672.563^F$	20.6	2.62×10^{-6}	8.5	18	0.19(1)	10.46(5)	2.61(12)	0.067
$(10, 21/2) \rightarrow (9, 19/2)$	$95\,150.402^F$	25.1	3.62×10^{-6}	10.5	22	0.20(1)	10.55(5)	2.61(13)	0.071
$(10, 19/2) \rightarrow (9, 17/2)$	$95\,188.935^F$	25.1	3.61×10^{-6}	9.5	20	0.19(1)	10.31(7)	2.90(17)	0.061
$(11, 23/2) \rightarrow (10, 21/2)$	$104\,666.575^F$	30.1	4.84×10^{-6}	11.5	24	0.21(1)	10.61(4)	2.60(10)	0.078
$(11, 21/2) \rightarrow (10, 19/2)$	$104\,705.099^F$	30.2	4.83×10^{-6}	10.5	22	0.20(1)	10.59(6)	2.84(16)	0.066
$(12, 25/2) \rightarrow (11, 23/2)$	$114\,182.520^F$	35.6	6.31×10^{-6}	12.5	26	0.25(2)	10.70(8)	2.51(21)	0.093
$(12, 23/2) \rightarrow (11, 21/2)$	$114\,221.035^F$	35.6	6.29×10^{-6}	11.5	24	0.23(1)	10.72(6)	2.42(14)	0.100
$(14, 29/2) \rightarrow (13, 27/2)$	$133\,213.644^W$	47.9	1.01×10^{-5}	14.5	30	0.27(5)	–	–	–
$(14, 27/2) \rightarrow (13, 25/2)$	$133\,252.140^W$	48.0	1.01×10^{-5}	13.5	28	0.26(6)	–	–	–
$(15, 31/2) \rightarrow (14, 29/2)$	$142\,728.783^W$	54.8	1.24×10^{-5}	15.5	32	0.23(5)	–	–	–
$(15, 29/2) \rightarrow (14, 27/2)$	$142\,767.267^W$	54.8	1.24×10^{-5}	14.5	30	0.28(4)	–	–	–
$(16, 33/2) \rightarrow (15, 31/2)$	$152\,243.611^W$	62.1	1.51×10^{-5}	16.5	34	0.21(3)	–	–	–
$(16, 31/2) \rightarrow (15, 29/2)$	$152\,282.083^W$	62.1	1.51×10^{-5}	15.5	32	0.30(4)	–	–	–
$(17, 35/2) \rightarrow (16, 33/2)$	$161\,758.109^W$	69.9	1.81×10^{-5}	17.5	36	0.26(4)	–	–	–
$(17, 33/2) \rightarrow (16, 31/2)$	$161\,796.568^W$	69.9	1.81×10^{-5}	16.5	34	0.24(3)	–	–	–
$(18, 37/2) \rightarrow (17, 35/2)$	$171\,272.255^W$	78.1	2.16×10^{-5}	18.5	38	0.16(3)	–	–	–
$(18, 35/2) \rightarrow (17, 33/2)$	$171\,310.702^W$	78.1	2.15×10^{-5}	17.5	36	$^{(s)}$	–	–	–
$(22, 45/2) \rightarrow (21, 43/2)$	$209\,324.922^F$	115.5	3.95×10^{-5}	22.5	46	0.25(1)	10.78(4)	2.04(10)	0.117
$(22, 43/2) \rightarrow (21, 41/2)$	$209\,363.306^F$	115.6	3.95×10^{-5}	21.5	44	0.26(1)	10.68(4)	2.35(12)	0.104
$(23, 47/2) \rightarrow (22, 45/2)$	$218\,837.007^F$	126.0	4.52×10^{-5}	23.5	48	0.23(1)	10.82(4)	2.15(10)	0.101
$(23, 45/2) \rightarrow (22, 43/2)$	$218\,875.374^F$	126.1	4.52×10^{-5}	22.5	46	0.21(1)	10.72(4)	1.84(10)	0.106
$(24, 49/2) \rightarrow (23, 47/2)$	$228\,348.618^F$	137.0	5.14×10^{-5}	24.5	50	0.20(2)	10.76(9)	2.08(24)	0.092
$(24, 47/2) \rightarrow (23, 45/2)$	$228\,386.966^F$	137.0	5.14×10^{-5}	23.5	48	0.17(2)	10.69(13)	2.35(35)	0.068
$(25, 51/2) \rightarrow (24, 49/2)$	$237\,859.735^F$	148.4	5.81×10^{-5}	25.5	52	0.16(2)	10.84(9)	1.62(28)	0.090
$(25, 49/2) \rightarrow (24, 47/2)$	$237\,898.065^F$	148.5	5.81×10^{-5}	24.5	50	0.21(2)	10.65(11)	2.27(27)	0.087
$(26, 53/2) \rightarrow (25, 51/2)$	$247\,370.338^F$	160.3	6.54×10^{-5}	26.5	54	0.20(1)	10.89(6)	1.96(15)	0.094
$(26, 51/2) \rightarrow (25, 49/2)$	$247\,408.648^F$	160.3	6.54×10^{-5}	25.5	52	0.20(1)	10.71(6)	2.19(15)	0.084
$(27, 55/2) \rightarrow (26, 53/2)$	$256\,880.407^F$	172.6	7.33×10^{-5}	27.5	56	0.19(2)	10.83(7)	1.70(20)	0.104
$(27, 53/2) \rightarrow (26, 51/2)$	$256\,918.696^F$	172.7	7.33×10^{-5}	26.5	54	0.18(1)	10.75(7)	2.08(17)	0.082
$(28, 57/2) \rightarrow (27, 55/2)$	$266\,389.921^F$	185.4	8.18×10^{-5}	28.5	58	0.14(1)	10.85(8)	1.96(18)	0.067
$(28, 55/2) \rightarrow (27, 53/2)$	$266\,428.190^F$	185.5	8.18×10^{-5}	27.5	56	0.12(1)	10.60(8)	1.90(20)	0.057
$(29, 59/2) \rightarrow (28, 57/2)$	$275\,898.861^F$	198.6	9.10×10^{-5}	29.5	60	0.17(2)	10.73(8)	1.60(22)	0.102
$(29, 57/2) \rightarrow (28, 55/2)$	$275\,937.107^F$	198.7	9.10×10^{-5}	28.5	58	0.15(2)	10.67(10)	1.76(27)	0.081
$(30, 61/2) \rightarrow (29, 59/2)$	$285\,407.207^F$	212.3	1.01×10^{-4}	30.5	62	0.15(2)	10.53(15)	2.30(32)	0.062
$(30, 59/2) \rightarrow (29, 57/2)$	$285\,445.430^F$	212.4	1.01×10^{-4}	29.5	60	0.14(3)	10.52(34)	2.50(59)	0.052
$(31, 63/2) \rightarrow (30, 61/2)$	$294\,914.937^F$	226.5	1.11×10^{-4}	31.5	64	0.11(1)	10.59(7)	1.89(23)	0.105
$(31, 61/2) \rightarrow (30, 59/2)$	$294\,953.137^F$	226.6	1.11×10^{-4}	30.5	62	0.06(1)	10.74(10)	1.45(24)	0.074
$(32, 65/2) \rightarrow (31, 63/2)$	$304\,422.034^F$	241.1	1.22×10^{-4}	32.5	66	0.16(2)	10.38(18)	2.17(50)	0.068*
$(32, 63/2) \rightarrow (31, 61/2)$	$304\,460.209^F$	241.2	1.22×10^{-4}	31.5	64	0.11(4)	10.95(37)	1.90(32)	0.056*